The diurnal cycle of precipitation over the Maritime Continent

A thesis submitted to the School of Environmental Sciences
of the University of East Anglia in partial fulfilment
of the requirements for the degree of Doctor of Philosophy

Jack Mustafa

May 2024

Abstract

The archipelago straddling the equator between the Indian and Pacific Oceans, known as the Maritime Continent (MC), is a broad region experiencing very high mean precipitation rate. Powerful global circulation cells are driven by the significant latent heat released over the MC. As such, variability of precipitation over the MC has widespread implications for global weather.

The dominant source of precipitation variability over the MC is the diurnal cycle (DC). As the spatio-temporal resolution of satellite-derived precipitation data products continues to improve it is becoming possible to characterise the DC in increasing detail. The first diurnal harmonic (FDH) waveform becomes an increasingly insufficient approximation of the 24-hour variability as complex DC characteristics are increasingly resolved. In order to characterise rapid changes in precipitation rate within the DC, such as the rapid intensification typical over land in the afternoon, the characterisation of the DC with waveforms more complex than the FDH is explored. The amplitudes of the complex waveforms are shown to be a more reliable indicator of the magnitude of diurnal variability than the amplitude of the FDH, and the phases of the complex waveforms offer a more reliable indication of the time of peak precipitation. These new parameters offer a more detailed framework with which a modelled DC may be assessed.

The simulated DC of precipitation in convection-parametrised (MC12) and convection-permitting (MC2) configurations of the Met Office Unified Model are analysed in the newly-developed characterisation framework. The nature of the DC is generally accurate in MC2, however the DC phase is several hours too early in MC12, as in many convection-parametrised models. These results demonstrate the capacity for skillful simulation of diurnal variability in a convection-permitting model without significant influence of boundary forcing.

The DC is shown to strengthen and weaken, slightly ahead of large-scale precipitation variability associated with the Madden-Julian Oscillation (MJO), an intra-seasonal mode of variability featuring eastward propagation of a large-scale convective envelope across the Indian and Pacific Oceans. Systematic shifts in the phase of the DC of up to four hours are observed in some locations, with westward (*eastward*) propagation of precipitation favoured before (*after*) the passage of the MJO over the MC. A resultant west–east phase regime divide is identified over the large islands and certain seas.

Acronyms

CCKW	Convectively-Coupled Kelvin Wave
DC	Diurnal Cycle
DJF	December-January-February
ENSO	El Niño–Southern Oscillation
EOF	Empirical Orthogonal Function
ERA5	ECMWF Reanalysis v5
FDH	First Diurnal Harmonic
GA7	Global Atmosphere 7
GCM	Global Climate Model
GPM	Global Precipitation Measurement
IMERG	Integrated Multi-Satellite Retrievals for GPM
IOD	Indian Ocean Dipole
ISWR	Incoming Shortwave Radiation
JULES	Joint UK Land Environment Simulator
KPP	*K*-Profile Parametrisation
LST	Local Solar Time
MC	Maritime Continent
MERRA-2	Modern-Era Retrospective Analysis for Research and Application, version 2
MetUM	UK Met Office Unified Model

MJO	Madden-Julian Oscillation
NAO	North Atlantic Oscillation
NEMO	Nucleus for European Modelling of the Ocean
OASIS	Ocean Atmosphere Sea Ice Soil
OLR	Outgoing Long-wave Radiation
OMI	OLR-based MJO Index
OSTIA	Operational Sea Surface Temperature and Ice Analysis
PC	Principal Component
PMW	Passive Microwave
QBO	Quasi-Biennial Oscillation
RAL2T	Regional Atmosphere and Land 2: Tropical
RMM	Real-time Multivariate MJO
RQ	Research Question
SST	Sea Surface Temperature
TOGA COARE	Tropical Ocean Global Atmosphere Coupled Ocean Atmosphere Response Experiment
TMPA	TRMM Multi-Satellite Precipitation Analysis
TRMM	Tropical Rainfall Measuring Mission
UK	United Kingdom
UKMO	UK Met Office

Acknowledgements

I am fortunate to have had too many people to individually thank support me over the past four years. Primary thanks must go to my UEA all-star supervisory team: Adrian, Rob, Karen and Marina. With Adrian's enthusiasm and subject experience, Rob's efficiency tips (even if I never did resort to Pot Noodles in the office), Karen's agonising but invaluable feedback on written work and Marina's commitment to involvement and support from afar, I always came away from supervisory meetings feeling purposeful, supported and uplifted.

Having had to undertake a substantial part of this research from home during the pandemic, much gratitude is owed to all my housemates who helped to keep me going through much uncertainty. Most of all, to Beth, for invaluable help with Python programming in the early days, coaxing me into participating in the 2020 Norwich Science Festival and for dragging me along to ballroom and Latin dance classes which have been a great release for the three years since.

To the Tropical Hour squad, the badminton group and friends within the gymnastics and ballroom and Latin dance clubs. Thanks for many fun moments; the richness of the past four years has made for many happy lasting memories.

To the brilliant occupants of 3.16, much gratitude for contributing to such a dynamic office environment that I always looked forward to coming into. Here's hoping any future offices feature as many unhinged conversations, yoga balls and beautiful sunsets.

To all my family who have supported me since long before beginning this thesis, much more recognition is owed than an acknowledgement here. This thesis is a testament to my dedication and originality, which I would never have developed without such a stable and nurturing upbringing.

The research in this thesis was carried out on the High Performance Computing Cluster supported by the Research and Specialist Computing Support service at the University of East Anglia.

Contents

List of figures

Chapter 1

Introduction

1.1 Motivation

The Maritime Continent (MC) — the islands and surrounding shallow seas around the equator between the Indian Ocean and the western Pacific Ocean (Figure 1.1; Peatman et al., 2014) — is a region of special interest in weather research. High temperature and humidity across the region favour high mean precipitation rates (Figure 1.2a; Sakaeda et al., 2017), which release substantial latent heat into the surrounding atmosphere. This atmospheric energy centre acts as a "boiler box", powering atmospheric teleconnection responses around the tropics and beyond into the extra-tropics (Ramage, 1968). As such, the weather dynamics operating over the MC are of global, as well as local, consequence.

Unfortunately, MC weather dynamics are notoriously challenging to simulate accurately in weather forecasting models (e.g. Neale & Slingo, 2003; Dirmeyer et al., 2012). This is due to the wide range of modes of weather variability that operate over the MC; while most of these modes of variability are understood fairly well in isolation, their scale interactions are less conceptually predictable, meaning that it is not straightforward to assess how faithfully a model simulates such interactions. Further, complex land–sea distribution and topography are not well represented in global models due to computational restrictions on resolution, therefore the complex interactions between weather systems and the islands and their topography cannot be fully captured.

One of the modes of MC weather variability that is most challenging for models to simulate accurately is the diurnal cycle (DC). Considering the

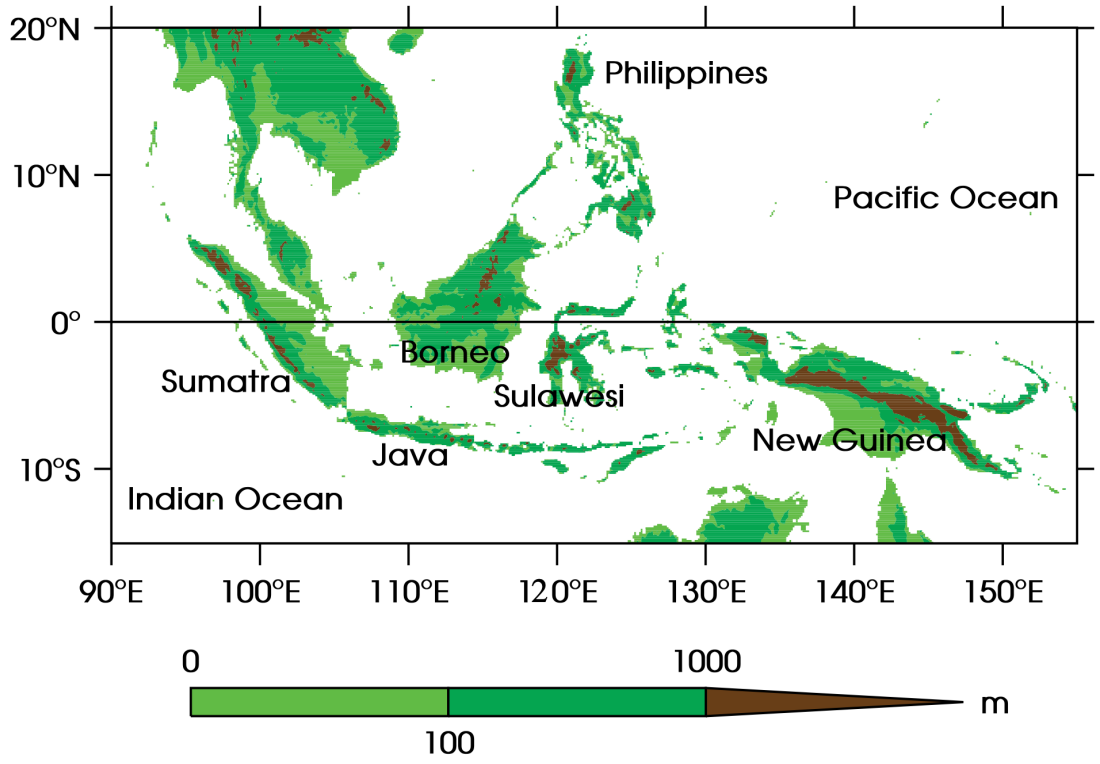

Figure 1.1: Labelled topographic map of the MC. *Image adapted from Peatman et al. (2014), Figure 1.*

manifestation of the DC in precipitation, for instance, the strongest DC occurs over the islands of the MC (Figure 1.2b; Sakaeda et al., 2017), where maximum precipitation tends to occur in the hours around sunset (Figure 1.2c; Sakaeda et al., 2017), while a slightly weaker DC with maximum precipitation in the hours around sunrise is typical over the near-coastal seas of the MC. Models, in particular those with a horizontal grid spacing of greater than 5 km which rely on a parametrisation scheme to represent deep convective processes, are typically unable to faithfully simulate the DC, especially its timing (e.g. Baranowski et al., 2019). The hindcast simulation described by Love et al. (2011), run with 40 km horizontal grid resolution, exemplifies the erroneous DC often generated by such coarse models, featuring peak precipitation several hours too early over land at around midday (Figure 1.3).

Model errors in the simulation of diurnal processes over the MC are liable to propagate into more global errors as a result of scale interactions between the DC and propagating modes of MC weather variability. In particular, the Madden–Julian Oscillation (MJO) has been shown to influence global weather patterns, including over the North Atlantic Ocean, via atmospheric teleconnection responses (e.g. Cassou, 2008; Skinner et al., 2022). The scale

interaction between the DC and the MJO therefore provides a clear dynamical pathway through which DC simulation error may be propagated globally. This motivates research into the observed characteristics of the DC, the simulated characteristics of the DC in different models, and the scale interaction between the DC and the MJO in both observations and models. Across the following three sections, a more detailed overview of the existing knowledge on these topics is presented.

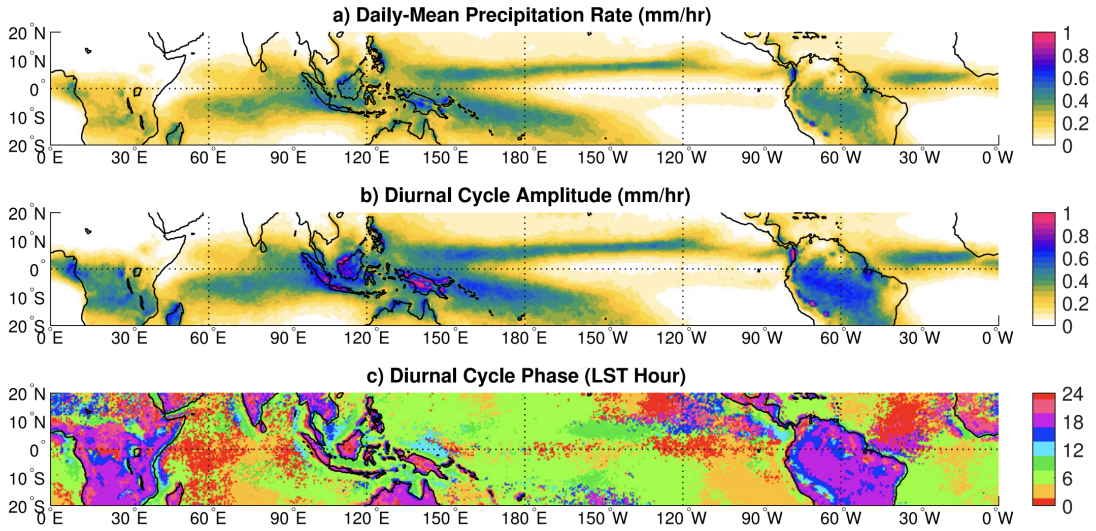

Figure 1.2: (a) Mean precipitation rate, (b) DC amplitude and (c) time of day of maximum precipitation, based on the November–March composite DC in TRMM. *Image adapted from Sakaeda et al. (2017), Figure 1.*

1.2 The Maritime Continent

The MC (Figure 1.1) features a complex distribution of islands of a range of shapes, sizes and orientations, the largest of which — New Guinea, Borneo, Sumatra, Java and Sulawesi — are over 180,000 km^2 in area and are among the largest non-continental islands on Earth, while the smallest of which have an area of less than 1 km^2 (Love et al., 2011). The MC is also topographically complex, with several areas well over 1000 m above mean sea level, and with the highest peaks exceeding 4000 m. Key regions of high topography include the New Guinea Highlands running WNW–ESE across the centre of New Guinea, the Barisan Mountains running NW–SE just inland of the southwestern coast of Sumatra, northeastern-to-central Borneo and central Sulawesi, with isolated peaks also observed along the W–E length of Java.

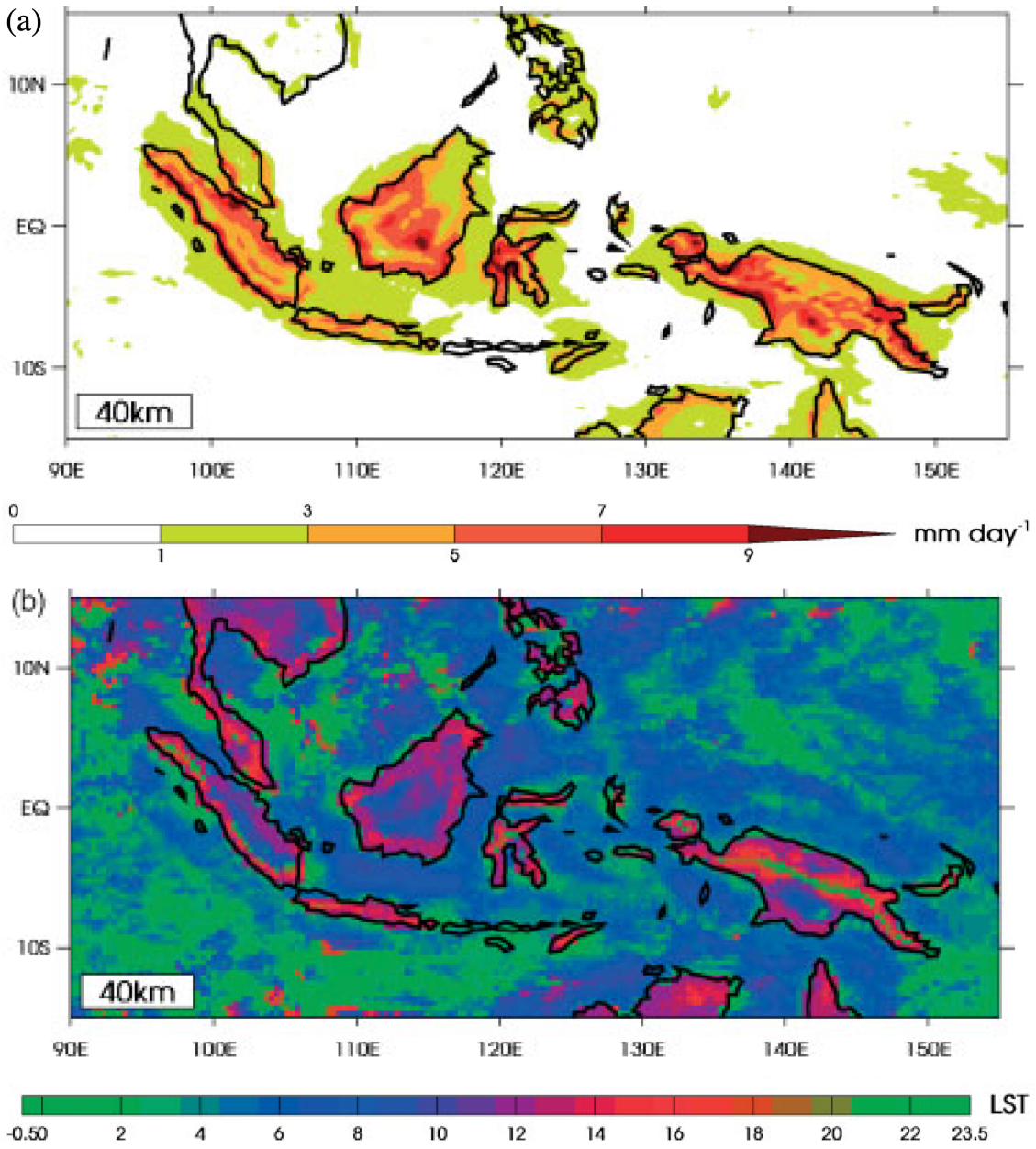

Figure 1.3: First diurnal harmonic (a) amplitude and (b) phase of maximum precipitation (in LST), of the DC simulated by a configuration of the MetUM with 40 km horizontal grid resolution run from October 2008 to April 2009. *Image adapted from Love et al. (2011), Figures 5&6.*

The MC is situated in the "Indo-Pacific warm pool" (e.g. Fasullo & Webster, 1999; Cravatte et al., 2009; Hu et al., 2017; Yin et al., 2022), a broad region of seas and ocean around the equator with typical sea surface temperatures (SSTs) in excess of 28°C (Figure 1.4). Such warm SSTs are considered a necessary condition for the development of tropical deep convection (Hoyos & Webster, 2012; Evans & Webster, 2014), which describes intense convective updrafts that

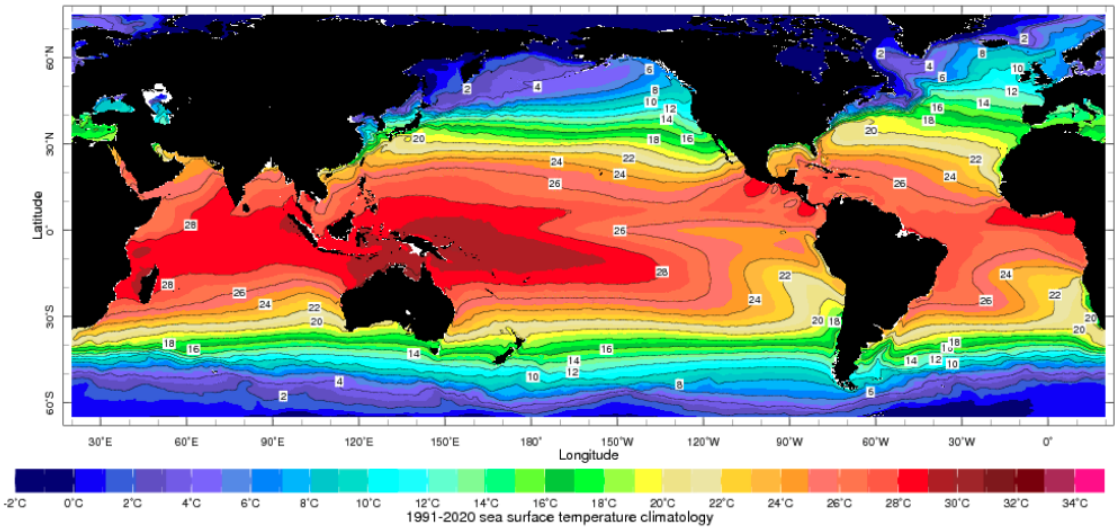

Figure 1.4: Illustration of the global pattern of mean SST during January. *Image adapted from* https://iridl.ldeo.columbia.edu/maproom/Global/Climatologies/SST_Loop.html.

penetrate upwards as far as the tropopause, which itself is higher than anywhere else globally at around 16-17 km altitude (e.g. Gage & Reid, 1987; Neale & Slingo, 2003). According to the Clausius-Clapeyron relation, with an increase in absolute air temperature comes a monotonic increase in the saturation vapour pressure (i.e. warmer air can hold more water vapour; e.g. Koutsoyiannis, 2012; Berg et al., 2013). As such, as a moist air parcel ascends through the troposphere and expands as the ambient atmospheric pressure decreases, its absolute temperature decreases. Its capacity to retain its water vapour content therefore also decreases, triggering the release of latent heat to the surrounding atmosphere as the excess water vapour condenses. The warming due to latent heat release continues adding buoyancy to the air parcel, creating a feedback mechanism for continued ascent until the original supply of water vapour has almost all condensed; as such, the most warm and humid air parcels near the surface will have the greatest potential for heat gain via latent heat release, driving deep convection. The intensity and scale of the regional-mean updraft due to tropical deep convection over the MC mean that it is able to drive atmospheric circulation throughout the tropics as the ascending limb of a Walker circulation cell, and into the extra-tropics as the ascending limb of the Hadley circulation cell (e.g. Lau et al., 1983; Jin & Hoskins, 1995; Neale & Slingo, 2003). The precise longitudinal alignment of the Walker circulation is sensitive to the states of certain modes of MC weather variability and to longer-term climatic changes (e.g. Adames & Wallace, 2014; Bayr et al., 2014; Schwendike et al., 2015;

Kim et al., 2020). It is this regional forcing of global circulation cells and the sensitivity of these cells to regional modes of variability that mark the MC as a region of global importance for weather forecasting.

Within the MC region, precipitation is perhaps foremost among the meteorological variables of greatest interest. Its intensity over the MC and warm pool generally (Figure 1.2a; Sakaeda et al., 2017) in association with deep convection leads it to sometimes be referred to as the Indo-Pacific rain pool or wet pool (e.g. Graham & Barnett, 1987; Dayem et al., 2007; Zhang & Chen, 2008; Yin et al., 2022). Precipitation across the wet pool is dominated by convective precipitation — precipitation associated with an organised local updraft where condensation of water vapour and formation of precipitation occur throughout much of the depth of the troposphere — while stratiform precipitation, associated with more widespread cloud cover at a single pressure level in the mid-upper troposphere, typically accounts for a smaller proportion of precipitation across the MC, particularly over land (e.g. Schumacher & Houze, 2003; Mori et al., 2004; Love et al., 2011). Convective precipitation may initiate rapidly and, in extreme cases, lead to natural disasters such as flash floods and landslides (e.g. Kirschbaum et al., 2012; Senior et al., 2023). Such extreme weather events tend to occur when a number of weather systems, often associated with a range of modes of MC weather variability, combine (e.g. Latos et al., 2021 & 2023). As such, it is desirable to understand the dynamics driving each mode of DC weather variability, as well as be able to predict the scale interactions of these modes of variability via faithful model representation.

A number of distinct modes of variability influencing MC weather can be isolated; these range from the El Niño–Southern Oscillation (ENSO; e.g. Bellenger et al., 2014; Santoso et al., 2017; Power et al., 2021) and the Quasi-Biennial Oscillation (QBO; e.g. Son et al., 2017; Densmore et al., 2019; Sun et al., 2019; Martin et al., 2021; Li et al., 2022) at interannual timescales, through the seasonal cycle with its distinct monsoonal activity (e.g. Chang et al., 2005; Toh et al., 2018), then the MJO (Section 1.4) and convectively-coupled Kelvin waves (CCKWs) and equatorial Rossby waves at intra-seasonal and synoptic timescales (e.g. Wang, 1988; Tsuda et al., 2006; Sakaeda et al., 2020), down to the DC (Section 1.3) at the high-frequency end of the spectrum. Each mode of variability has a distinct atmospheric signature that evolves in a generally predictable manner when uninterrupted, however the scale interactions of these modes tend to be rather sensitive and less readily predictable. The challenges posed by MC scale interactions must be addressed in order to significantly boost

the predictive potential of global weather forecasts (Figure 1.5).

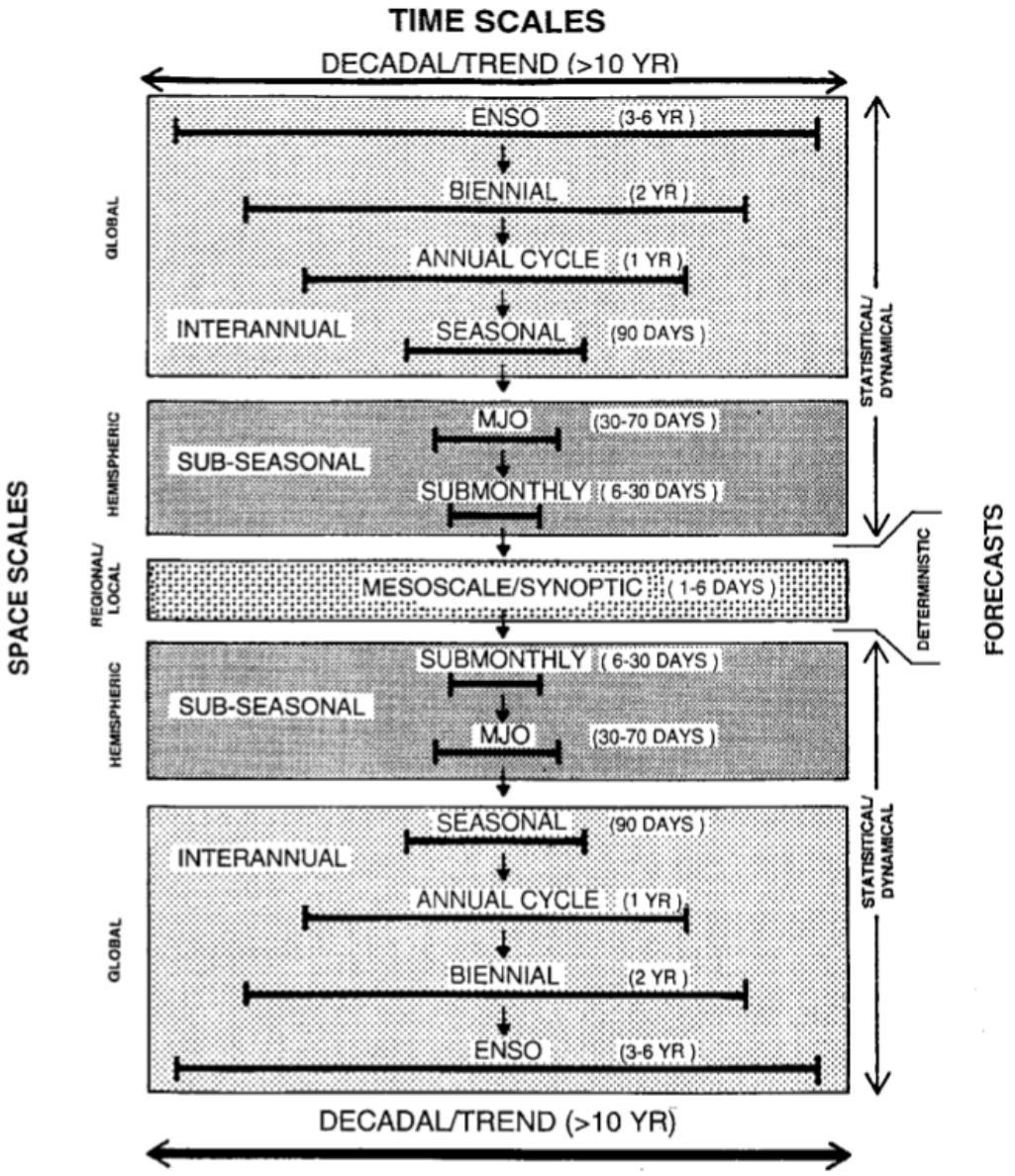

Figure 1.5: Schematic of the spatial and temporal range of scale interactions that occur around the MC. Global, long timescale modes of variability have a downscale influence on successively more local and short-timescale modes of variability, down to the DC and its component physical structures, encapsulated within the "mesoscale/synoptic" grouping. These mesoscale modes of variability then have an upscale influence back toward long-timescale modes of variability. *Image adapted from Meehl et al. (2001), Figure 3.*

1.3 The Diurnal Cycle

A DC may be defined as the composite 24-hour cycle (as an absolute or a perturbation from the mean state) of a variable of interest across a representative time period, or more qualitatively as the component of variability that can be attributed to known diurnal forcing mechanisms on any given day. While precipitation is focused on in the present research, previous studies have considered the DC across a broad range of meteorological variables beyond precipitation (Yang & Smith, 2006), including SST (e.g. Webster et al., 1996; Sui et al., 1997; Matthews et al., 2014), land surface temperature, moisture and associated sensible and latent heat fluxes (e.g. Ignatov & Gutman, 1999; Duan et al., 2014; Renner et al., 2021), horizontal winds and vertical winds/mass divergence (e.g. He et al., 2013; Repinaldo et al., 2015; Short et al., 2019), surface pressure (e.g. Dai & Wang, 1999; Schindelegger & Ray, 2014; Dai, 2023), cloud cover and size (e.g. Mapes & Houze, 1993; Soden, 2000; Tian et al., 2004; Eastman & Warren, 2014), outgoing longwave radiation (OLR; e.g. Smith & Rutan, 2003; Taylor, 2012), and frequency of thunderstorms and lightning strikes (e.g. Dai, 2001; Virts et al., 2013; Minobe et al., 2020). DC studies have been staged across a range of spatial scales, from the local scale across urban heat islands and small islands (e.g. Zhou et al., 2013; Lang et al., 2020) through to the continental, tropical or even planetary scales (e.g. Janowiak et al., 2005; Sharifnezhad et al., 2021). Ultimately, the DC in each of these meteorological variables is driven by the daily cycle in incoming shortwave radiation (ISWR; i.e. sunlight); the daily cycle of ISWR to the top of the atmosphere is dependent primarily on latitude and the time of year. As such, diurnal forcing is strongest in the tropics where maximum ISWR around midday is most intense and contrasts most strongly with the absence of ISWR overnight, though there is also evidence for weak diurnal behaviour at high latitude (e.g. Wang & Zender, 2011; Tastula et al., 2013).

Diurnal behaviour tends to be most repeatable and therefore strongest over and around any boundary between areas with strongly contrasting Earth surface properties. The most obvious such boundary is a coastline; land and water respond very differently to ISWR. Land is opaque to ISWR, meaning that radiative heating of land occurs in a very thin surface layer and the resultant temperature increase is rapid as a result of being concentrated into a small volume. In contrast, water is more transparent to ISWR, meaning that radiative heating is distributed more sparsely across the surface layer, mostly within

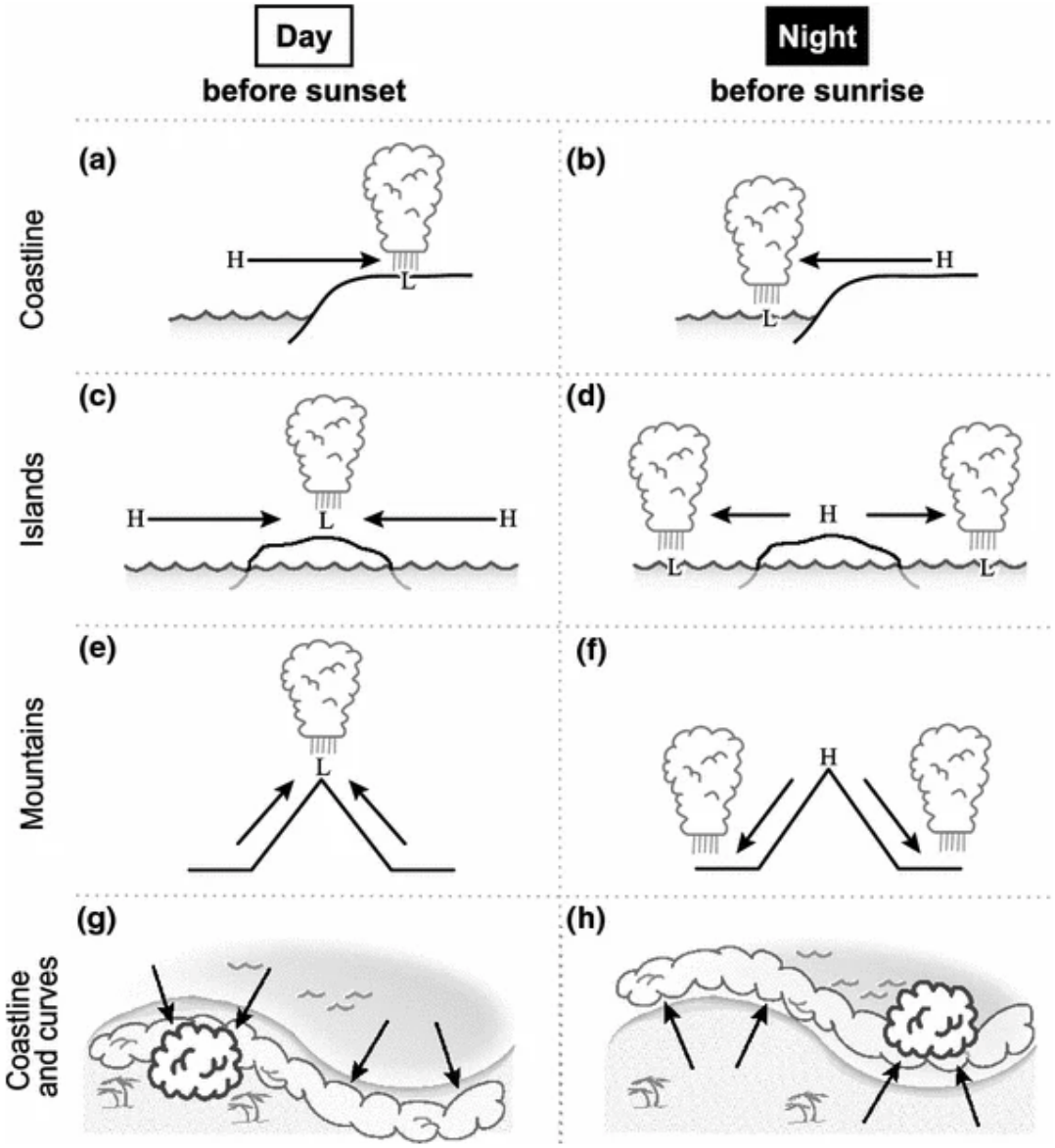

Figure 1.6: Schematics of low-level wind flow and convection associated with (a-d) land–sea breezes and (e&f) mountain–valley breezes, and (g&h) the influence of coastline shape on organisation of the convection induced by land–sea breezes. *Image adapted from Biasutti et al. (2012), Figure 16.*

the uppermost metre. Additionally, as a liquid, water has the capacity to redistribute the surface radiative heat input deeper into the water column by means of convection, while land is only able to redistribute heat deeper into the Earth by means of conduction, which is much slower. Finally, over water, transfer of energy from the water into the atmosphere predominantly occurs via "latent heating" — the evaporation of water, which raises the humidity of the atmosphere more than its temperature — while over land, a much greater

proportion of the heat transfer into the atmosphere occurs via "sensible heating" — heating via conduction. The result of these combined contrasting features of land and water mean that the surface layer of land warms more rapidly, particularly under tropical solar radiative forcing, and transfers heat into the atmospheric boundary layer much more rapidly. This establishes a horizontal temperature (and density) gradient within the atmospheric boundary layer, resulting in the development of a "sea breeze" density current (Figure 1.6a) — low-level winds blowing across the coastline onto land. The incoming sea breeze forces the ascent of the rapidly warming near-surface air over land, which is likely to develop into a convective updraft over land featuring intense convective precipitation. Overnight, the opposite radiative process occurs as the land surface cools more rapidly than the water surface, so the near-surface atmosphere over land loses more sensible heat than that over water, leading to development of a denser atmospheric boundary layer over land which drives a "land breeze" density current (Figure 1.6b) offshore through the night and favours the triggering of convection and precipitation offshore overnight.

Kikuchi & Wang (2008) identify the coastal DC regime of tropical precipitation as the strongest such regime, ahead of the continental and oceanic regimes (Figure 1.7). The continental DC regime has intermediate strength, partially due to the presence of a range of types of land surface, the boundaries between which may act similarly to the land–sea contrast. Examples of such contrasts are between heavily vegetated areas and more arid areas (e.g. Baldi et al., 2008; Garcia-Carreras et al., 2010), between land and large inland water bodies such as lakes (e.g. Holle & Murphy, 2017; Nicholson et al., 2021), and between large urban areas and their rural surroundings (e.g. Shepherd, 2005; Argüeso et al., 2016). Additionally, variable topography allows for the development of horizontal density gradients even across a single type of land surface. As the near-surface atmosphere on a slope warms, a horizontal density gradient develops between the warming air adjacent to the slope and the un-warmed air at the same pressure level away from the slope, leading to ascent of the air adjacent to the slope, typically developing into an organised "valley breeze" density current (Figure 1.6e) with upslope ("anabatic") wind flow. Conversely, a downslope (or "katabatic") "mountain breeze" density current (Figure 1.6f) may develop overnight. Variable topography also leads to an uneven distribution of ISWR strength; for instance, the eastward side of a mountain will experience an early-shifted DC of ISWR with maximum warming before solar noon, at the time of day when the sun is perpendicular to

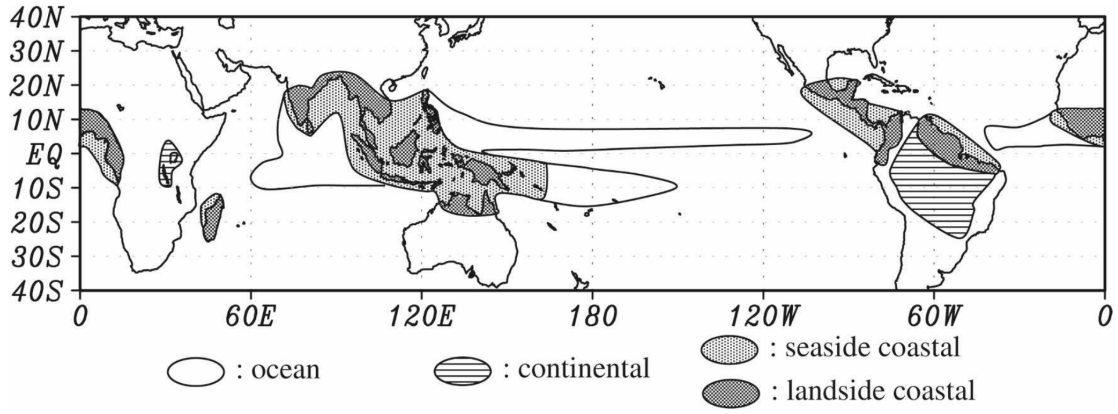

Figure 1.7: Illustration of the tropical distribution of diurnal precipitation regimes, with each regime diagnosed according to its range, peak time, and presence/absence of phase propagation. *Image adapted from Kikuchi & Wang (2008), Figure 10.*

the eastward-dipping slope, while the westward side of the mountain will not see the sun until some hours later and will therefore experience a late-shifted DC of ISWR. The weak SST diurnal cycle over the open ocean, compounded by the lack of spatial heterogeneity, leads to a comparatively weak open ocean precipitation DC regime. Kikuchi & Wang (2008) identified the MC as a region dominated by the coastal DC regime (tending toward the oceanic regime away into the Indian and Pacific Oceans), and as such is renowned as a region with a very strong DC. A key feature of the coastal DC regime is phase propagation; evidence that the precipitation maximum becomes increasingly late with distance offshore from the coastline. The land breeze density current is not the only mechanism that is theoretically capable of producing overnight phase propagation; studies have investigated the roles of mountain breeze density currents (e.g. Qian et al., 2012; Junquas et al., 2018; Coppin & Bellon, 2019b), cold pool-triggered density currents (e.g. Wu et al., 2009; Dipankar et al., 2019), and gravity waves (e.g. Mapes et al., 2003; Love et al., 2011; Hassim et al., 2016; Coppin & Bellon, 2019a; Yokoi et al., 2019) in producing the observed phase propagation. While the consensus remains weak, particularly concerning the relative influence of different types of density current, there is increasing recognition that different mechanisms may be dominant at different distances from the coastlines, specifically with gravity waves seemingly more influential further offshore as they propagate more quickly than density currents.

The meteorological DC across the tropics has been the subject of many previous studies since at least the mid-20^{th} century (e.g. Dexter, 1944; Riehl, 1947), with a range of field campaigns conducted to better characterise and

understand the dynamics of the DC since that time. The Tropical Ocean Global Atmosphere Coupled Ocean Atmosphere Response Experiment (TOGA COARE) was among the first major field campaigns conducted close to the MC, observing 4 months from November 1992 to February 1993 (e.g. Webster & Lukas, 1992; Soloviev & Lukas, 1997). Satellite-derived data products were also extensively used around this time period (e.g. Albright et al., 1985; Nitta & Sekine, 1994) Yang & Slingo, 2001) including Yang & Slingo (2001) who were among the first to characterise the DC of precipitation across the entire tropics (Figure 1.8), however these data products typically quantified brightness temperature or another variable with which precipitation could be approximately inferred. Greater spatial coverage of more direct precipitation observations was attained across the tropics with the onset of the Tropical Rainfall Measuring Mission (TRMM) satellite in 1997, active until 2015. With the data collected during this mission, a gridded data product of precipitation with a spatial resolution of 0.25° by 0.25° and a temporal resolution of 3 hours was developed (TRMM 3B42), alongside other more robust data products at lower temporal resolution. As quantified in TRMM data, the DC demonstrates qualitatively similar characteristics at the large scale as were estimated with earlier data products (e.g. Figure 1.2; Sakaeda et al., 2017).

Such characterisations of the DC of precipitation indicate that the strongest diurnal variability is focused around the near-equatorial land masses of the MC, South America and Africa, with variability almost as strong over much of the tropical Indian Ocean, two off-equator bands over the western-to-central Pacific Ocean, and immediately north of the equator over the Atlantic Ocean (Figures 1.8a & 1.2b). Particularly over the oceans, strong diurnal variability tends to be collocated with high mean precipitation (Figure 1.2a) — it is over land that diurnal variability is typically strongest in proportion to local mean precipitation. The complex spatial pattern of diurnal phase is also coarsely captured — over land, maximum precipitation tends to be observed in the hours surrounding sunset, while over the seas and oceans, maximum precipitation tends to be observed in the hours around sunrise (Figures 1.8b & 1.2c). Many studies characterise the DC using the amplitude and phase of the first diurnal harmonic (FDH), explicitly or implicitly assuming that the FDH offers a good characterisation of the DC with the main effect of muting noise. It has been noted that the apparent timing of the DC depends on the phase parameter with which maximum precipitation is described; Bai & Schumacher (2022) demonstrated a systematic regionally-dependent difference between the time

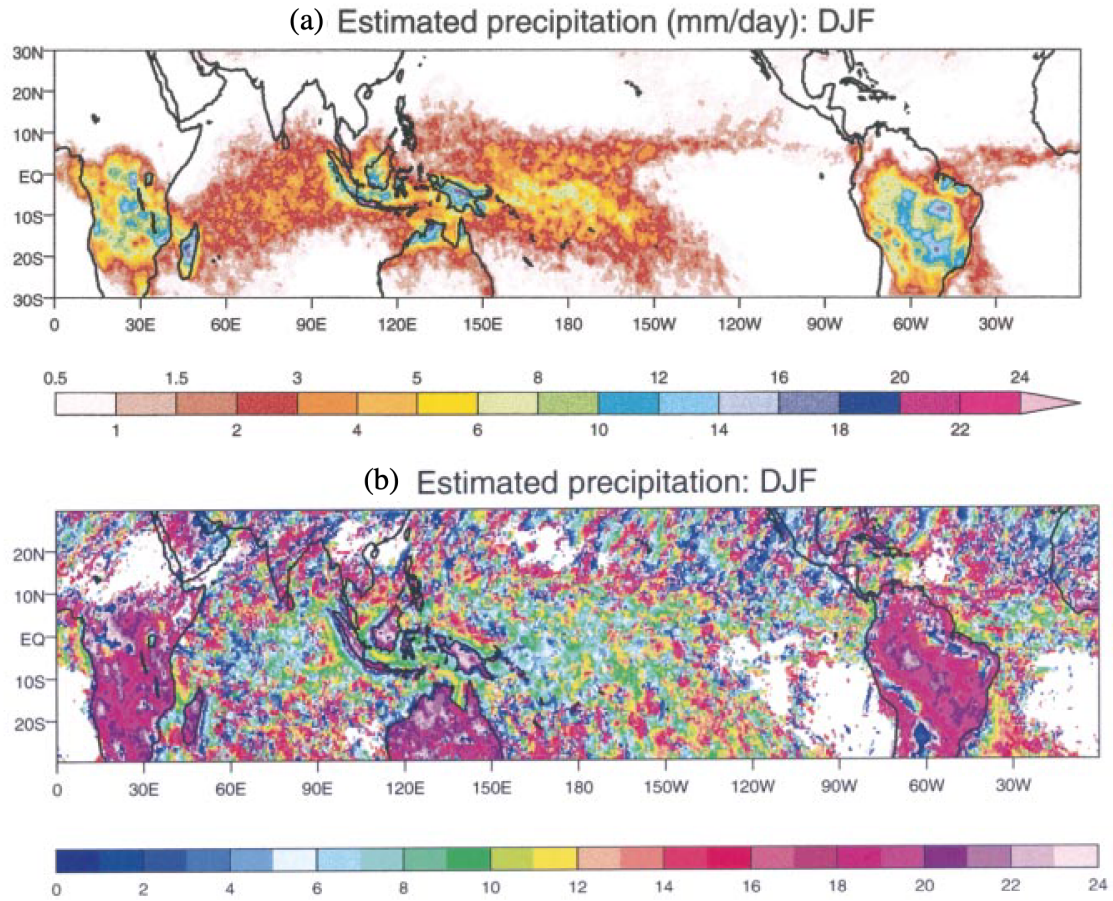

Figure 1.8: The (a) amplitude and (b) phase (in LST) of the first diurnal harmonic of estimated precipitation based on early CLAUS data in the boreal winter (DJF) season. *Image adapted from Yang & Slingo (2001), Figures 2&3.*

of maximum precipitation and the phase of the FDH, of multiple hours in some places (Figure 1.9). However, the diurnal range and time of maximum precipitation are also only useful to an extent, with the nature of the 24-hour diurnal variability not well constrained by these characteristics alone and often relying on inference (Figure 1.10). There is some evidence of offshore phase propagation away from some coastlines, particularly when the FDH phase characterisation is considered (e.g. Figure 1.8b) — the clearest examples include southwest of Sumatra, northwest of Borneo and north of New Guinea — with a near-sunrise precipitation maximum near the coast propagating toward a midday maximum a couple of hundred kilometres offshore. However, since the FDH phase is not a reliable indicator of the time of maximum precipitation, and the propagation cannot be well resolved using the time of maximum precipitation at the 3 hour resolution of TRMM, accurate and meaningful characterisation of phase propagation is not straightforward.

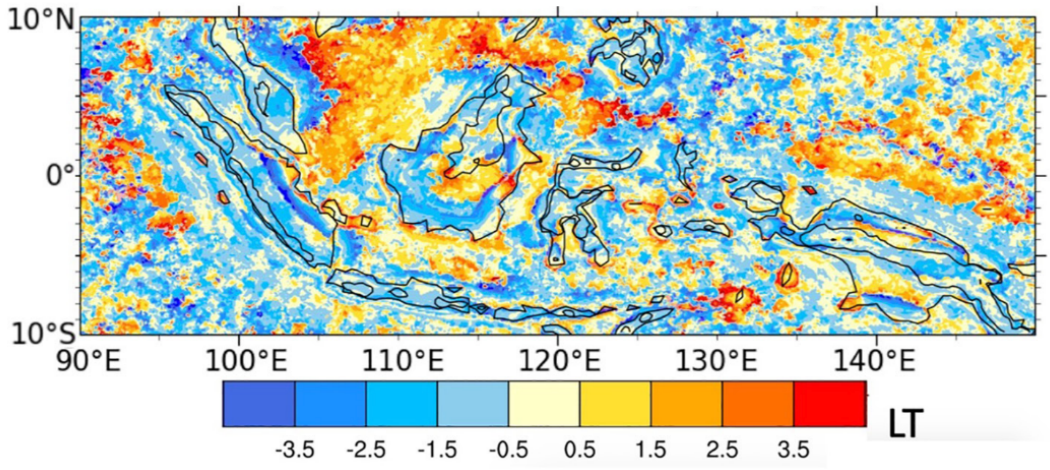

Figure 1.9: The time difference between the first diurnal harmonic (FDH) phase and the time of maximum precipitation in an IMERG composite. Negative values (blue) indicate that the FDH phase is too late. *Image adapted from Bai & Schumacher (2022), Figure 6.*

The TRMM satellite was superseded by a satellite associated with the Global Precipitation Measurement (GPM) mission, which launched in 2014 (Huffman et al., 2015). Advances in integration algorithms, sensor capabilities and resolution have allowed for the development of a yet higher-resolution precipitation data product, the Integrated Multi-Satellite Retrievals for GPM (IMERG). IMERG quantified precipitation at a 0.1° by 0.1° spatial resolution and to a greatly improved temporal resolution of 30 minutes. Relative to TRMM 3B42, IMERG improves on the temporal resolution of global precipitation by a factor of 6, with 48 measurements per day as opposed to 8. Since precipitation rate can fluctuate on a much shorter timescale than 3 hours, with this advancement comes great potential to resolve and characterise rapid intensification and/or weakening of precipitation during the DC in greater detail. A range of field campaigns have been conducted in recent years under the Years of the Maritime Continent (YMC) program (e.g. Yoneyama & Zhang, 2020), which aims to provide a comprehensive observational data set across the MC against which high-resolution satellite data products such as IMERG may be validated. A better characterisation of the DC of precipitation would be beneficial for two main reasons: firstly, it would provide a more thorough benchmark against which a simulated DC of precipitation (which itself is often output at hourly resolution or better) may be compared, and secondly, it would allow for improved characterisation of the sensitivity of the observed DC to other dominant modes of tropical weather variability, thereby facilitating more

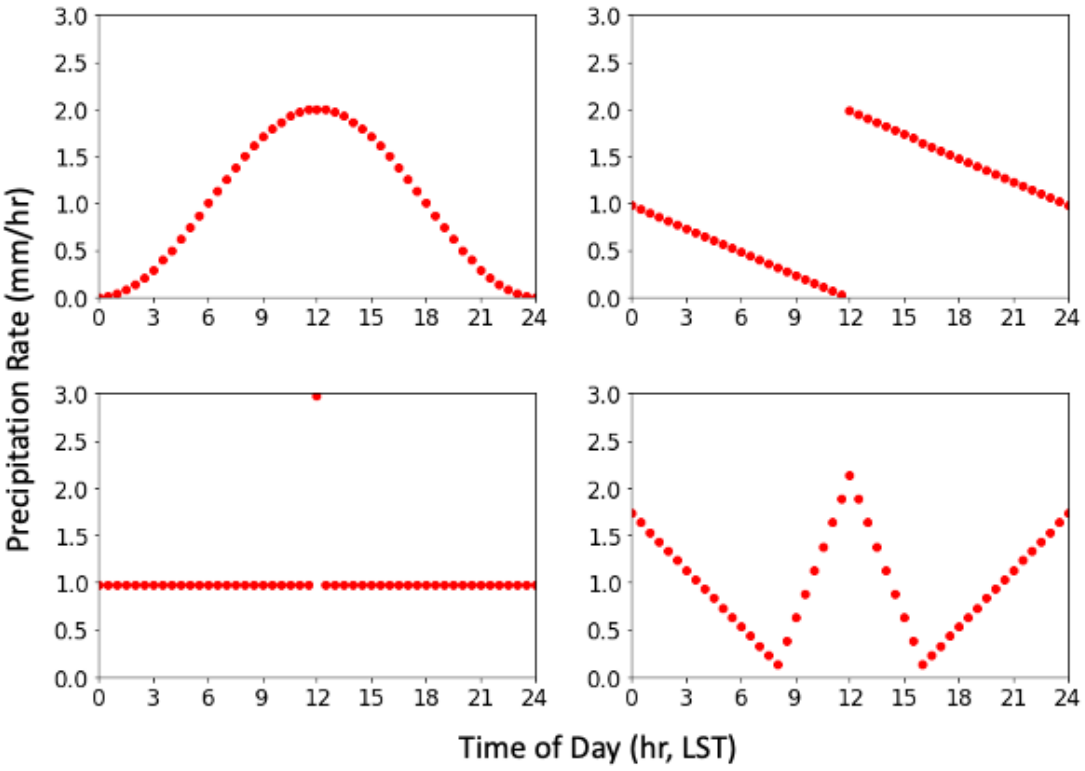

Figure 1.10: Illustration of the uncertainty associated with characterisation of the DC using the diurnal range and the time of maximum precipitation. All four (extreme) idealised DCs shown have the same diurnal range, time of maximum precipitation and mean precipitation, but the nature of diurnal variability varies greatly.

accurate insight into the nature of the scale interactions of the DC. A primary aim of the *TerraMaris* project, by which the studentship supporting this research was supported, was to contribute a large-scale coordinated field campaign observing many weather variables through the atmosphere and surrounding waters of the western MC. Regrettably, this field campaign had to be cancelled, ultimately as a consequence of the global Covid-19 pandemic, however a broad suite of supporting regional hindcast model runs were performed under the project in order to contribute to the state of understanding of the strengths and limitations of weather models across the MC (Howard et al., in review).

Model skill at simulating observed diurnal variability across the MC was identified as a crucial weakness several years ago (e.g. Neale & Slingo, 2003; Slingo et al., 2003), and significant simulation challenges persist to present. In coarse-gridded global climate models (GCMs), the islands of the MC register as only a small handful of grid cells, with maximum precipitation typically occurring around midday over these land cells, in phase with maximum solar radiative forcing. A number of studies analysing the DC of higher resolution

GCMs and regional climate models have demonstrated that DC simulation skill scarcely improves, if at all, as horizontal grid spacing is reduced down to around 10 km (e.g. Dirmeyer et al., 2012; Ban et al., 2014; Baranowski et al., 2019); maximum precipitation over land still occurs approximately six hours too early as the observed lag between the maximum in solar radiative forcing and in precipitation is not captured (Figure 1.3b; Love et al., 2011), however the DC amplitude and general precipitation climatology do tend to improve with resolution. A marked improvement in DC simulation, alongside other modes of variability and the mean state, occurs once the horizontal grid spacing is reduced to 5 km or less (e.g. Birch et al., 2016; Vincent & Lane, 2017; Argüeso et al., 2020; Xue et al., 2020); at this resolution, key processes governing deep convection and cloud formation can be explicitly resolved, so need not be approximately represented by a convection parametrisation scheme. Model errors in the phase of the DC influence regional radiation budgets — too much cloud in the model around midday when ISWR is strongest is likely to result in too little surface-level heating, which will impact on the mean state and triggering of convection. There has been much research dedicated toward tweaking (or overhauling) the convection parametrisation scheme in order to decouple the precipitation maximum from the solar radiative forcing maximum (e.g. Rio et al., 2009; Grandpeix & Lafore, 2010; Sane et al., 2012; Chao, 2013), with some demonstrable improvements to the amplitude and phase of the simulated DC of precipitation in convection-parametrised models as a result. However, such tweaks often have a uniform spatial effect, so still fail to characterise detailed phase variability over land, and they are liable to inadvertently worsen the representation of other elements of precipitation variability. As such, some operational models continue to utilise convection parametrisation schemes that do not simulate the phase of the DC over the MC remotely faithfully.

The scale interactions between the DC and longer-period modes of tropical weather variability have been a further key topic of interest. Perhaps the most intuitive scale interaction is that between the DC and the annual cycle (e.g. Worku et al., 2019; Lu et al., 2021) — the annual cycle over the MC features a monsoon season during the boreal winter months, bringing especially high mean precipitation during this wet season and inducing an especially strong DC. The potential for local extreme weather and the influence of MC weather on global circulation patterns are therefore heightened during these months, and as such, much research including that presented within this thesis focuses on the

wet season from December to February (DJF). The characteristics of the DC over the MC, particularly phase propagation characteristics, are also dependent on the large-scale background conditions, including wind direction (e.g. Peatman et al., 2021), and these large-scale conditions are influenced by modes of tropical weather variability including ENSO, the MJO, tropical cyclones, CCKWs and equatorial Rossby waves — which all also interact with one another (Figure 1.5). The ultimate goal is to understand how all of these major modes of variability simultaneously interact, however it is first necessary to understand how each pair of modes of variability interacts. The works herein discuss some elements of the scale interaction between the DC and the MJO.

1.4 The Madden-Julian Oscillation

While the DC is the dominant mode of short-term precipitation variability over the MC, the MJO is the dominant mode of precipitation variability at intra-seasonal timescales. First identified in the early 1970s (Madden & Julian, 1971 & 1972), recognition for the importance of the MJO in the global weather and climate system and the challenges faced in faithfully simulating its characteristics has continually grown since. A good proxy for MJO research interest is the number of citations received by the original discovery paper; having steadily become more popular through the decades, every year within the most recent decade at the time of writing saw at least 100 known studies citing Madden & Julian (1971). To account for this acceleration in research interest, review articles summarising the diversity of literature on observational, modelling and theoretical MJO studies have been produced with ever-increasing frequency (e.g. Madden & Julian, 1994; Zhang, 2005; DeMott et al., 2015; Jiang et al., 2020; Zhang et al., 2020).

The initial observation of MJO variability was in zonal winds in the lower and upper troposphere (850 hPa and 150 hPa respectively); Madden & Julian (1971) studied a time series of horizontal wind velocity from rawinsonde data from over Canton Island in the central Pacific Ocean (3°S, 172°W), and noted a broad spectral peak in the frequency range corresponding to an intra-seasonal period of 41–53 days at each of these pressure levels. Such a strong spectral peak was not observed at intermediate tropospheric pressure levels, nor was it observed in the meridional component of wind at any pressure level — as such, the responsible circulation pattern was considered to operate primarily in the

zonal plane, much like a Walker circulation cell. The spectral peak has too low a frequency to be associated with any of the theoretical modes of tropical wave that the authors had intended to investigate (Matsuno, 1966; Gill, 1980), but too high a frequency (and too broad a range) to be a product of the seasonal cycle. Upon extending their analysis to several other tropical locations and comparing the phases of intra-seasonal spectral peak relative to that at Canton Island, Madden & Julian (1972) identified an eastward-propagating signal along the equator (with a slow component of propagation outward away from the equator in either direction), strongest within ten degrees of the equator and between the Indian and Pacific Oceans.

A schematic of the MJO cycle in the 1972 study, reproduced here in Figure 1.11, illustrates the speculated gross properties of the MJO with sufficient accuracy that it remains a useful summary of the MJO cycle over 50 years later. An "MJO event" tends to initiate over the Indian Ocean; low surface pressure develops in association with a broad region — or "envelope" — of organised convection, with a mean updraft accompanied by lower-tropospheric convergence and upper-tropospheric divergence. An opposite pattern of high surface pressure with lower-tropospheric divergence, upper-tropospheric convergence and a mean downdraft over the western-central Pacific Ocean complements the active MJO event over the Indian Ocean. The MJO active envelope propagates eastward, typically intensifying over the MC and weakening somewhere over the Pacific Ocean, as represented by the cloud shape in each of the panels of the schematic. In-situ, any affected location therefore experiences a cycle between enhanced organised convection during the active MJO phase and suppressed organised convection when the MJO is active over a different longitude.

In the years since the initial speculative description of the MJO, a wealth of satellite-borne observations and dedicated field campaigns have allowed for its characteristics to be described in greater detail (e.g. Waliser et al., 2012; Yoneyama et al., 2013; Xu & Rutledge, 2014). Based on observations of outgoing long-wave radiation (OLR) as an indicator of cloud top height, Nakazawa (1988) was able to establish the organisational hierarchy within an MJO active envelope (Figure 1.12); the active envelope comprises several super-clusters of cloud, each with a typical length scale of several thousand kilometres, a lifespan of up to 10 days and an eastward-propagating signal. Each super-cluster comprises several individual cloud clusters, each typically lasting 1–2 days, spanning a length scale on the order of hundreds of kilometres, and advecting westward with the

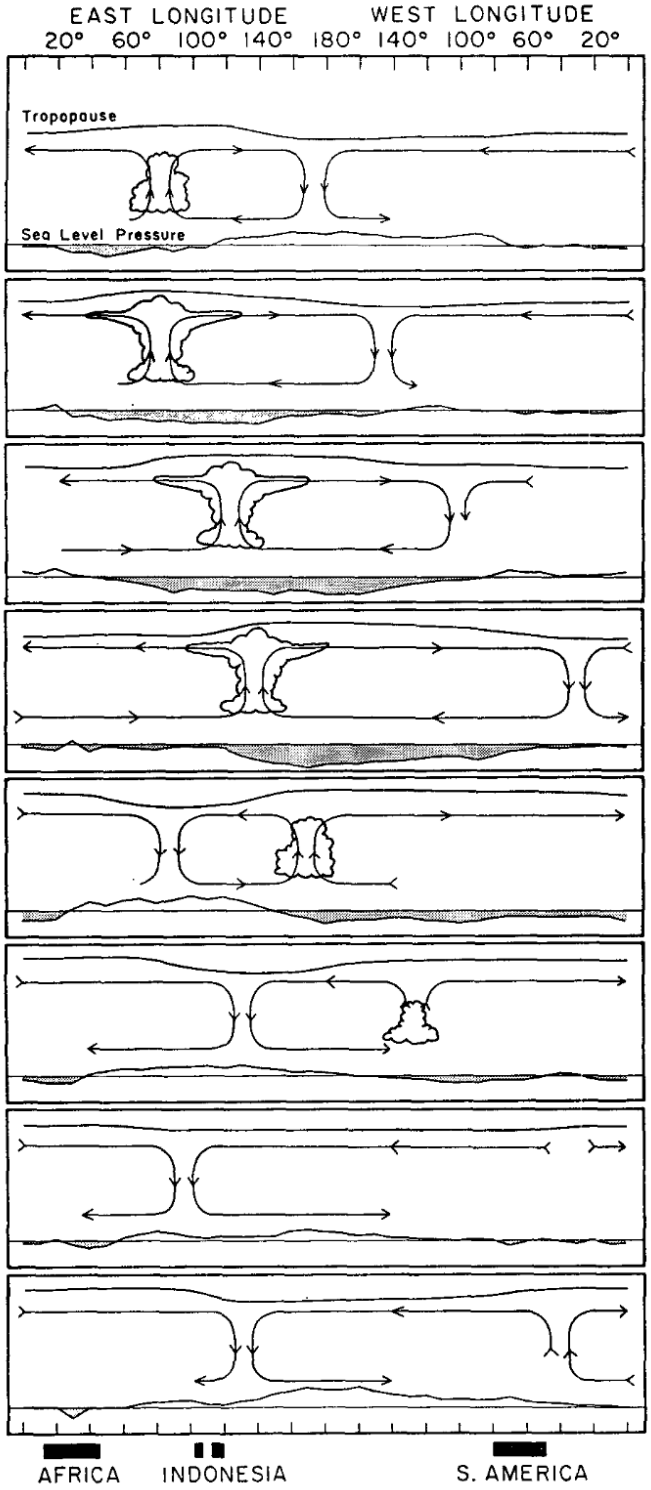

Figure 1.11: Schematics of circulation in the zonal plane associated with an MJO event as it propagates eastward (panels progress downwards). Deep convection is indicated by the large cloud over the MC in the second to fourth panels, while smaller clouds in the adjacent panels indicate shallow convection. Lines at the top and bottom of each panel represent the relative tropopause height and sea level pressure. *Image adapted from Madden & Julian (1972), Figure 16.*

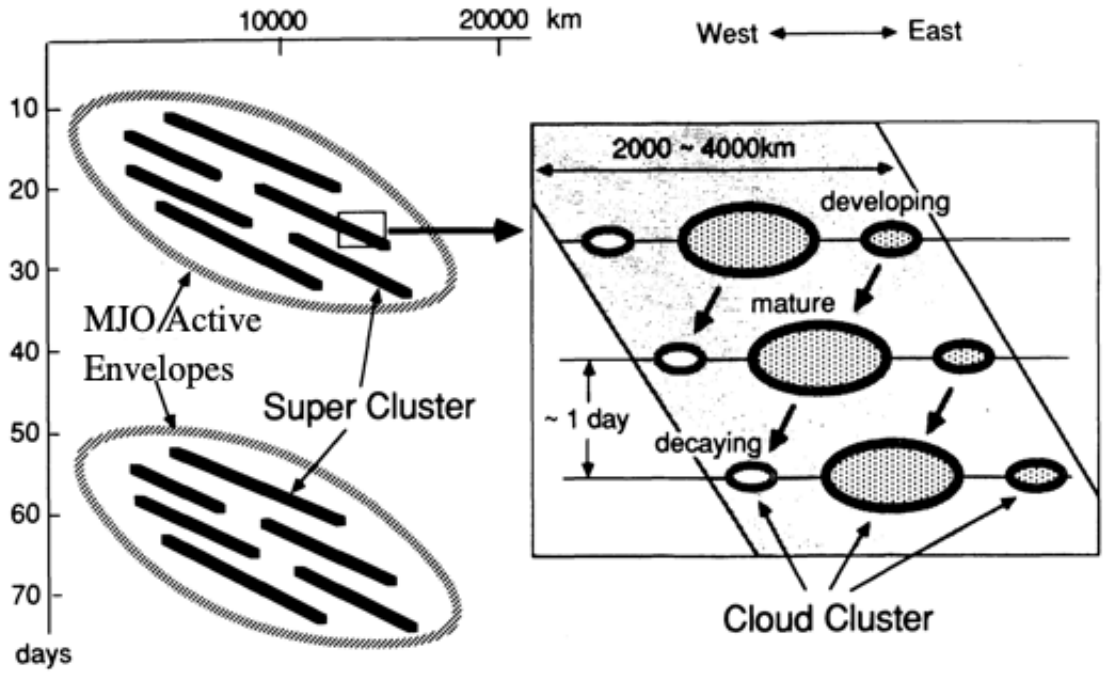

Figure 1.12: Schematic representation of the hierarchy of organisation of convection and clouds within an active envelope of the MJO. Each eastward-propagating MJO contains several super-clusters which propagate eastward with a comparable phase speed. Each super-cluster contains several clusters which propagate westward, with initiation of new clusters occurring on the eastward edge of the super-cluster. *Image adapted from Nakazawa (1988), Figure 5.*

prevailing tropical easterly winds. The successive formation of clusters within a super-cluster tends to occur on the eastern edge of the super-cluster, producing eastward propagation of the super-cluster despite the westward advection of the individual clusters. As such, key theoretical questions about the MJO concern the mechanism behind the formation of new cloud clusters on the eastern edge of existing super-clusters, and the influences governing the planetary scale and (variable) frequency of MJO events (Zhang, 2005).

A quantitatively rigorous explanation of the MJO, accounting for its full range of key characteristics, remains elusive despite the wide range of hypotheses and theories that have been presented across the years. Zhang et al. (2020) summarise four of these theories: skeleton theory (Majda & Stechmann, 2009), moisture-mode theory (Adames & Kim, 2016), gravity-wave theory (Yang & Ingersoll, 2013), and trio-interaction theory (Wang et al., 2016). Certain influences are, however, widely considered essential in their contribution to MJO characteristics, such as coupled ocean influences (e.g. DeMott et al., 2015), moist convective processes (e.g. Sobel & Maloney, 2013) and interactions with the

complex MC archipelago (e.g. Wu & Hsu, 2009). For the works presented in this thesis, the interactions of the MJO with the MC are of greatest significance due to diurnal activity being most strongly focused around the MC. The eastward propagation of the MJO over the MC is much less steady than over the Indian Ocean; the disruptive influence of the MC is often described as the "barrier effect" (e.g. Salby & Hendon, 1994; Seo & Kim, 2003; Kim et al., 2014; Kerns & Chen, 2016). Zhang & Ling (2017) demonstrated the frequent blocking of the MJO over the MC, with approximately 50% of MJO events initiated over the Indian Ocean terminating over the MC, and the majority of events that successfully cross the MC are weakened. This is one element of understanding of the MJO life cycle that has shifted since its discovery, as Madden & Julian (1972) originally suggested that MJO convection typically strengthens during passage over the MC (Figure 1.11). A range of mechanisms for the MC barrier effect have been proposed, including physical blocking by topography (e.g. Wu & Hsu, 2009; Kim et al., 2017), reduced moisture fluxes replenishing the lower troposphere due to lower sea surface coverage (e.g. Sobel et al., 2010; Birch et al., 2016), westward propagation of anomalously dry air from over the central Pacific Ocean (e.g. Feng et al., 2015; DeMott et al., 2018) and other causes of weakened zonal gradient in moisture (e.g. Gonzalez & Jiang, 2017; Ahn et al., 2020b; Kang et al., 2021), and disruption of the large-scale MJO environment by the DC-dominated convective activity over the MC (e.g. Hagos et al., 2016; Ling et al., 2019b; Savarin & Chen, 2023).

MJO representation was (to varying extents) inaccurate, or even absent, in many GCMs earlier in the century (e.g. Neale & Slingo, 2003; Zhang, 2005; Hung et al., 2013). Simulation of variability resembling the MJO has become more common among GCMs within the latest decade, allowing for a greater diversity of studies on the key characteristics of the simulated MJO, such as its frequent blocking over the MC (e.g. Jiang et al., 2015; Peatman et al., 2015; Ling et al., 2019a; Ahn et al., 2020a). Many models exaggerate the barrier effect of the MC, resulting in MJO active envelopes propagating into the western Pacific too infrequently (e.g. Inness & Slingo, 2003; Seo et al., 2009; Vitart & Molteni, 2010). Global teleconnection responses to MJO activity in the western Pacific are especially impactful (e.g. Adames & Wallace, 2014; Ungerovich et al., 2021; Skinner et al., 2022), therefore model misrepresentation of MJO activity over this region is especially detrimental to global medium-range forecasting. In recent years, modelling studies investigating the contribution of the DC to inaccurate MJO propagation over the MC have become more common (e.g. Oh et al., 2013;

Hagos et al., 2016; Zhou et al., 2021; Tan et al., 2022; Savarin & Chen, 2023); for instance, Hagos et al. (2016) demonstrated a greater (more realistic) proportion of MJO events crossing the MC when the DC was inhibited by fixing ISWR at the top of the atmosphere to the daily mean value.

Many other studies have investigated the reciprocal downscale component of the scale interaction of the MJO on the DC over the MC (e.g. Tian et al., 2006; Suzuki, 2009; Rauniyar & Walsh, 2011; Oh et al., 2012; Virts et al., 2013; Peatman et al., 2014; Vincent & Lane, 2016; Sakaeda et al., 2017; Szkolka et al., 2023). This wealth of research reflects the outstanding uncertainties concerning this interaction; many studies have found that maximum DC amplitude slightly leads maximum mean MJO-induced precipitation (e.g. Peatman et al., 2014; Vincent & Lane, 2016; Sakaeda et al., 2017; Lu et al., 2019), though some studies have suggested that, over land, the DC tends to be weaker within the active envelope of the MJO (Sui & Lau, 1992; Oh et al., 2012). There is a yet weaker consensus on whether the phase of the DC systematically varies through an MJO cycle (e.g. Chen & Houze, 1997; Fujita et al., 2011; Rauniyar & Walsh, 2011; Oh et al., 2012; Virts et al., 2013; Sakaeda et al., 2017) or is essentially consistent (e.g. Tian et al., 2006; Suzuki, 2009; Lu et al., 2019; Szkolka et al., 2023).

Due to lack of consensus on its precise fundamental characteristics, objective definition of the MJO has proved troublesome. In the early decades following the discovery of the MJO, there was a distinct absence of universally accepted definition of the phenomenon, leading to studies individually defining the MJO according to somewhat inconsistent criteria. For instance, Madden & Julian (1971) define the mode of variability as having a frequency range from 41–53 days, but more loosely refer to it as the "40–50 day oscillation", and subsequent studies considered a range of portions of the frequency spectrum between less than 30 and more than 60 days (e.g. Krishnamurti & Subrahmanyam, 1982; Weickmann et al., 1985). Li et al. (2005) suggest a latitudinal dependence of the dominant intra-seasonal frequency, increasing from 20–30 days on the equator to 60–90 days at 20°N/S.

In time, Wheeler & Hendon (2004) developed an MJO metric — the real-time multivariate MJO (RMM) index, characterising the MJO by amplitude and phase — that has been widely used in the decades since, allowing for a more consistent definition of the MJO. The RMM index is built on the tropical patterns of OLR and zonal wind at the 200 hPa and 850 hPa pressure levels, with the first two empirical orthogonal functions (EOFs) calculated based on the combined multivariate field after variability associated with the seasonal cycle, ENSO

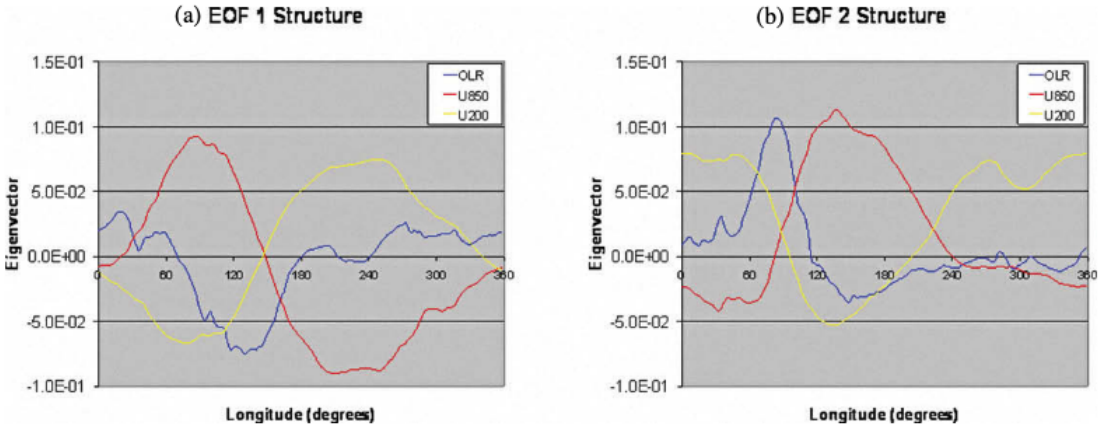

Figure 1.13: Multivariate structures of (a) EOF1 and (b) EOF2, onto which the multivariate anomaly field is projected to determine the magnitude of RMM1 and RMM2 on any given day. *Image adapted from Gottschalck et al. (2010), Figure 1.*

and remaining amalgamated long-term modes of variability are removed. On any given day, the anomalous multivariate field can be projected onto the two EOFs to determine the magnitudes of the two leading principal components, RMM1 and RMM2. A positive value of RMM1 places the active envelope of the MJO — identified by a negative anomaly in OLR, a positive gradient in lower-tropospheric zonal wind (U850) with longitude and a negative gradient in upper-tropospheric zonal wind (U200) with longitude — over the MC and the most suppressed MJO activity over Africa and/or the eastern Pacific Ocean, and vice versa for negative values (Figure 1.13a; Gottschalck et al., 2010). Similarly, a positive value of RMM2 places the active envelope of the MJO over the western Pacific Ocean and the most suppressed MJO activity over the Indian Ocean, and vice versa for negative values (Figure 1.13b; Gottschalck et al., 2010). As such, a typical MJO cycle is reflected as a cycle through negative RMM1, negative RMM2, positive RMM1, positive RMM2, and back to negative RMM1. The 2-D phase space of RMM1 and RMM2 is divided into eight regions (Figure 1.14), tracking the typical MJO cycle from MJO phase 1 with the MJO active envelope over east Africa and the western Indian Ocean, through to MJO phase 8 over the central-eastern Pacific Ocean (Figure 1.15). Figure 1.14 shows the RMM phase space time series for a three-month period from January to March 2020; an MJO event initiates around January 6^{th} in phase 4, intensifies over the MC and western Pacific, then decays in phase 7 around January 25^{th}. February then saw a period of generally inactive MJO, followed by a weaker MJO event in early March that did not propagate as far east as the January event, but was followed very shortly by another MJO event initiating around March 18^{th}

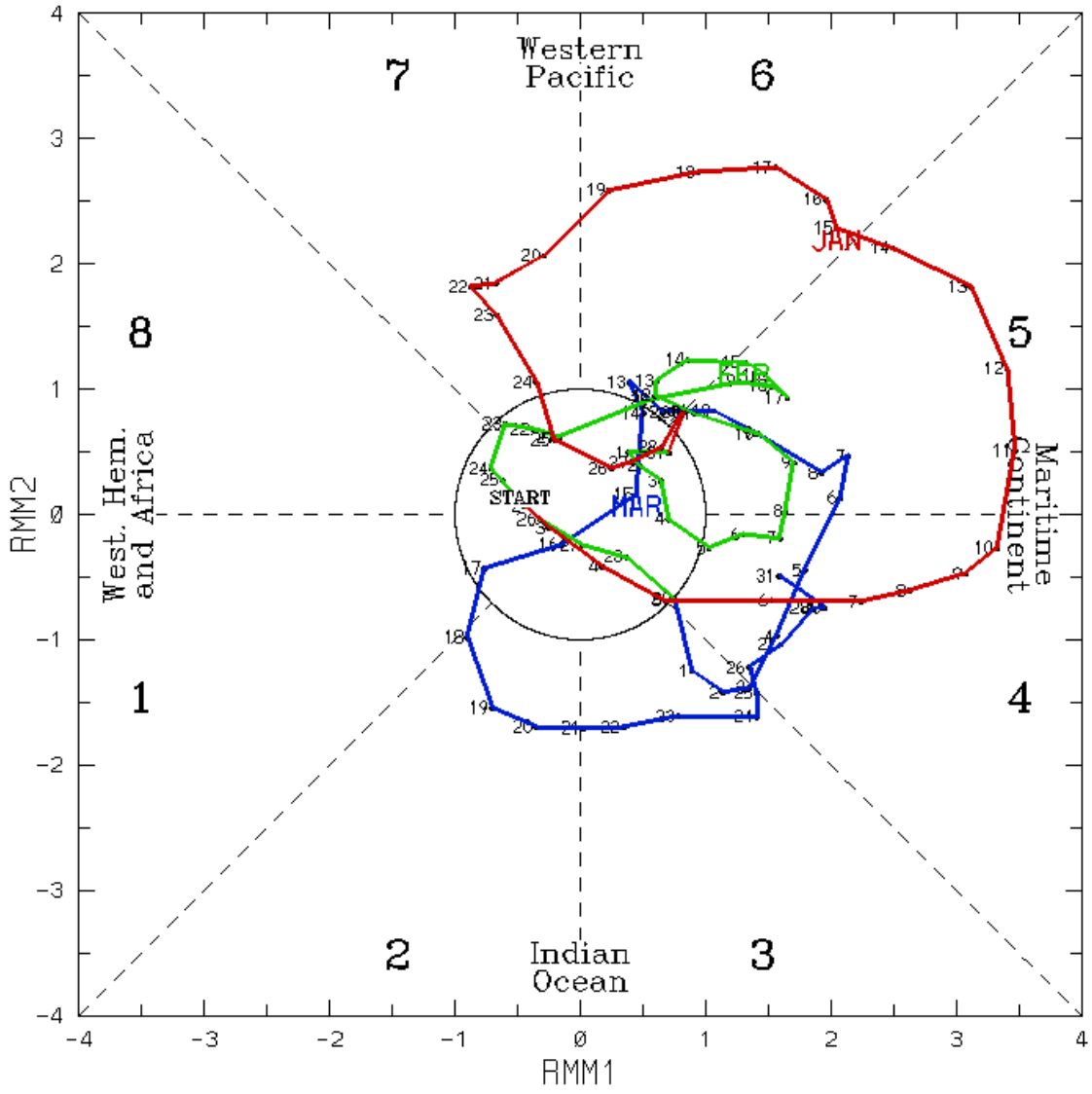

Figure 1.14: Representation of the RMM index in 2-D phase space. In Cartesian coordinates, RMM1 and RMM2 are plotted on the x- and y-axis, respectively. In polar coordinates, the amplitude (distance from the centre) indicates the MJO strength and the phase (direction from the centre) indicates the longitude of the MJO active envelope, as labelled. Phases 1–8 of the MJO are marked. The inner circle, with amplitude below 1, indicates an inactive period of the MJO. The red, green and blue lines show the evolution of the RMM index through January, February and March 2020, respectively. *Image adapted from* http://www.bom.gov.au/climate/mjo, *maintained by the Australian Bureau of Meteorology*.

in phase 2. This three-month period exemplifies the irregular nature of the MJO; despite its name, it should not be considered a regular oscillation, as the duration between consecutive MJO events may be highly variable, and there is substantial variability in the nature and strength of individual MJO events. An MJO event may initiate further east than phase 1 or terminate further west than phase 8, however, a transition from phase 8 to phase 1 at high amplitude, as in March 2020, implies a "successive MJO event" (Matthews, 2008); immediate development of a new MJO active envelope following decay of the preceding envelope. A range of alternative MJO indices have been developed, with differences in selected meteorological variables considered and in the precise data treatment methodology (e.g. Kikuchi et al., 2012; Ventrice et al., 2013; Kiladis et al., 2014); different indices tend to slightly differ in their definition of the MJO amplitude and phase at any time. Ultimately, there is a degree of situational dependence concerning which index is most appropriate for which research question.

1.5 Research Questions

The following key research questions (RQs) concerning the DC of precipitation are considered through this thesis:

1. Does improved spatio-temporal resolution of the DC of precipitation allow for more complex features to be identified than in previous research?
2. To what extent can either a *convection-parametrised* model or a *convection-permitting* model succeed at faithfully simulating the complex features of the observed DC of precipitation, and what are the nature and likely dynamical causes of any differences?
3. What is the nature of the influence of the MJO on the manifestation of the DC of precipitation, and in how much detail is it possible to resolve this scale interaction?

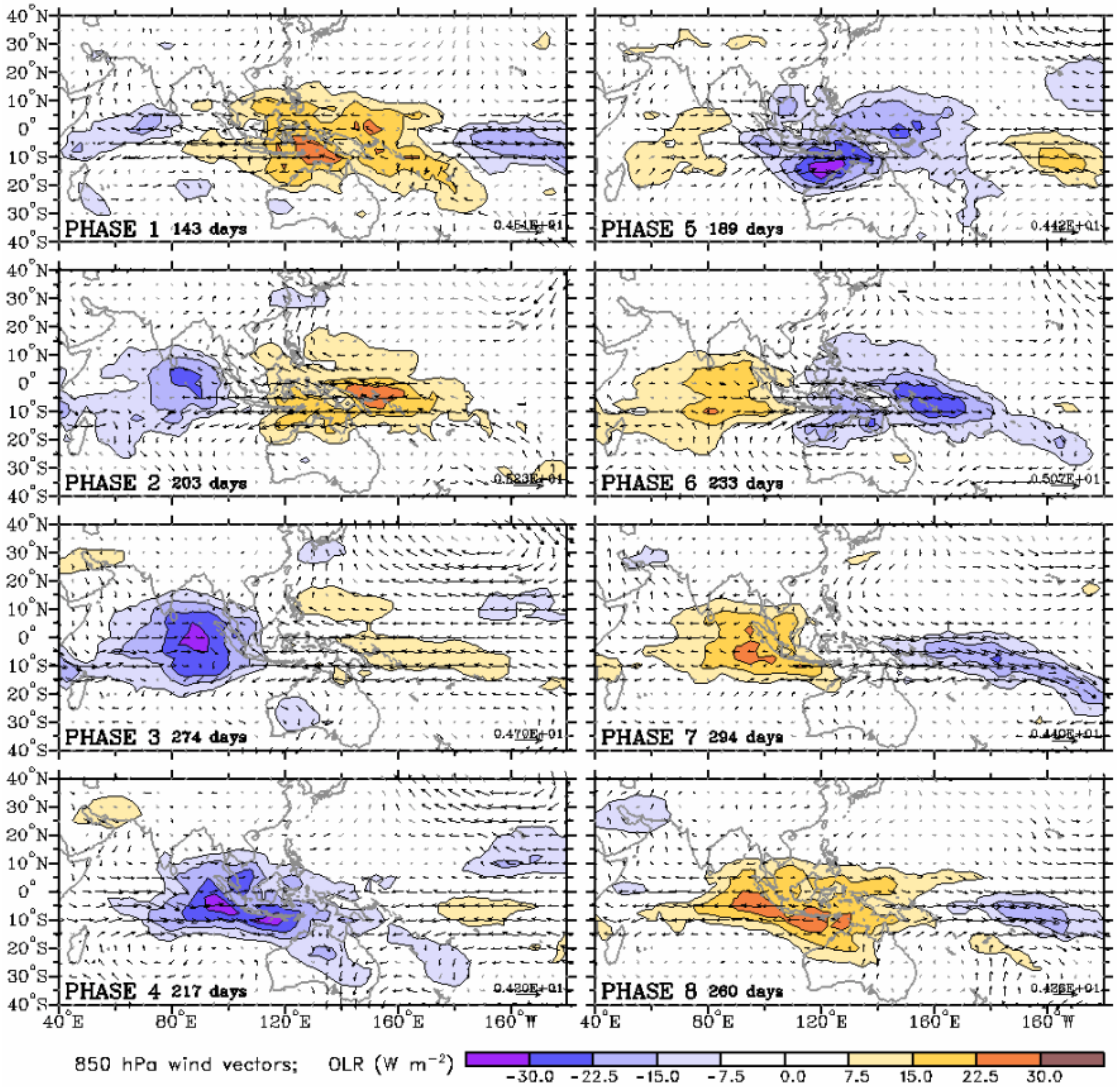

Figure 1.15: Illustration of the spatial structure of each of the eight phases of the MJO as defined by the RMM index of Wheeler & Hendon (2004). Shading indicates the anomaly in OLR (the "active envelope" is centred around the negative OLR anomaly), and arrows denote horizontal wind vector anomalies at the 850 hPa pressure level. *Image adapted from* http://poama.bom.gov.au/project/maproom/RMM/composites/index.html, *maintained by Matthew Wheeler*.

1.6 Thesis Outline

This thesis contains four further chapters. Chapter 2 considers the DC of precipitation observed in high-resolution satellite data and characterises the key spatio-temporal features of the DC in greater detail than previous DC studies using lower-resolution data have been at liberty to do. Chapter 3 uses the benchmark characterisation established in Chapter 2 to scrutinise the DC simulated by both a convection-parametrised and a convection-permitting configuration of the UK Met Office Unified Model (MetUM). Chapter 4 documents an analysis of the downscale influence of the MJO on the observed DC, in order to provide a benchmark against which simulated scale interactions may be contrasted. Finally, a holistic discussion and synthesis of results is presented in Chapter 5.

Chapter 2

Characterisation of the observed diurnal cycle of precipitation over the Maritime Continent

2.1 Preface

The work in this chapter has been recently published in the Quarterly Journal of the Royal Meteorological Society (Mustafa et al., 2024), and at the time of final thesis submission is available to view online via early access. No substantial alterations have been made for this chapter, therefore some introductory content from Chapter 1 is repeated. This chapter is the sole work of the candidate, with the supervisory team listed as co-authors for their supervisory role.

2.2 Introduction

The Maritime Continent (MC) is the name given to the archipelago situated in the Indo-Pacific warm pool between Southeast Asia and Australia. It features islands of a range of sizes, many with complex topography, interspersed among shallow shelf seas which are some of the Earth's warmest (e.g. Zhang et al., 2016; Roxy et al., 2019; Yin et al., 2022). Mean humidity and precipitation rates across the MC are also among the highest observed globally (e.g. As-syakur et al., 2016). The mean diurnal cycle (DC) features extreme contrasts between maximum and minimum rates of precipitation, particularly over land and near-coastal marine regions, with near-coastal land typically

experiencing maximum mean precipitation between the late afternoon and evening, near-coastal waters experiencing maximum mean precipitation shortly after midnight, and waters further offshore experiencing an increasingly late mean precipitation maximum up to late morning (e.g. Love et al., 2011; Sakaeda et al., 2017; Worku et al., 2019). The DC of convection, to which the DC of precipitation is coupled, is dominantly driven by land–sea breeze dynamics which are generated by the differential in surface warming and cooling rates between land and water surfaces under the intense equatorial DC of solar radiative forcing (e.g. Mori et al., 2004; Kikuchi & Wang, 2008).

The DC is a high-frequency mode of tropical weather variability that is landlocked over the MC. Lower-frequency modes of tropical variability that propagate along the equator, including the eastward-propagating Madden-Julian Oscillation (MJO; Madden & Julian, 1971 & 1972; Zhang, 2005) and convectively-coupled equatorial Kelvin waves (CCKWs; e.g. Kiladis et al., 2009), modulate and are modulated by the DC as they propagate into the MC area (e.g. Oh et al., 2012; Peatman et al., 2014; Birch et al., 2016; Lu et al., 2019; Worku et al., 2020). The probability of a CCKW successfully propagating across the MC has been shown to be highly dependent on whether its arrival time at the islands of the MC is in phase with active diurnal convection (Baranowski et al., 2016). Furthermore, there is increasing support for the hypothesis that a strong DC over the MC is an integral component of the so-called "barrier effect" experienced by the MJO over the MC (e.g. Zhang & Ling, 2017; Ling et al., 2019b; Zhou et al., 2021); evidence to the contrary is also still emerging (e.g. Seiki et al., 2021), however all studies agree that the strength of the DC influences the MJO in some manner. Since the convectively active envelope of an MJO event frequently contains CCKW components (Kikuchi et al., 2018), it follows that the fate of an MJO active envelope as it interacts with the DC is highly sensitive to both the amplitude and phase of the DC. This sensitivity has implications for global medium-range weather forecasting, as the inability of a model to generate an accurate DC will limit the degree to which the widespread medium-range predictability offered by MJO dynamics can be harnessed (Cassou, 2008; Skinner et al., 2022).

Although coarse-gridded general circulation models still show mixed skill concerning the simulation of an accurate DC (Baranowski et al., 2019), high-resolution regional models have become increasingly capable of generating a DC that reflects the observed DC quite well (Bhatt et al., 2016). There is, therefore, an increased need to be able to characterise the complexities of the

DC beyond the first-order pattern (i.e. an amplitude and a phase) in order to provide an accurate benchmark against which to assess model performance to facilitate further improvements. With the availability of over two decades of high-resolution gridded satellite precipitation data at the time of this study, there is potential to refine the characterisation of the DC in order to capture more of the spatio-temporal complexities that cannot be fully encapsulated with a two-parameter (amplitude and phase) characterisation.

The first diurnal harmonic (FDH) is a reasonable simplification of the DC in most locations across the MC as it represents the single 24-hour oscillation between a diurnal precipitation maximum and minimum that is generally observed, and has been used widely in the past (e.g. Yang & Slingo, 2001; Peatman et al., 2014 ;Birch et al., 2016; Seiki et al., 2021). Using a simple waveform to approximate the DC at a location has the two main benefits of noise suppression and characterisation of the full 24-hour composite cycle. Studies that use only the diurnal range (difference between maximum and minimum precipitation) and the time of maximum precipitation are not able to constrain the details of the 24-hour cycle very well except for the maximum, which can complicate dynamical interpretation of the local DC. Bai & Schumacher (2022) note that precipitation events tend to approximate more closely to brief instantaneously-initiating pulses than to sinusoidally-varying oscillations, particularly where the precipitation is associated with the triggering of deep convection. As such, a waveform which is more adaptable to sharp temporal gradients in precipitation rate may offer a more appropriate approximation. The primary purpose of this study is to demonstrate the application of two novel waveforms developed to be able to capture and intuitively characterise rapid transitions in precipitation rate.

The remainder of this article is structured as follows: Section 2.3 details the data used in this study. Section 2.4 describes the observed DC with the use of the diurnal range and time of maximum, and notes some complexities of the DC which are difficult to resolve with these characteristics alone. Section 2.5 describes the DC with the use of the FDH parameters and notes how and where this description is especially misleading. Section 2.6 introduces two novel waveforms trialled for a more accurate characterisation and gives an overview of the output of these new characterisation methods. Section 2.7 discusses the benefits and complications of the new characterisation methods, and describes how the new results might be interpreted and applied to other fields. Conclusions are presented in Section 2.8.

2.3 Data

The current state-of-the-art high-resolution satellite-derived precipitation data product, the Integrated Multi-satellite Retrievals for GPM (IMERG) v06B final run, is used (Huffman et al., 2015). Having stitched together data from the Tropical Rainfall Measuring Mission (TRMM) satellite (active 1997 — 2015) and the Global Precipitation Measurement (GPM) satellite (active 2014 — present), and having reprocessed the TRMM data to match the higher spatial and temporal resolution of GPM, IMERG v06B offers over two decades of global precipitation data with a 30-minute temporal resolution and a 0.1° by 0.1° spatial resolution. The temporal resolution of IMERG improves sixfold on the resolution of the TRMM 3B42 data product used in previous studies (e.g. Peatman et al., 2014; Sakaeda et al., 2017; Lu et al., 2019), allowing for more detailed investigation into the temporal characteristics of the observed DC of precipitation across the MC than has been possible until recently. The IMERG data product is constructed using the core GPM satellite as a reference standard according to which data from the additional passive microwave (PMW) sensors in the GPM satellite constellation is calibrated (Tan et al., 2019b). For most PMW sensors, the brightness temperature recorded is fed into the Goddard profiling algorithm (Kummerow et al., 2001 & 2015) which also considers surface temperature, surface class and total column water vapor. Data quality is supported by calibration against monthly rain gauge accumulations, and the high resolution of IMERG v06B is achieved by filling gaps in satellite observations according to an interpolation algorithm based on motion vectors calculated from total column water vapor in the reanalysis data product Modern-Era Retrospective Analysis for Research and Application, version 2 (MERRA-2; Gelaro et al., 2017). Tan et al. (2019a) demonstrated the improved suitability of the IMERG v06B final run data product for analysis of the DC of precipitation relative to IMERG v05 and the previous TRMM-derived precipitation data product — the TRMM Multi-Satellite Precipitation Analysis (TMPA) — by calculating a lower median phase lag (0.5 hr) relative to ground-based observations over the southeast United States. While no such assessment of DC phase against ground-based observations has been undertaken in the MC area, reasonable accuracy of DC phase is assumed by extension of the findings over the southeast United States. The accuracy of the amplitude of the DC in IMERG is less certain; Sekaranom et al. (2018) exposed inaccuracies in TRMM estimates of precipitation over high topography of Java, however the repercussions for IMERG and the DC amplitude specifically are

unclear.

To focus on diurnal dynamics in the wet season, a composite DC is calculated using the 1800 days in the DJF season (excluding leap days) between January 2001 and December 2020. Time is stored in Universally Coordinated Time (UTC), and converted to local solar time (LST) as a linear function of longitude after all data extraction and best-fitting has been performed. The study area, spanning 8°N to 10°S and 94°E to 120°E, encapsulates the western side of the MC including the major islands of Sumatra, Borneo and Java, part of the southeast Asian peninsula, and a number of smaller islands (Figure 2.1a). The complementary land–sea mask at IMERG resolution is used to isolate land and marine regions, with marine regions arbitrarily defined as having over 80% water surface coverage.

2.4 Basic Characteristics of the Composite Diurnal Cycle

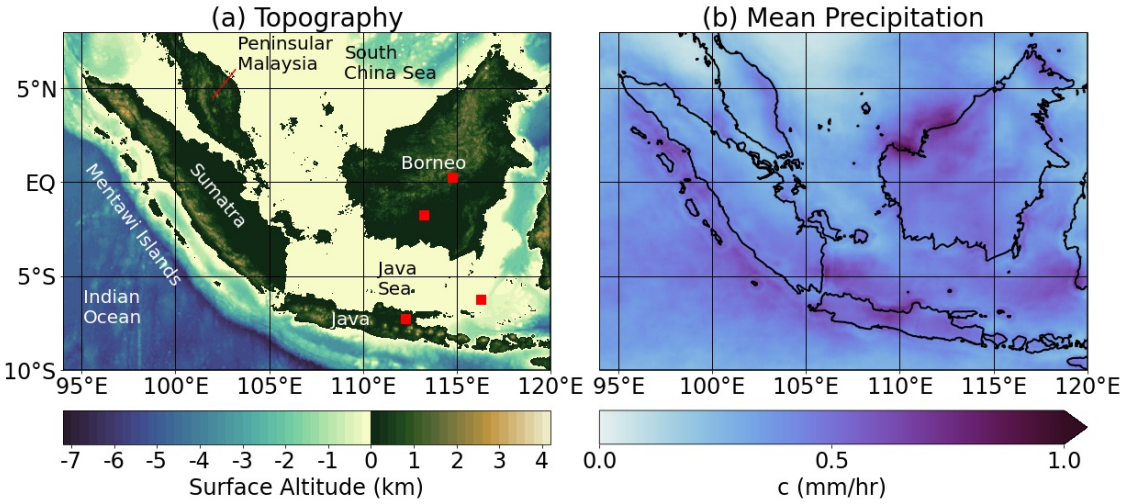

Figure 2.1: (a) Regional map of topography and bathymetry, with major land masses and water bodies labelled. The red squares mark four of the boxes across which the event-based analysis, described in Section 2.7.2, is performed. (b) Climatological distribution of DJF precipitation, based on GPM-IMERG data from 2001–2020.

In this study, the term "basic characteristic" is applied to simple quantities describing the DC that are not associated with a waveform. Mean precipitation (represented as c; Figure 2.1b) is the primary basic characteristic around which diurnal variability occurs. Mean precipitation has a mean value of 0.39 mm hr^{-1} across the entire study area, or 0.42 mm hr^{-1} over land, with the wettest

locations experiencing a mean precipitation rate of around 0.9 mm hr^{-1}. Here, and in many other studies, two further basic characteristics are extracted to inform on the strength and timing of the diurnal precipitation maximum. For later ease of comparison with waveform amplitudes, the "half range" (half of the difference between the diurnal maximum and minimum of precipitation) is reported, along with the "peak time" (the time of day of maximum precipitation at the half-hourly resolution of IMERG).

The half range (Figure 2.2a) is greatest over land, particularly Java and the western sides of the other major land masses, with an overall mean half range over land (0.38 mm hr^{-1}) comparable to the magnitude of mean precipitation (Figure 2.1b), and slightly exceeding 1 mm hr^{-1} in the most highly diurnally active locations. Near-coastal waters also show moderately high diurnal variability, with the half range decaying offshore toward background values of the order of 0.15 mm hr^{-1} over the eastern Indian Ocean and less than 0.10 mm hr^{-1} over the South China Sea, some hundred kilometres from their closest highly diurnally active coastlines. The unusually high marine diurnal variability observed near the northwest coast of Borneo and over the far western Java Sea is associated with very high mean precipitation; there is no process specifically enhancing the diurnal component of precipitation variability in these areas relative to their surroundings, merely stronger diurnal variability in proportion with the higher mean precipitation. The pattern of peak time (Figure 2.2b) shows that diurnal precipitation over near-coastal land peaks in the mid-late afternoon with a distinct inland gradient within about 100-200 km of the coastlines, inferring inland propagation of precipitation through the evening. Inland Borneo and parts of inland Sumatra have a less spatially coherent peak time, and in some regions a sharp discontinuity is observed between locations with a mid-afternoon peak time and locations with a post-midnight peak time. In many near-coastal waters, offshore propagation of peak precipitation is also evident from the progression of peak time from around midnight near the coasts toward late morning further offshore. The less spatially coherent peak time signal over the offshore Indian Ocean and South China Sea is indicative of the dominance of outliers, associated with strong individual non-diurnal precipitation events, over the open ocean DC. This is consistent with previous studies demonstrating the distinct characteristics and influences of the open ocean DC, which is typically found to be weaker than coastal and continental DC regimes (e.g. Nesbitt & Zipser, 2003; Kikuchi & Wang, 2008).

These basic characteristics are consistent with expectations of a DC regime

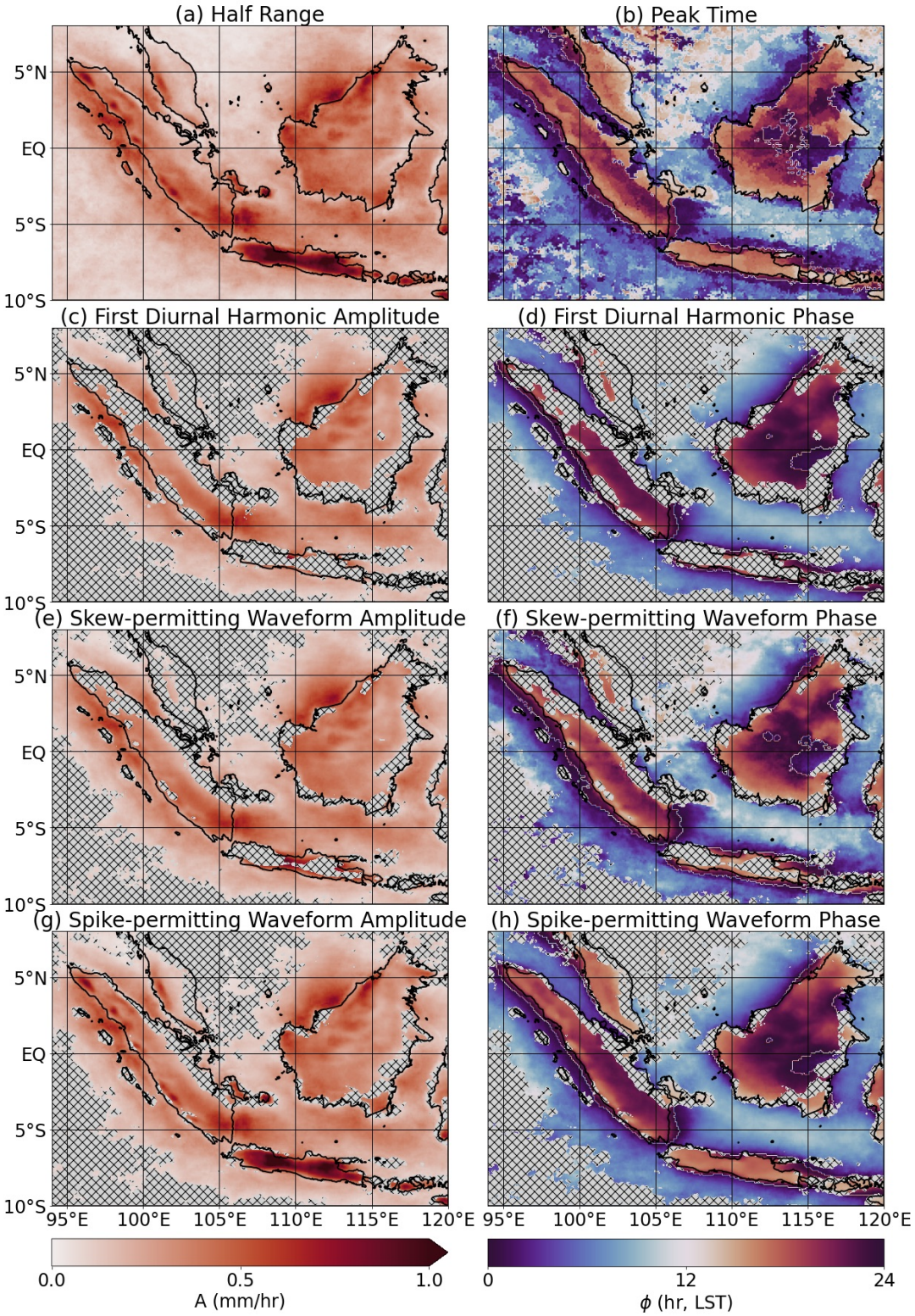

Figure 2.2: Indicators of the magnitude (left panels) and timing (right panels) of diurnal precipitation variability. (a) Half the difference between the maximum and minimum precipitation. (b) Time of maximum precipitation. (c–h) Amplitude and phase of the: (c&d) first diurnal harmonic; (e&f) best-fit skew-permitting waveform, and; (g&h) best-fit spike-permitting waveform. Hatching is applied where $\epsilon > 0.4$ for the relevant waveform (see Equation (2.2) and Figures 2.3a and 2.6a&c).

driven by the land–sea contrast. The discontinuities of peak time in inland areas point to one of the shortcomings of these basic characteristics, which is their inability to characterise more than one major diurnal peak in precipitation if present. Lowland regions to the east of mountain ranges over Sumatra and Borneo are known to experience a mean DC with both an afternoon peak and a night peak (e.g. Bai & Schumacher, 2022), hence a subtle change in the relative strength of these local maxima can affect which one counts as the peak time. This is a dramatic example of the difficulties associated with trying to understand the full 24-hour cycle of precipitation at a location using only basic characteristics, and these difficulties also apply where there is only one major maximum. It is not necessarily accurate to assume that the diurnal minimum occurs 12 hours before/after the maximum, or that the intensification and weakening occur steadily or in an oscillatory manner. By characterising the data with a suitable waveform, the complete 24-hour cycle can be approximately represented which removes the need to make assumptions about the details of the DC away from the maximum. The following section considers the FDH characterisation of the DC and to what extent the FDH is a suitable waveform for the characterisation of observed DC variability.

2.5 Form-fitting with Diurnal Harmonics

2.5.1 Form-fitting with the First Diurnal Harmonic

The FDH is the least-squares best-fit sinusoidal wave with 24-hour period fitted to the observed diurnal variability, where "diurnal variability" is defined as the composite DC minus the mean precipitation (c; Figure 2.1b) at any location. Two parameters describe the FDH; an amplitude (A) and a phase (ϕ). The FDH characterisation of the composite DC (diurnal variability plus the mean) therefore follows the equation:

$$f(t) = A\cos\left(\frac{2\pi}{T}\left[t-\phi\right]\right) + c, \tag{2.1}$$

where f is the rate of precipitation indicated by the waveform at time t in hours, and T is the diurnal period (24 hours).

In meteorological time series, it has typically been found that the amplitude of the FDH dominates over that of higher-order harmonics. For instance Yang

& Slingo (2001) found that the amplitudes of the second and third diurnal harmonics of mean brightness temperature are generally of the order 40% and 15% respectively of the FDH amplitude. When higher-order harmonics are negligible, the FDH amplitude and phase are accurate indicators of the magnitude and timing of the diurnal maximum and the FDH waveform can be used to accurately approximate the full 24-hour DC. In such cases, the FDH amplitude should closely resemble the half range (Figure 2.2a) while the FDH phase should closely resemble the peak time (Figure 2.2b).

To quantify the general accuracy of the FDH waveform approximation (and later waveform approximations), the proportion of diurnal variability accounted for by the waveform is calculated. The standard deviation of the residual, where the residual is defined as the composite DC (d) minus the best-fit waveform (f) evaluated at each of the N (48) half-hourly time steps, quantifies the error in the waveform characterisation. This error is inherently proportional to the magnitude of diurnal variability, therefore a "scaled error" (ϵ; Figure 2.3a) is calculated in order to quantify the appropriateness of the waveform characterisation at each grid point in the IMERG dataset by normalising against the standard deviation of the composite DC:

$$\epsilon = \frac{\sqrt{\frac{1}{N}\sum_{n=1}^{N}(d_n - f_n)^2}}{\sqrt{\frac{1}{N}\sum_{n=1}^{N}(d_n - c)^2}}. \tag{2.2}$$

This scaling enforces a $0 \leq \epsilon \leq 1$ range, where $\epsilon = 0$ indicates perfect waveform fit and $\epsilon = 1$ indicates no waveform component (i.e. $A = 0$). In this study, waveforms are considered to provide a sufficiently accurate characterisation of the DC only where $\epsilon \leq 0.4$; this arbitrary threshold balances the need for an accurate waveform with the reality that the waveforms considered here are highly idealised. In order to minimise the risk of misinterpreting parameters, visualisation and interpretation of waveform parameters are restricted to locations where the waveform provides a sufficiently accurate characterisation.

Over land, scaled error varies from low over central Borneo (Figure 2.3c) to very high over eastern Sumatra (Figure 2.3e). Broad areas of land including Java and much of coastal Sumatra and Borneo have intermediate scaled error, suggesting a characterisation which is fair to first order but with a large residual at certain times of day, which could be due to relatively strong noise or due to a

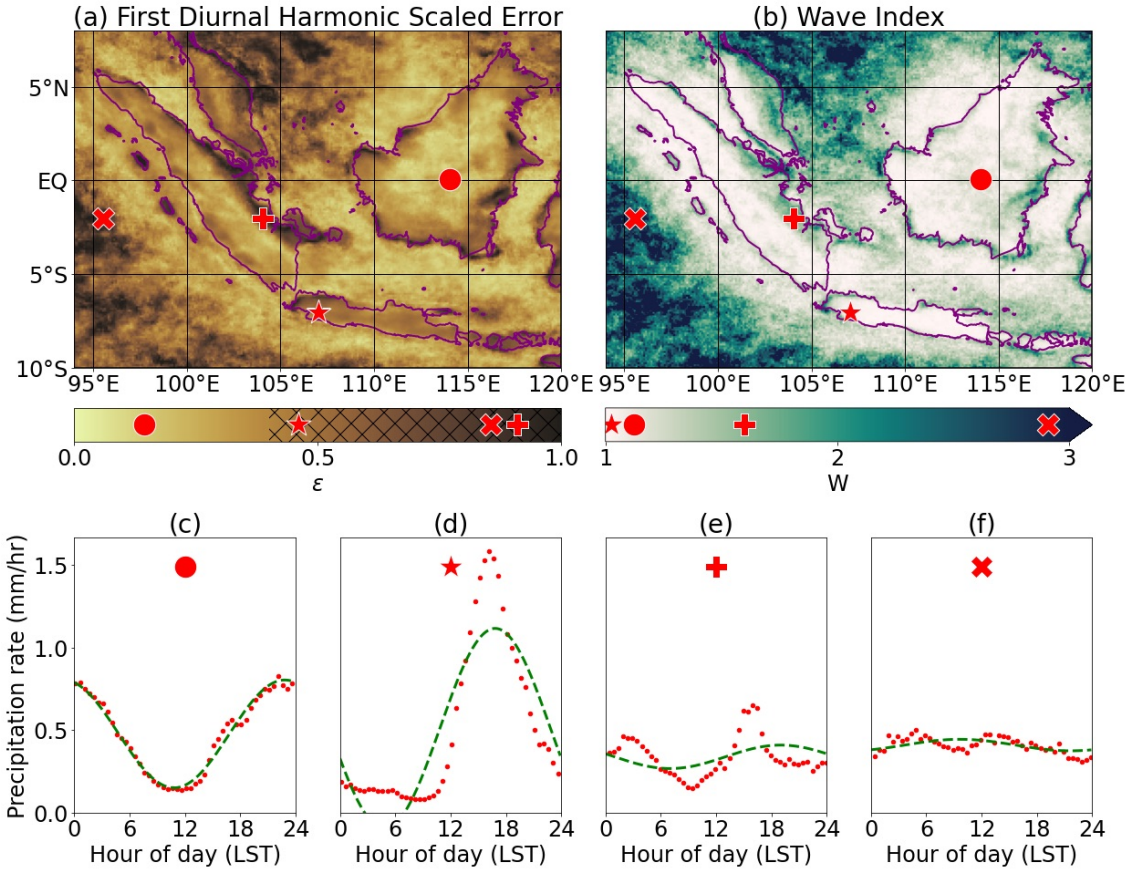

Figure 2.3: Indicators and examples of presence and character of diurnal activity. (a) Scaled error (ϵ) map for the first diurnal harmonic waveform. Colour bar hatching corresponds to the map hatching applied in Figure 2.2c&d. (b) Wave index map, quantifying the complexity of the diurnal cycle as defined in text. (c–f) Examples of the composite diurnal cycle of precipitation at point locations, with the first diurnal harmonic as the dashed green line.

systematic difference between the shape of the DC and the shape of the idealised waveform (e.g. Figure 2.3d). Over water, there is a clear tendency from low scaled error in coastal areas toward high scaled error far offshore as the diurnal signal weakens and noise becomes increasingly dominant (e.g. Figure 2.3f). The half-range-weighted mean scaled error — that is, the mean scaled error with each grid point weighted proportionally to its half range — across the entire study area is 0.37.

The FDH amplitude and phase are visualised in Figure 2.2c&d, with those regions which are not sufficiently accurately characterised by the waveform (i.e. $\epsilon > 0.4$) hatched over. Where not hatched, the FDH amplitude compares strongly to the half range (Figure 2.2a), as anticipated, while the FDH phase resembles a smoothed-out peak time (Figure 2.2b). The spatial smoothness of

the FDH phase emphasises the divide between the diurnal regimes of land and water and is less complicated by outliers than the peak time, however it also affects the representation of propagation speeds. Over Sumatra and Borneo, the FDH phase features a shorter difference in timing between coastal and inland precipitation maxima than the peak time (removal of coastal hatching would further accentuate this), such that inland propagation of precipitation based on the FDH phase appears quicker. A similar comparison is observed over the Java Sea; the near-midnight peak in precipitation around the northern coast of Java slowly propagates northward until midday in the peak time map, while the FDH phase changes less rapidly with distance northward, indicating more rapid northward propagation of the precipitation peak. The FDH phase and peak time are more clearly contrasted in Figure 2.4b, which visualises the lag of the FDH phase relative to the peak time (this lag is described as the "phase error" to reflect waveform misrepresentation of the time of maximum precipitation). Within approximately 100-150 km inland of coastlines, especially southern and western coastlines, the FDH phase error tends to be positive, while further inland areas (particularly across central Borneo) demonstrate a less coherent pattern but with a less positive mean FDH phase error than closer to coastlines. The strong correlation observed between FDH phase error and FDH phase — where FDH phase lag (red in Figure 2.4b) coincides with the earliest FDH phases over both land and sea while FDH phase lead (blue in Figure 2.4b) coincides with the latest FDH phases of both the land and sea regimes — is consistent with the above discussion on the effect of phase parameter on apparent propagation speeds.

The FDH phase errors observed are of the order of multiple hours in many areas, even where the FDH provides a sufficiently accurate characterisation of the DC. The FDH phase is within one hour of the peak time over only 37% of the total study area or 38% of land area, increasing slightly to 45% of the total area where the FDH characterisation is sufficiently accurate according to $\epsilon \leq 0.4$. Over land, FDH phase lag exceeding one hour is over three times more prevalent than FDH phase lead exceeding one hour; this systematic deviation in land-based precipitation phase risks offsetting the perceived timescale over which deep diurnal convection develops over land. Bai & Schumacher (2022) performed a similar analysis demonstrating large and spatially variable differences between FDH phase and peak time.

As quantified by the analogous amplitude error (Figure 2.4a), the FDH amplitude tends to under-represent the magnitude of diurnal activity across the

study area, particularly over certain land areas such as Java, parts of near-coastal Sumatra and Borneo, and many of the smaller islands. Over Java, the mean amplitude error is -0.15 mm hr^{-1} while the mean half range is 0.66 mm hr^{-1}, meaning that the FDH amplitude captures only 77% of the magnitude of diurnal variability in this key region (defining the capture proportion as 1 + Mean Amplitude Error/Mean Half Range). Regions with high amplitude error correlate strongly with regions of high scaled error (Figure 2.3a), particularly over land; since the correlation between the magnitude of the phase error and the scaled error is less strong, it is suggested that an accurate amplitude parameter is intrinsically more critical for accurate waveform characterisation than an accurate phase parameter.

As used here, the FDH does not offer accurate insight into diurnal processes across most coastal land areas, far offshore nor over almost all of Java and peninsular Malaysia (Figure 2.2c&d). Far offshore, the half range is small, so it is expected that any true diurnal signal has a magnitude indiscernible against the background noise — this may be addressed by spatial averaging of the DC, however spatial fidelity is prioritised in the visualisations of this study. Conversely, the half range over Java (and, to a lesser extent, other coastal regions) is large, indicative of a strong diurnal signal which is worth characterising more accurately than the FDH can achieve.

2.5.2 Consideration of Diurnal Cycles with Multiple Maxima

In order to characterise the DC variability in locations that the FDH fails to sufficiently accurately characterise, a more complex waveform with more than two degrees of freedom is needed. One might consider adding to the FDH the second diurnal harmonic, a sinusoidal wave with 12-hour period, which would introduce two additional best-fit parameters: the amplitude and the phase of the second diurnal harmonic. This approach reduces the half-range-weighted mean scaled error of the study area by over 40%, from 0.37 to 0.22. Of course, yet higher-order diurnal harmonics may also be added to ultimately completely characterise the DC. While incorporation of the second diurnal harmonic is moderately effective at improving the accuracy of the waveform characterisation, it is difficult to make use of the characterisation intuitively because the shape of the combined waveform may be complex and the additive nature of harmonics makes it difficult to interpret any single parameter in isolation.

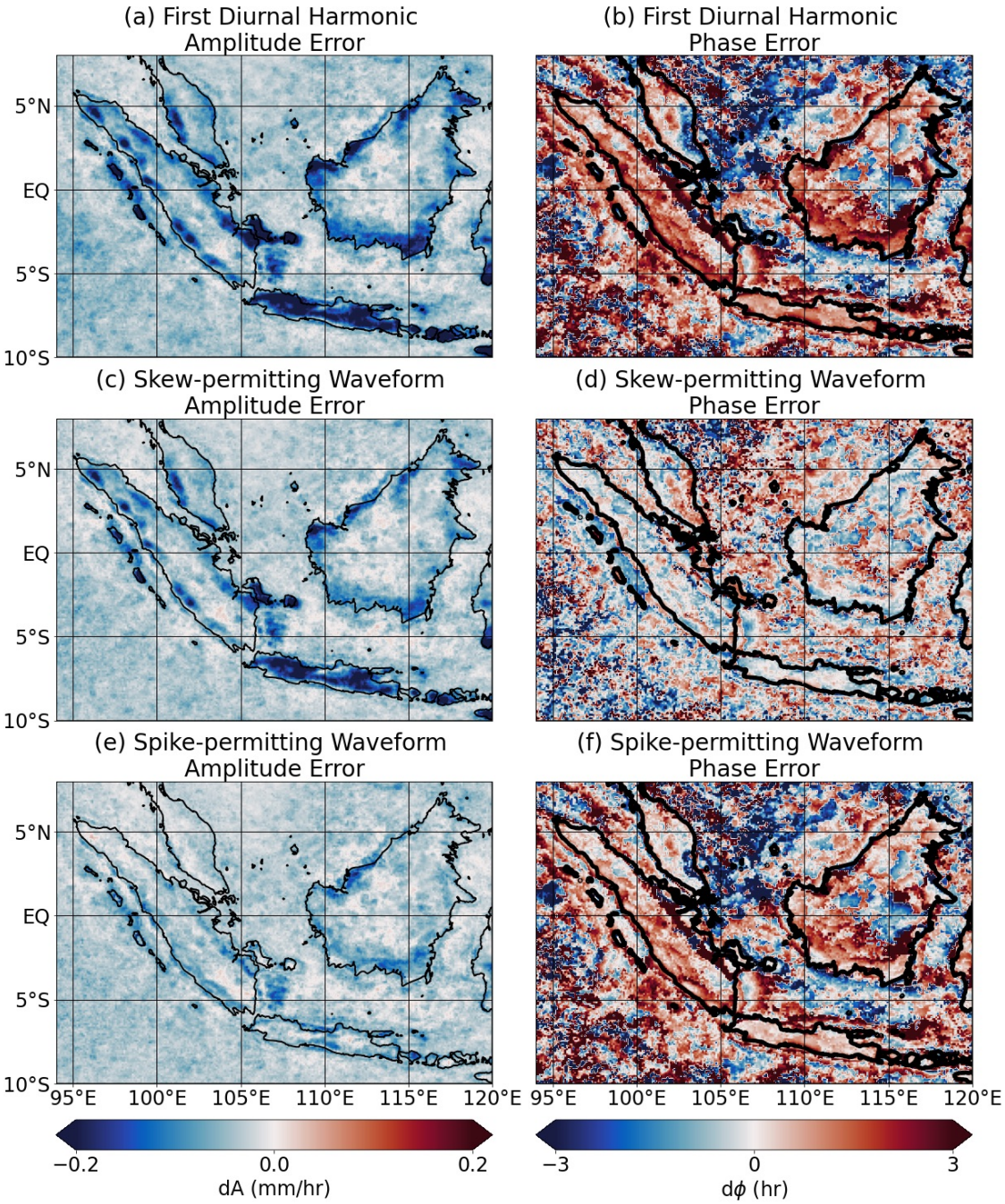

Figure 2.4: Amplitude error (left panels) and phase error (right panels) for: (a&b) the first diurnal harmonic; (c&d) the best-fit skew-permitting waveform, and; (e&f) the best-fit spike-permitting waveform. Errors defined as the waveform parameter (amplitude/phase) minus the comparative basic characteristic (half range/peak time).

The intuitively ideal waveform would retain just one amplitude parameter and phase parameter, to facilitate direct comparisons with the half range and peak time, and incorporate one additional degree of freedom that can capture as much additional diurnal variability as possible by morphing the shape of the waveform in an intuitive manner. A waveform with a single amplitude-phase

parameter pair (a "single-peak waveform") is, however, inherently only suited to characterisation of DCs with one dominant maximum-minimum pair. This excludes parts of eastern Sumatra and Borneo that are known to experience dual diurnal precipitation maxima. However, the regions with the highest magnitude of diurnal variability are generally found to have one dominant maximum, therefore a single-peak waveform may have high characterisation potential in key areas. To demonstrate the spatial distribution of the degree of dominance of the primary maximum-minimum pair, this study utilises a simple metric referred to as the "wave index" (W; Figure 2.3b) which quantifies the relative size of perturbations attributed to additional maxima and minima in the DC. The wave index is defined as the ratio between the sum of the absolute differences between each pair of consecutive time steps (or, equivalently, each neighbouring maximum-minimum pair) and two times the DC range (or four times the half range):

$$W = \frac{\sum_{n=1}^{N} |d_{n+1} - d_n|}{2\,(d_{max} - d_{min})}. \tag{2.3}$$

W takes a minimum value of 1 when there is only one local maximum and minimum in the composite DC, and a higher value when additional maxima and minima are present. The wave index shows that most land features one dominant diurnal maximum-minimum pair, with the main exceptions being the eastern parts of Sumatra, Borneo and peninsular Malaysia, as anticipated. Near-coastal marine locations typically show a reasonably low wave index, tending toward higher wave index further offshore. Unlike over eastern land areas, the multi-peak behaviour offshore is mostly attributed to noise; this can be demonstrated by calculating the wave index after spatially averaging the DC which reduces the offshore wave index as the noise is damped, while the wave index over eastern land areas is not as strongly affected (not shown). Locations with the highest half range feature one dominant maximum-minimum pair, and those locations with a high wave index tend to have a low half range. Across the study area, 95% of grid points with half range over 0.2 mm hr^{-1}, and over 99% of grid points with half range over 0.3 mm hr^{-1}, have $W \leq 1.5$.

The half-range-weighted mean wave index across the entire study area is 1.30. This value shows that the combined magnitude of additional diurnal fluctuations is, on average, about 30% of the magnitude of the dominant diurnal oscillation. Despite being limited to characterisation of the dominant diurnal oscillation, it seems likely that a single-peak waveform may be able to

characterise the key features of the DC well. The half-range-weighted mean scaled error across the study area that would be achieved by the optimal single-peak waveform (i.e. a waveform that characterises the dominant diurnal oscillation with absolute accuracy) can be estimated by considering an idealised cycle of diurnal variability with $W = 1.30$; two sinusoidal oscillations each with 12-hour period, where one oscillation has an amplitude 30% as great as the other. The scaled error of this idealised DC can be calculated and is approximately 0.29. While this is a crude estimate (and likely an overestimate due to the influence of noise on the wave index), it is comfortably lower than the half-range-weighted mean scaled error calculated above for the FDH (0.37), which suggests that there is significant potential to improve on the characterisation of the DC provided by the FDH without needing to consider the complication of characterising multiple diurnal maximum-minimum pairs with multiple pairs of amplitude and phase parameters. The challenge is to achieve this while retaining the independent intuitive value of each variable parameter, meaning the degrees of freedom added to the FDH should be minimised. The following section demonstrates DC characterisation using two single-peak waveforms that generalise the oscillatory nature of the FDH with one extra degree of freedom each, and explores the impact of each waveform on amplitude and phase representation and diurnal variability characterisation.

2.6 Form-fitting with other Single-peak Waveforms

In this section, two novel single-peak waveforms — a skew-permitting waveform and a spike-permitting waveform — are discussed, with description of the waveform properties, derivation and the best-fit characterisation procedure followed by a description of the resultant best-fit parameters and their comparisons with the FDH parameters. A reference to simplified versions of the programming code used to calculate these best-fit waveforms (in Python programming language) is supplied at the end of Section 2.8.

2.6.1 Form-fitting with a Skew-permitting Waveform

2.6.1.1 Form-fitting procedure

The skew-permitting waveform is designed to accommodate cases where the DC maximum and minimum are not half a cycle apart, such that the increase in

diurnal precipitation occurs rapidly and the decrease is drawn out across more of the day, or vice versa. The skew-permitting waveform has the form:

$$f(t) = \frac{A}{\tan^{-1}\left(\frac{\alpha_0}{\sqrt{1-\alpha_0^2}}\right)} \tan^{-1}\left\{\frac{\alpha_0 \sin\left[\frac{2\pi}{T}(t-\phi)+\cos^{-1}(\alpha_0)\right]}{1-\alpha_0\cos\left[\frac{2\pi}{T}(t-\phi)+\cos^{-1}(\alpha_0)\right]}\right\} + c, \quad (2.4)$$

where α_0 is the skew parameter and can vary between -1 and 1 (except for 0 as discussed below). For all values of α_0, as for the FDH, A represents half the difference between the waveform maximum and minimum and ϕ represents the time of the waveform maximum; these are treated as the fixed definitions of waveform amplitude and phase in this study. A linearisation calculation (explained in the following paragraph) is applied to convert from the raw skew parameter (α_0) to a rescaled skew parameter, $-1 \leq \alpha \leq 1$, which is equivalent to α_0 for the values of -1, 0 and 1. This cumbersome equation and process result in a rather intuitive waveform (Figure 2.5a). The waveform shape converges on the shape of the FDH at low $|\alpha|$, hence the simplification to Equation (2.1) is made when $\alpha = 0$ to render it a solvable value in the best-fitting procedure. Equation (2.4) varies smoothly toward a saw-tooth function as $|\alpha|$ increases. Positive α corresponds to a quicker increase in precipitation, such that the extreme positive case of $\alpha = 1$ features an instantaneous transition from minimum to maximum precipitation followed by constant decrease throughout the cycle. Conversely, extreme negative α gives a constant increase throughout the day followed by an instantaneous drop from the maximum to the minimum. Note that the concept of skew described here is unrelated to the statistical definition of the skew of a distribution, although the direction of the tail away from the maximum does qualitatively mirror the statistical definition.

The skew parameter is linearised with respect to the mean time lag of precipitation following the waveform minimum. This is achieved by calculating the timing of the "waveform centroid" between two consecutive waveform minima — the centre of the area bound between the waveform and the straight line connecting the consecutive waveform minima ($y = -1$ in Figure 2.5a) — for any given value of α_0. When $\alpha_0 = 0$, the time lag of the waveform centroid after the minimum (t_{lag}) is exactly 12 hours, while t_{lag} may be as low as 8 hours for positive skew or as high as 16 hours for negative skew. By defining $\alpha = -(t_{lag} - 12)/4$, where t_{lag} is a function of α_0, the magnitude of the rescaled skew parameter becomes a good indicator of how significantly the shape of the DC deviates from that of the FDH.

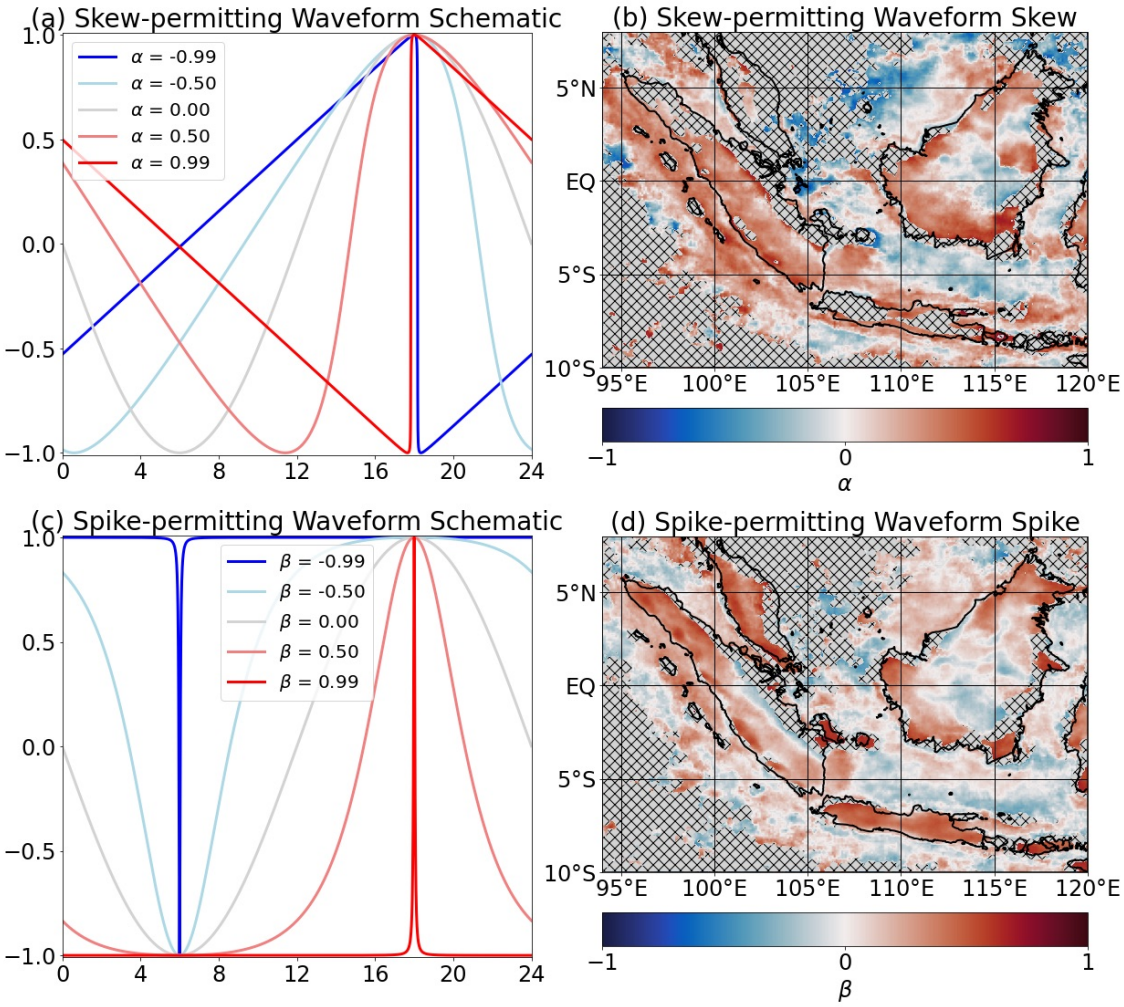

Figure 2.5: Skew and spike behaviour of the diurnal cycle (see Equations (2.4)&(2.5)). (a) Skew-permitting waveform structure according to variable rescaled skew parameter, α. $A = 1$, $\phi = 18$ and $c = 0$ for all lines. (b) Map of best-fit skew parameter, partnering the best-fit skew-permitting waveform parameters in Figure 2.2e&f. (c) Spike-permitting waveform structure according to variable rescaled spike parameter, β. $A = 1$, $\phi = 18$ and $Ag + c = 0$ for all lines. (d) Map of best-fit spike parameter, partnering the best-fit spike-permitting waveform parameters in Figure 2.2g&h. Hatching is applied where $\epsilon > 0.4$ for the relevant waveform (see Figure 2.6a&c).

Equation (2.4) is adapted from a "tilted sine" formula described at the following web address (https://math.stackexchange.com/questions/2430564/equation-of-a-tilted-sine), and is one of a range of formulae able to induce this skew effect. This particular formula was the most simple formula encountered with the ability to induce skew to the extremity of the saw-tooth shape, with the maximum potentially immediately before or after the minimum. While waveforms of this type appear throughout scientific and engineering literature (e.g. Tappeiner et al., 2009; Bray & Dunne, 2017), this study marks the first known application of such a waveform to the characterisation of a cycle observed within a science

discipline, certainly for the meteorological diurnal cycle.

Unlike the FDH, the best-fit skew-permitting waveform cannot be extracted using a Fourier technique, therefore least-squares optimisation is applied. The mean (c) is subtracted to leave the diurnal variability, and the FDH amplitude and phase and $\alpha_0 \approx 0$ are applied as the initial guess. In almost all cases for the DCs in this study, the optimisation successfully converged on a best-fit solution, with only a handful of noisy offshore locations failing to converge (in which case the FDH was taken as the best fit).

2.6.1.2 Results

The amplitude and phase of the best-fit skew-permitting waveform are shown in Figure 2.2e&f, while the associated rescaled skew parameter is shown in Figure 2.5b. As for the FDH, the scaled error was calculated for the best-fit skew-permitting waveform (Figure 2.6a), and only sufficiently accurately characterised locations with $\epsilon \leq 0.4$ are shown. The amplitude parameter is very similar to the FDH amplitude (Figure 2.2c), with a subtle increase in mean amplitude of 0.010 mm hr^{-1} relative to the FDH (approximately 5% increase) with the increase distributed reasonably evenly across the study area. The phase parameter distribution bears a closer resemblance to the peak time than the FDH phase parameter distribution does, with the breadth of timings across Borneo and the Java Sea well represented, though the waveform best-fitting still has a subtle smoothing effect. Systematic regional phase errors are not as evident as they are for the FDH phase (Figure 2.4b&d). Phase is within one hour of the peak time over 59% of the entire study area, or 62% of the region sufficiently accurately characterised by the best-fit skew-permitting waveform. While these are much greater proportions than for the FDH (37% and 45%, respectively), the best-fit skew-permitting waveform phase parameter does not precisely match the peak time in all cases. This suggests that this waveform is not over-fitting to the noise-associated outliers that influence the peak time measurement of the precipitation maximum, therefore the best-fit skew-permitting waveform phase parameter may offer a more robust quantification of the timing of maximum diurnal precipitation.

The rescaled skew parameter distribution (Figure 2.5b) shows that moderately positive skew values prevail over western Sumatra and near-coastal Borneo, with some negative values over eastern central Borneo. Over marine areas, positive skew also prevails within some hundred kilometres of coastlines

(most strongly to the southwest of Sumatra and north of Java) and there is a tendency toward negative skew further offshore. Separately for both the land-based and marine diurnal regimes, skew tends to decrease as the peak time becomes later. Dynamical inferences from the best-fit skew-permitting waveform parameter distributions are discussed in Section 2.7.2.

The half-range-weighted mean scaled error for the best-fit skew-permitting waveform is 0.30, which is an improvement of 0.07 on the FDH and much closer to the estimated optimal single-peak waveform characterisation (0.29). The spatial distribution of characterisation improvement (Figure 2.6b) shows that the key regions that benefit from a skew-permitting characterisation are parts of near-coastal Borneo and Sumatra and the seas around the Mentawi islands to the west of Sumatra (all of which have strongly positive skew). Some regions however, notably including most of Java, do not benefit substantially from a skew-permitting characterisation and remain insufficiently accurately characterised, meaning that the best-fit parameters over such regions are still liable to be misleading.

2.6.2 Form-fitting with a Spike-permitting Waveform

2.6.2.1 Form-fitting procedure

The spike-permitting waveform accommodates cases where the mean precipitation rate is not the average value of the DC maximum and minimum, such as the example location illustrated in Figure 2.3d. With this waveform, composite precipitation may be relatively constant for a long stretch of the DC, with a short duration where precipitation significantly increases or decreases (Figure 2.5c). The following equation is the basis for the spike-permitting waveform:

$$f(t) = A\cos\left(\frac{\pi\tan^{-1}\left\{\left[\frac{2\bmod_T(t-\phi-T/2)}{T}-1\right]\tan(\beta_0)\right\}}{\beta_0}\right) + A\,g(\beta_0) + c, \quad (2.5)$$

where β_0 is the spike parameter and varies between 0 and $\pi/2$, $\bmod_T$ is the remainder operator with base T, and $g(\beta_0)$ is a translation function, varying between 0 (when $\beta_0 = 0$) and 1 (when $\beta_0 = \pi/2$). When integrated across the cycle, the first term on the right side of the equation does not have a mean value of zero, so the second term translates the waveform to restore a time-integrated

mean value of zero before the third term (c) is added. This ensures that the parameter c consistently represents the mean value. As with the FDH and the skew-permitting waveform, A denotes half the difference between the waveform maximum and minimum while ϕ corresponds to the time of the waveform maximum.

Equation (2.5) is undefined when the new parameter $\beta_0 = 0$. However, the function is designed to converge on the FDH as β_0 tends toward 0. As β_0 becomes more positive, the waveform peak becomes increasingly narrow, until at $\beta_0 = \pi/2$ the DC features a constant value except for an instantaneous intense peak (akin to a Dirac delta function). In order to achieve the opposite effect where the minimum becomes increasingly narrow, the waveform is inverted (i.e. A is replaced with $-A$ and ϕ with $\phi + T/2$) — the best-fitting procedure also considers this behaviour, and in cases where the optimisation procedure returns an inverted spike-permitting waveform, the true-to-definition values of A and ϕ are reported, and β_0 is reported as negative. This means that, as reported, β_0 may range between -$\pi/2$ and $\pi/2$, and $g(\beta_0)$ may range between -1 and 1.

In order to make the spike parameter a good indicator of how significantly the waveform shape deviates from that of the FDH, a rescaled spike parameter, β, is calculated by linearising with respect to the relative closeness of the waveform mean to the waveform maximum and minimum, and normalising onto a scale from -1 to 1. Values of -1, 0 and 1 for β correspond to values of -$\pi/2$, 0 and $\pi/2$ for β_0, respectively. In practice, the definition of the rescaled spike parameter makes it equivalent to the translation function (i.e. $\beta = g(\beta_0)$). Due to the complexity of the function $g(\beta_0)$, it is approximated as a nineteenth order polynomial. While the effect of linearisation is rather subtle for the skew-permitting waveform, it has a pronounced effect for the spike-permitting waveform. Values of β_0 that appear moderate in magnitude show only a subtle qualitative deviation from the form of the FDH (i.e. low $|\beta|$), as the qualitative variability of the spike-permitting waveform is concentrated around extreme $|\beta_0|$. For this reason, the optimisation process is most reliable when the initial guess of β_0 is not too close to zero to avoid the risk of the algorithm finding that the waveform fit is unaffected by small changes to the spike parameter — an initial guess of 10^{-4} was found to be suitable.

Equation (2.5) is analogous to other waveforms with an accentuated peak, such as the cnoidal waveform and, incidentally, the derivative of waveforms like the skew-permitting waveform, but was derived independently as part of this

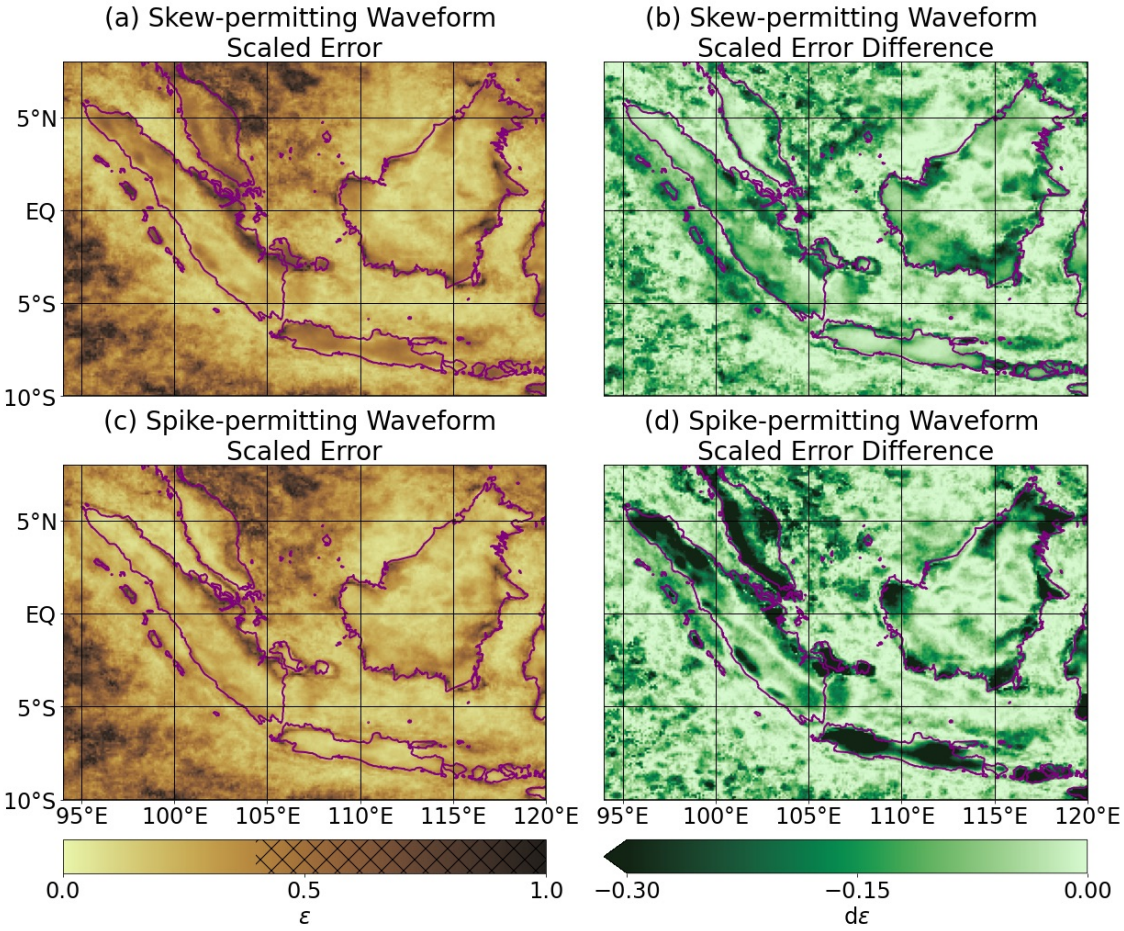

Figure 2.6: Maps of new waveform scaled error (left panels), and improvements relative to the first diurnal harmonic (right panels). Based on (a&b) the best-fit skew-permitting waveform and (c&d) the best-fit spike-permitting waveform. Colour bar hatching corresponds to the map hatching applied to the appropriate waveform in Figures 2.2e–h and 2.5b&d.

study. One worthy alternative formula inducing similar behaviour is:

$$f(t) = A\left(\frac{\cos\left\{\frac{2\pi}{T}\left[t-\phi\right]\right\}+1}{2}\right)^{\beta_0} + A\,g(\beta_0) + c, \tag{2.6}$$

for $\beta_0 \geq 1$. This formula, discovered at a late stage in the study, may have been preferable to Equation (2.5) for its greater simplicity in retrospect, however the formulae are likely to be equally functionally appropriate. While the analogous cnoidal waveform is known to have been used in distant scientific disciplines for the characterisation of non-linear waves (e.g. Liu et al., 2018), no such waveform is believed to have been used previously to characterise a meteorological cycle.

2.6.2.2 Results

The amplitude and phase of the best-fit spike-permitting waveform are shown in Figure 2.2g&h, while the associated rescaled spike parameter is shown in Figure 2.5d. As for the other waveforms, the scaled error was calculated for the best-fit spike-permitting waveform (Figure 2.6c), and the best-fit parameters are only shown in regions with $\epsilon \leq 0.4$. Of the three waveforms discussed in this study, the amplitude of the best-fit spike-permitting waveform offers the closest match to the half range. The domain-averaged amplitude is larger than that of either the FDH or best-fit skew-permitting waveform (a 0.016 mm hr^{-1} or 8% increase on the FDH). Regions with the largest FDH amplitude error (Figure 2.4a) are responsible for a high proportion of this increase, such that these regions do not stand out as having a highly under-representative best-fit spike-permitting waveform amplitude (Figure 2.4e). For instance, while the FDH only captured 77% of the magnitude of diurnal variability over Java, the best-fit spike-permitting waveform captures 92%, meaning that the mean amplitude over Java is nearly 20% greater using the spike-permitting waveform relative to the FDH. Compared with the FDH, there are 80% fewer grid points where the amplitude error is more negative than -0.1 mm hr^{-1}, resulting in a more uniform background amplitude error which accounts for 14% of diurnal variability as quantified by the half range.

The best-fit spike-permitting waveform phase parameter (Figure 2.2h) is qualitatively similar to the FDH phase (Figure 2.2d). As such, use of the spike-permitting waveform results in a systematic phase lag over near-coastal land, much like the FDH (Figure 2.4b&f), though the magnitude of the lag is lower. 51% of the well-characterised area has a phase value within one hour of the peak time, compared with 45% and 62% for the FDH and best-fit skew-permitting waveform, respectively. Across both land and water, the best-fit spike-permitting waveform phase is more uniform than either the best-fit skew-permitting waveform or the peak time distribution (Figure 2.2b&f), therefore the apparent propagation speed of maximum precipitation away from coastlines is too fast, as discussed for the FDH.

The spike parameter distribution (Figure 2.5d) shows a prevalence of positive spike behaviour over most land areas, particularly over Java, western and central Sumatra, western peninsular Malaysia, coastal Borneo and some of the minor islands. The most positive values align with those areas that have the highest FDH amplitude error (Figure 2.4a). Eastern inland Sumatra and most of inland

Borneo show slightly negative spike. The distribution of spike over marine areas is less simple, generally ranging between weakly positive and weakly negative, with negative spike often located close to land areas with the most positive spike. Positive spike dominates along the southwest coast of Sumatra, while negative spike is prevalent in the seas around Java.

As a result of significant characterisation improvements over positive spike land areas such as Java (Figure 2.6d), the half-range-weighted mean scaled error for the best-fit spike-permitting waveform is 0.27, compared with 0.37 and 0.30 for the FDH and best-fit skew-permitting waveform, respectively. This surpasses the crudely estimated value of 0.29 for the optimal single-peak waveform, and begins to approach the half-range-weighted mean scaled error for the second diurnal harmonic (0.22), despite incorporating one less degree of freedom. 91% of locations with half range over 0.2 mm hr^{-1} meet the $\epsilon \leq 0.4$ criterion (Figure 2.6c) and are therefore sufficiently accurately characterised by this new waveform, compared with 72% for the FDH.

2.7 Discussion and Applications

2.7.1 Waveform Strengths and Deficiencies in Representation of the Diurnal Cycle

Best-fit waveforms have two key benefits; they are not highly sensitive to noise or outliers in the way that the basic characteristics of half range and peak time may be, and they offer a means to approximate the continuous 24-hour cycle. However, if the waveform cannot achieve a shape that closely follows the DC, the output parameters cannot be accurately interpreted in their usual manner (i.e. amplitude as an indicator of DC magnitude and phase as an indicator of the time of the maximum). As these results show, different waveforms have different susceptibilities regarding the intuitive reliability of their parameters.

The FDH is susceptible to misrepresenting both the DC magnitude and the time of maximum, particularly over land (Figure 2.4a&b). The shape of the FDH cannot capture the brief intense peak in precipitation observed in areas like Java, nor can it capture the asymmetry of the rapid intensification and gradual weakening of precipitation over near-coastal areas (Bai & Schumacher, 2022). The suitability of the FDH characterisation is highly regionally variable; it characterises the DC very well over most of inland Borneo and many

near-coastal marine areas, and is entirely unsuitable over eastern land areas.

The best-fit skew-permitting waveform is also susceptible to misrepresenting the DC magnitude (Figure 2.4c), since the added degree of freedom does not allow for a much briefer peak. The phase parameter, however, is a reliable indicator of the time of day at which the most intense precipitation is focused, as shown by its regional accuracy in comparison with the peak time (Figure 2.4d). Over land, the mean phase error is very small (-0.07 hours), indicating an accurate representation of the large-scale peak time to within five minutes, while the other two waveforms have a mean and median phase lag over land of more than 30 minutes (and greater if considering only near-coastal land). The 0.5 h mean phase lag of the DC peak time in IMERG behind that in ground-based observations in the southeast United States demonstrated by (Tan et al., 2019a), if also applicable to the MC, means that the inaccuracy of the representation of the DC timing in IMERG is a greater limitation to accurate DC phase characterisation than any systematic misrepresentation of the peak time by the best-fit skew-permitting waveform. However, the systematic misrepresentation of the peak time by the FDH and best-fit spike-permitting waveform exacerbates the mean phase lag of IMERG, such that the mean phase lag of either the FDH or best-fit spike-permitting waveform phase behind the peak time in ground-based observations may exceed 1.0 h. The standard deviation of best-fit skew-permitting waveform phase error is lower than for the other waveforms (1.66 hours over the entire study area, in comparison with 1.91 and 1.98 hours for the FDH and best-fit spike-permitting waveform, respectively). The lower standard deviation is consistent with the best-fit skew-permitting waveform phase's closer comparison to the peak time, however it is still imprecise enough to suggest that the waveform does not over-fit to noise-related outliers.

The best-fit spike-permitting waveform produces a more accurate phase parameter than the FDH, however it still features a clear and significant phase lag over near-coastal land and waters, with a tendency toward phase lead or less phase lag both inland and offshore away from coastlines (Figure 2.4f). However, the waveform shape allows for accurate characterisation of the brief but extreme peak in precipitation over land areas including Java (Rais & Yunita, 2017), which means that the best-fit spike-permitting waveform amplitude is a much more reliable indicator of the magnitude of diurnal variability than the other waveform magnitudes (Figure 2.4e). The lack of extreme values and the spatial coherence of the spike parameter (Figure 2.5d) demonstrate the lack of susceptibility of this waveform to outliers when the

cycle is well resolved, however, when applied to cycles with less data points, greater waveform sensitivity to outliers is probable. The reliability of amplitude representation leads to sufficiently accurate DC characterisation ($\epsilon \leq 0.4$) in the vast majority of cases with a single dominant peak (Figure 2.7). The best-fit spike-permitting waveform sufficiently accurately characterises 93.0% of observed DCs with $W < 1.5$ (Figure 2.7d), in comparison with 74.4% and 86.7% sufficiently accurate characterisation of low wave index areas by the FDH and best-fit skew-permitting waveform, respectively (Figure 2.7b&c). For the best-fit spike-permitting waveform, the insufficiently-characterised low wave index locations (magenta) are mostly well-dispersed across the region, which suggests that many of the 7.0% of insufficiently characterised low wave index locations are fringe or borderline cases. Exceptions are northwest Borneo (around 2.5°N, 111.5°E) where an otherwise roughly steady cycle features a brief negative diurnal perturbation for a few hours before local midday followed by a slightly less brief positive diurnal perturbation after midday (resulting in the negative perturbation not being characterised), and parts of southeast Borneo which demonstrate strongly positive skew.

Both the FDH and best-fit skew-permitting waveform show several coherent areas over land where the wave index is low and characterisation is considered insufficiently accurate (magenta in Figure 2.7), suggesting that these are not borderline failures sensitive to the choice of sufficient ϵ. Instead, these characterisation failures show that there is considerable systematic inability of these waveforms to appropriately characterise certain observed forms of single-peak DC, such as the brief precipitation maximum over west Java (Figure 2.3d). Of the three waveforms, the spike-permitting waveform is demonstrably the most successful waveform at characterising diurnal variability in the presence of a single dominant maximum-minimum pair ($W < 1.5$) — such locations account for 62.0% of the western MC region (Figure 2.7a), including 83% of its land area. Its form-fitting potential is especially strong at very low wave index; of the 22% of the study area with $W < 1.1$, no location has $\epsilon > 0.53$ for the best-fit spike-permitting waveform, while both other waveforms have instances of such locations with $\epsilon > 0.65$. The spike-permitting waveform also demonstrates slightly superior characterisation success at moderate wave index values (lavender in Figure 2.7). However none of the three waveforms considered are able to accurately characterise DCs with complex multi-peak variability (grey in Figure 2.7). This confirms the expected unifying weakness of these single-peak waveforms and shows that a multi-peak waveform will be

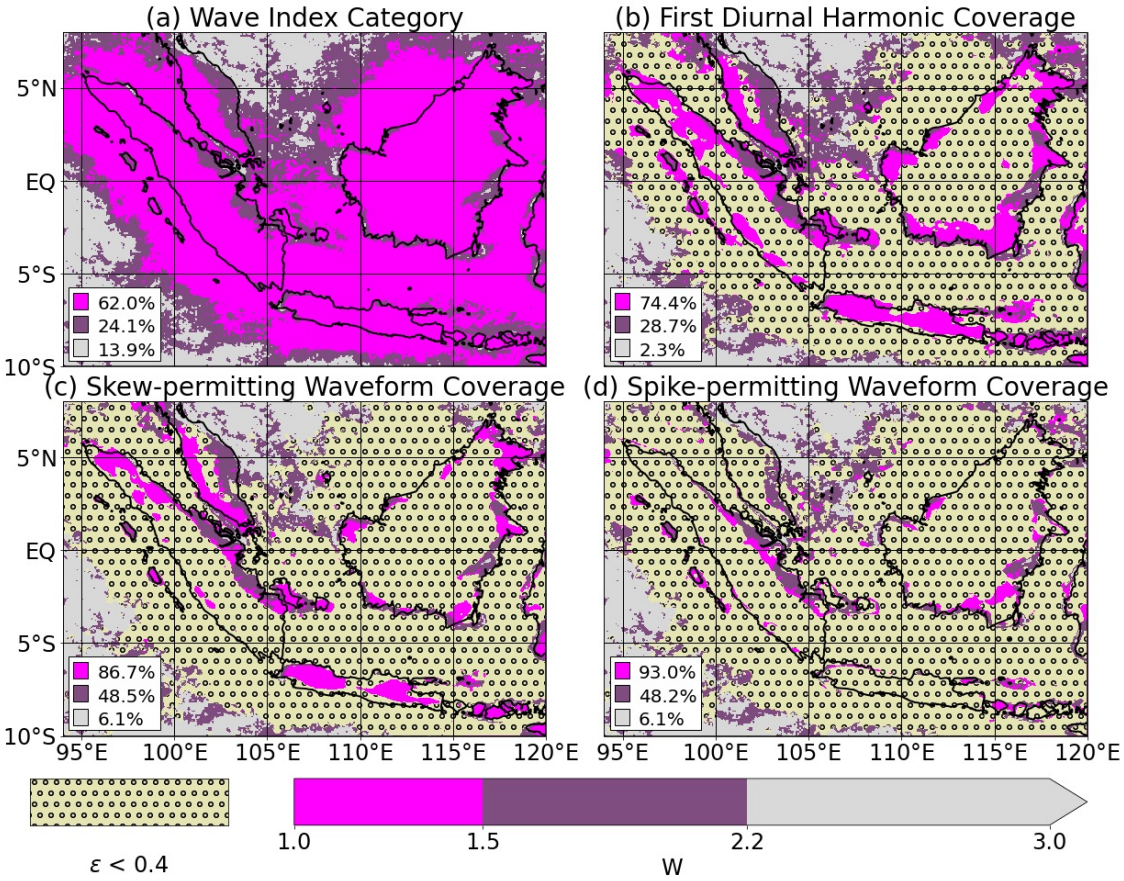

Figure 2.7: Demonstration of the relative skill of the three waveforms in characterising the composite diurnal cycle of precipitation where it is dominated by a single peak. (a) Simplified wave index from Figure 2.3b, where all magenta ($1.0 \leq W \leq 1.5$) and some lavender ($1.5 < W \leq 2.2$) regions might be expected to be well-characterised with a single-peak waveform. The legend percentages show the proportion of grid points within the study area in each wave index category. The same map features yellow circular hatching overlaid where $\epsilon \leq 0.4$ for: (b) the first diurnal harmonic; (c) the best-fit skew-permitting waveform, and; (d) the best-fit spike-permitting waveform. The legend percentages express the proportion of locations for which $\epsilon \leq 0.4$ for the relevant waveform for each wave index category.

necessary in order to achieve accurate 24-hour characterisation of regions with a complex DC.

The skew parameter and, to a lesser extent, the spike parameter demonstrate a tendency toward incoherence when fitting to noise-dominated cycles. The least-squares optimisation procedure for the skew-permitting waveform often returns an extreme skew waveform (a linear best-fit waveform with a step-change between two of the most different consecutive points in the cycle), while the optimisation procedure for the spike-permitting waveform may return a moderate spike waveform that traces the dominant noise-induced fluctuation and fails to characterise diurnal variability across the remainder of the cycle.

The features of the cycle that influence these optimal fits are highly sensitive to small shifts in the noise distribution; it is especially common to observe contrasts between extreme positive and extreme negative skew in adjacent grid cells, described as incoherence. However, these areas of incoherence are masked in Figure 2.5b&d by the hatching, demonstrating that this behaviour is limited to noise-dominated cycles and that both waveforms are reasonably insensitive to low-to-moderate noise.

The FDH has the benefit of being a guaranteed least-squares best fit as extracted by Fourier analysis, while the skew-permitting and spike-permitting waveforms both require an appropriate initial guess and optimisation methodology in order to converge on the best fit. The very low rates of convergence failure (only over weakly-varying regions dominated by noise) and the high spatial coherence of the best-fit skew and spike parameters give confidence in the general success of the best-fit optimisation methodology. The skew and spike parameters both offer clear qualitative insight into the temporal details of the observed diurnal variability of precipitation, which may in turn be used to understand the regional dynamics. Common diurnal mechanisms may occur in different areas with comparable skew and/or spike. The following subsection considers the features and consistency of individual precipitation events to investigate possible physical mechanisms that lead to positive and negative values of skew and spike.

2.7.2 Interpretation of Skew and Spike Parameters

Analysis and description of the DC thus far in this study has considered the composite DC, which isolates the mean diurnal signal from the transient non-diurnal weather systems that are observed on any given day. There is, of course, much day-to-day variability in practice because the convection and precipitation driven by the onset of solar radiative forcing every morning is highly dependent on the initial state of the atmosphere. Indeed, there may be so much day-to-day variability that there is no individual day during which precipitation closely follows the composite cycle. It is difficult to assess the degree of day-to-day variability from the composite alone. For example, if the degree of day-to-day variability is low, a DC with positive skew may be interpreted as having a systematic rapid intensification of precipitation followed by a systematic gradual weakening, whereas if the day-to-day variability is high, a positive skew DC may instead be interpreted as having a consistent, systematic

timing of precipitation onset but an inconsistent precipitation event duration.

In order to assess the degree of day-to-day variability and constrain dynamical hypotheses for positive and negative values of skew and spike, an event-based analysis was performed in select locations to determine the frequency of precipitation event initiations, event maxima and event terminations (as observed at the location) at each time of day. The precipitation time series of the same 1800 DJF days was used, in each case averaged across a 0.5° by 0.5° box with similar DC parameter values throughout the box in order to minimise noise while avoiding averaging beyond an area of coherent uniform diurnal regime. A precipitation threshold of 0.02 mm hr^{-1} was chosen to identify precipitation initiations and terminations. Only "major precipitation events" — those that registered a maximum precipitation rate of at least 5 mm hr^{-1} — were counted. The low proportion of major precipitation events lasting more than 24 hours were omitted in calculations involving duration.

Such an analysis has the potential to be afflicted by artificial initiations and terminations resulting from discontinuities in the interpolated precipitation time series. In IMERG v05, where interpolations are calculated according to infrared sensors in geostationary orbit, such artificial discontinuities might have aligned at the same time of day, with potentially significant influence on the event-based analysis. However, the interpolations in the IMERG v06 data product used in this study are instead based on numerical model data, primarily from MERRA-2, therefore any discontinuities in the time series are not anticipated to systematically align at a consistent time of day.

2.7.2.1 Positive spike

Positive spike is perhaps the case with the most well-constrained interpretation. At extreme positive values, the composite shows a rapid increase shortly followed by a rapid decrease, meaning that the diurnal component of precipitation must arrive at almost exactly the same time of day on any day that it manifests and last for a very short time. Less extreme positive values allow for longer precipitation events and/or more day-to-day variability in the exact timing of initiation and termination, but on any given day any diurnally-driven precipitation is still highly constrained. The most positive values observed are in coastal land areas which are close to great lengths of coastline, including many small islands, the thin island of Java and narrow northern Sumatra (Figure 2.5d). Such locations are likely to experience intense low-level wind convergence in the

afternoon due to the convergence of moisture-rich sea-breezes from multiple directions, which would induce a strong updraught and trigger rapid initiation and intensification of precipitation (Baker et al., 2001). There is also likely to be less day-to-day variability in diurnal regime in such locations than in locations with a single, approximately linear coastline nearby, where day-to-day differences between onshore and offshore background wind regimes strongly influence the evolution of diurnal precipitation systems (Peatman et al., 2021) — background winds from most directions are likely to be onshore with respect to some part of the nearby coastline. The event-based analysis over the part of eastern Java marked in Figure 2.1a supports a very consistent timing of initiation (Figure 2.8a), with 93% of major precipitation events initiating between 0800 and 1600 LST. A comparatively short median major precipitation event duration of 11.0 hours is also found.

2.7.2.2 Positive skew

There is substantial overlap between areas of positive spike and positive skew, and both of these idealised DC shapes have the common feature of a rapid increase (Figure 2.5). Three hypotheses are considered that may result in the gradual decrease observed after the rapid increase observed in positive skew areas: 1) day-to-day variability is insignificant and every individual day features rapid intensification and gradual weakening of precipitation at consistent times (Figure 2.9a); 2) precipitation events are alike in duration but variable in timing, with the distributions of initiation time, maximum time and termination time all featuring (statistical) positive skew (Figure 2.9b), and; 3) the time of initiation is consistent day-to-day, but the event duration (and therefore the termination time) is highly variable (Figure 2.9c). The event-based analysis finds that the timing of the precipitation maximum of major precipitation events is, on average, closer to the initiation time than the termination time over positive skew areas, particularly over southern Borneo (Figure 2.8b) where mean post-maximum precipitation endures over two hours longer than mean pre-maximum precipitation. This frequent asymmetry in individual major precipitation events over positive skew areas is consistent with hypothesis 1 above. One dynamical possibility with which this hypothesis is consistent is a systematic transition from intense but brief convective precipitation to less intense but potentially longer-lasting stratiform precipitation (e.g. Worku et al., 2019).

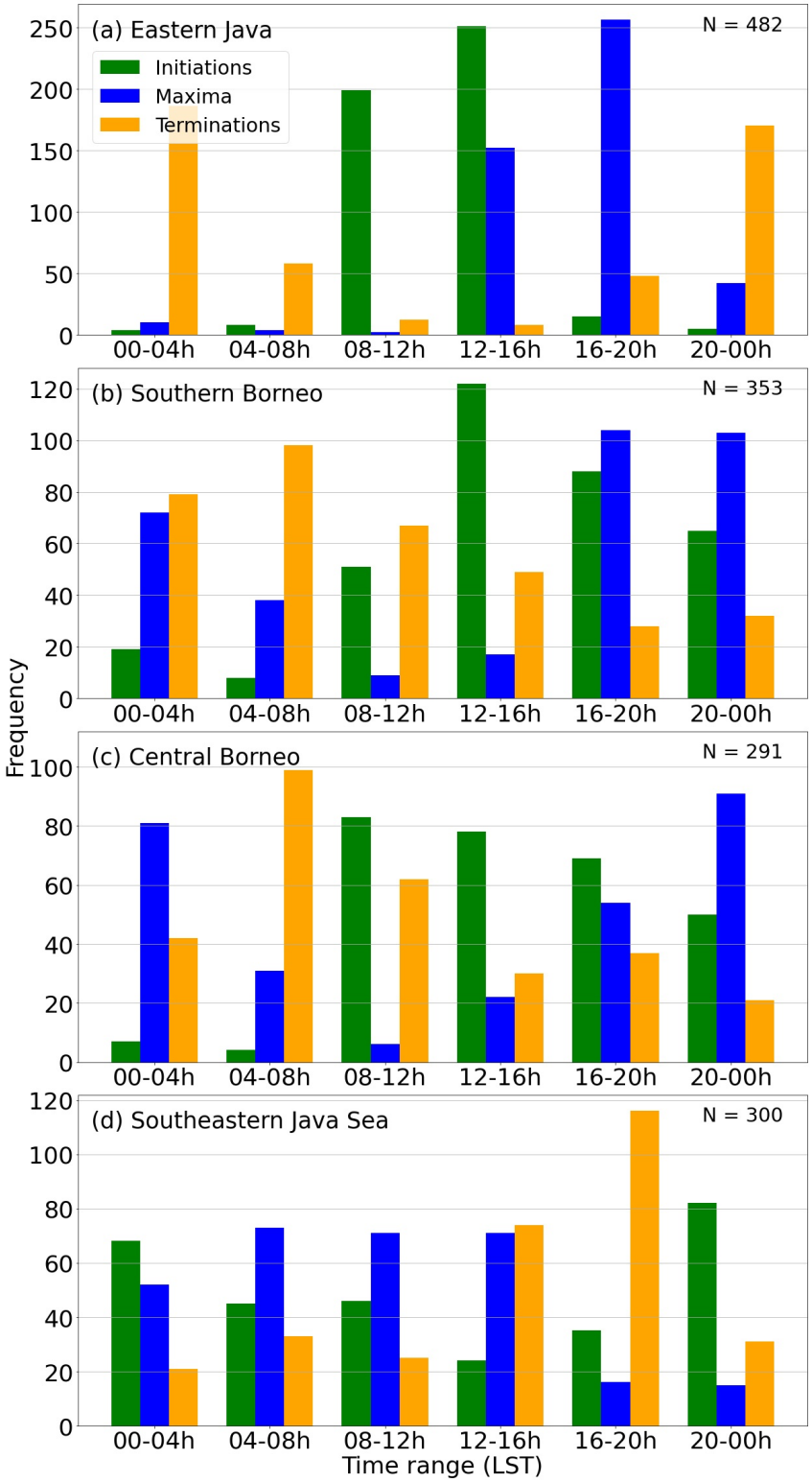

Figure 2.8: Frequency histograms for the timing of initiation (green), maximum (blue) and termination (orange) of individual major precipitation events at the case study locations shown in Figure 2.1a: (a) eastern Java; (b) southern Borneo; (c) central Borneo, and; (d) the southeastern Java Sea. The number of major precipitation events observed at each location is given in the top right of each subplot. Time ranges are in LST for each location.

The distribution of event durations has a standard deviation of over four hours, which infers a role for day-to-day variability in controlling the duration of precipitation events in positive skew areas, which is a key feature of hypothesis 3 (Figure 2.9c). The contrast of consistent initiation timing and less consistent termination timing over the southern Borneo area (Figure 2.8b) is also most consistent with hypothesis 3, and not consistent with hypothesis 2 for which the distributions of event initiations and terminations should be similarly consistent. A dynamical mechanism that may achieve this contrast in initiation and termination consistency is advection of diurnally-initiated weather systems by background winds. The development of diurnally-driven deep convective cells is relatively independent of the background weather conditions (e.g. Da Silva & Matthews, 2021), being driven by the strong, temporally consistent and land-locked surface heating contrast. However, once the diurnal convective system has developed and mid-tropospheric stratiform cloud has spread broadly around the convection centre, the land–sea surface heating contrast is inhibited and stops anchoring the convection centre. This leaves the precipitating convection centre susceptible to horizontal advection by strong background winds. Variability in the speed and direction of these background winds may then be critical in determining the local precipitation termination time in positive skew areas. Peatman et al. (2021) demonstrated the strong influence of background wind velocity on diurnal precipitation propagation over southern Sumatra, while the timing of the onset of precipitation over land appears to be consistent between the three background wind regime clusters identified. In summary, over positive skew areas there is clear evidence supporting a consistent precipitation initiation mechanism, and evidence that both a systematic transition to weaker precipitation and day-to-day variability contribute to the gradual composite weakening associated with a positive value of the skew parameter.

2.7.2.3 Negative skew

Negative skew of the DC points to the presence of a consistent rapid decrease in precipitation rate following a more gradual increase. Such cases are found predominantly far from coastlines, in inland areas and over relatively distal waters (Figure 2.5a). Mirroring the three hypotheses for positive skew, three hypotheses are considered that explain how day-to-day variability in precipitation events leads to negative skew DCs: 1) day-to-day variability is insignificant and every individual day features gradual intensification and rapid

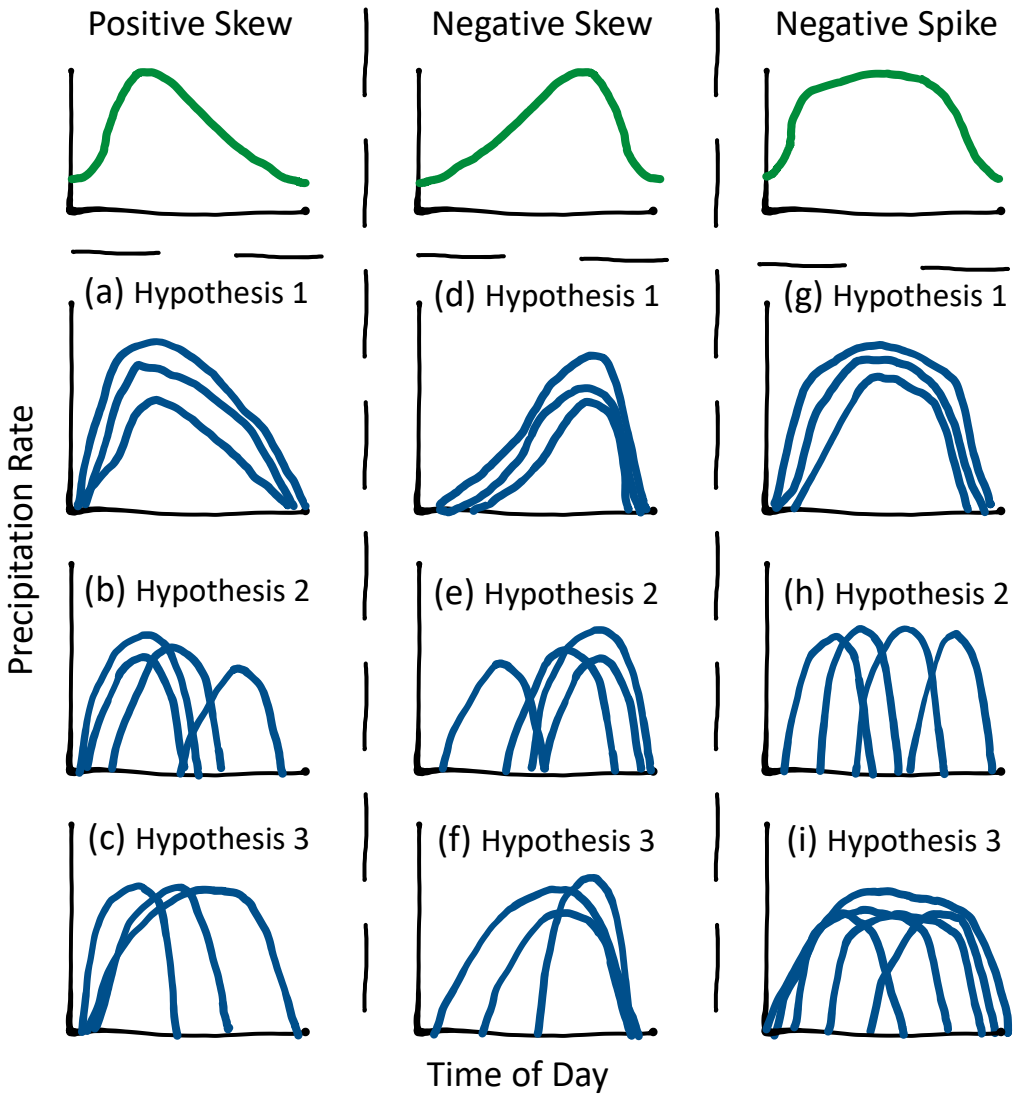

Figure 2.9: Schematic of hypotheses of the range of individual precipitation events (blue) that may combine to produce DCs with positive skew, negative skew and negative spike in the composite (green). (a-c) Hypotheses 1-3 for positive skew, (d-f) hypotheses 1-3 for negative skew, and (g-i) hypotheses 1-3 for negative spike. Note that hypotheses of the same number are independent of each other and need not have the same degree of accuracy.

suppression of precipitation at consistent times (Figure 2.9d); 2) precipitation events are alike in duration but variable in timing, with the distributions of initiation time, maximum time and termination time all featuring (statistical) negative skew (Figure 2.9e), and; 3) precipitation may initiate at a broad range of times of day, but most events terminate at a consistent time (Figure 2.9f). Hypothesis 1 for negative skew is ruled out, since the event-based analysis finds that the event maxima in negative skew locations (including central Borneo; Figure 2.8c) tend to average midway through the event or closer to the

initiation. Over central Borneo, there is no evidence in support of a statistically negatively skewed distribution of initiation, maximum or termination times, which contradicts the key expectation of hypothesis 2. There is, however, greater consistency in termination time than in initiation time, which is consistent with hypothesis 3. This is also observed over the negative skew area of the Java Sea, across both positive spike areas (not shown) and negative spike areas (Figure 2.8d), where the distribution of termination times shows a well-constrained modal frequency in the hours around sunset. In contrast, event initiations are more inconsistently dispersed through night time hours over the negative skew area of the Java Sea.

A commonality amongst areas of negative skew is a broadly-spread distribution of initiation times. While the inconsistency of event terminations over positive skew areas was suggested above to be the result of advection by variable background winds, it follows that the inconsistency of event initiations over nearby negative skew areas may be the result of variable arrival time of diurnal convective centres. This inconsistency does not carry further forward to the event terminations, however — over the southeastern Java Sea most event terminations occur in the eight-hour window between 1200 and 2000 LST (Figure 2.8d). This suggests that there may be a consistent precipitation suppression mechanism operating over negative skew areas. One possible precipitation suppression mechanism over water is an offshore-propagating gravity wave that may nucleate over land as deep convection develops. Near-coastal land areas, such as Java and southern Borneo, typically show high spike, which has been linked to a consistent precipitation initiation time and maximum time (Figures 2.5d and 2.8a&b); the strong diurnal signal over Java in particular suggests that strong and consistently timed gravity waves may be nucleated there. The modal frequency of event terminations over the negative skew Java Sea is a few hours later than the modal frequency of event initiations over Java — those few hours of lag are plausibly related to the propagation time of a gravity wave, which would typically propagate at a speed of the order 15-20 m s^{-1} (Mapes et al., 2003), plus Doppler shift by upper-tropospheric background winds. It is less clear what mechanism may be responsible for consistent termination of inland precipitation in the hours around sunrise (Figure 2.8c).

Gravity waves are central to an additional hypothesis regarding the transition from positive to negative skew with distance offshore, observed most clearly to the northwest of Borneo. Peatman et al. (2023) demonstrated the

relative roles of gravity waves and density currents generated by the land breeze; the most intense and most regular overnight precipitation is associated with the slow-propagating density current, while isolated convection and precipitation may occur ahead of the density current front if triggered by a fast-propagating gravity wave. If the density current and gravity wave begin propagating offshore at around the same time in the evening, then near-shore waters will experience the gravity wave followed shortly by the density current, while waters further offshore will experience a longer time lag between the arrivals of the gravity wave and the density current. As such, locations further from shore will show a greater time lag between the onset of composite precipitation intensification (associated with infrequent gravity wave triggering) and peak precipitation associated with the density current; this would appear as more gradual intensification in the composite further from the coastline. However, land breeze density currents are not typically observed to propagate more than a couple of hundred kilometres from the coastline, so this mechanism may fail to explain negative skew much further offshore.

2.7.2.4 Negative spike

Negative spike tends to occur in inland areas, and is also observed in the waters surrounding Java (Figure 2.5d) and around some other land locations with strongly positive spike. Extreme negative values of spike are not observed; these would diagnose the peculiar case where the dominant feature of the DC is a strong suppression of precipitation followed shortly by a strong intensification, occurring at a very consistent time day-to-day. Three hypotheses for how variability in day-to-day precipitation may lead to the moderate negative spike values observed are as follows: 1) day-to-day variability is insignificant and every individual day features precipitation intensification followed much later by suppression, both at a consistent time (Figure 2.9g); 2) precipitation events are alike (and comparatively short) in duration but highly variable in timing (Figure 2.9h), and; 3) there is a period of regular event termination, and a period of regular event initiation shortly after, but precipitation events need not last the entire day in between (Figure 2.9i). As discussed above, decreasing spike parameter allows for increased event duration and/or less consistent timing, and hypotheses 1 and 2 differentiate between these possibilities; a higher typical event duration than positive spike areas would be expected with hypothesis 1, while the event duration may be similar to positive spike areas if hypothesis 2 is more accurate. Hypothesis 3 represents the case where a precipitation

suppression mechanism is the dominant diurnal driver.

The event-based analysis shows different distribution patterns for the two key negative spike areas of inland Borneo (not shown) and the southeastern Java Sea (Figure 2.8d). The distribution of event timings across the negative spike part of inland Borneo is remarkably similar to that over southern Borneo, despite the contrast in spike parameter. Event initiations and event maxima are reasonably consistent, while event terminations are less consistent. The key contrast appears in event duration; due to slightly earlier event initiations and slightly later terminations, central Borneo typically experiences slightly longer-lasting precipitation events than southern Borneo. This is consistent with hypothesis 1 for negative spike. There is, however, a slight decrease in the consistency of the event timing distributions over negative spike central Borneo relative to positive spike southern Borneo, which is consistent with hypothesis 2. The absence of a consistent event termination over negative spike land (unless also featuring negative skew, as discussed above) suggests that a precipitation suppression mechanism is not the dominant diurnal factor, contradicting hypothesis 3. In contrast, the southeastern Java Sea experiences moderately consistent event initiations, highly consistent event terminations, but inconsistent event maxima, with high frequency of event maxima between midnight and 1600 LST (Figure 2.8d). There is also evidence that event duration is systematically longer over the negative spike part of the Java Sea than the positive spike part of the Java Sea (not shown), consistent with hypothesis 1, however the strongly consistent event terminations over the southeastern Java Sea is also consistent with hypothesis 3 (Figure 2.9i). This suggests that a brief and consistent precipitation suppression mechanism is a dominant diurnal driver in negative spike areas only over water. The concentration of negative spike seas around Java (Figure 2.5d) supports the suggestion above that the dominant gravity wave originates from this island, and a similar pattern is observed around the small islands between Sumatra and Borneo. A consistent precipitation termination is observed across much of the Java Sea, even toward the north where the spike is positive, therefore it may be that the diurnal consistency of the suppressive influence of a gravity wave originating from Java does not reduce substantially with distance from Java. Instead, it appears that the northward transition to positive spike results from the decrease in event duration and the increasingly constrained distribution of precipitation maxima.

2.7.3 Applications of New Waveforms

In this study, the skew-permitting waveform (Equation (2.4)) and the spike-permitting waveform (Equation (2.5)) have been applied to satellite-derived tropical precipitation to capture and characterise a range of diurnal behaviour that cannot be accurately described using the FDH. Future work on the DC generated by models will benefit from the skew-permitting and spike-permitting characterisations, which will provide more representative amplitude and phase parameters and the additional characterisation metrics of skew and spike. Having begun to establish the likely dynamical associations of positive and negative skew and spike, the skew and spike parameters may be used to compare and contrast the dynamics of models and observations. Spatial resolution of the DC in models, as well as temporal, is likely to be critical in determining the importance of considering DC details beyond the FDH parameters. In the observational data of this study, it is found that the half-range-weighted mean scaled error across the study area decreases from 0.37 at the native 0.1° by 0.1° resolution to 0.31 at a coarser 1° by 1° resolution, meaning that the FDH is more appropriate for the characterisation of coarser observational data. This may be partially due to a reduction of noise, however, the mean magnitude of each of the asymmetry parameters (which have been established to be largely unaffected by noise) is also slightly lower for the coarsened data. By extension, as computational advances allow for increasing spatial and temporal model resolution and the complexities of the DC become more clearly resolved, the FDH is likely to become increasingly insufficient, and diurnal asymmetries such as those quantified by the skew-permitting and spike-permitting waveforms are likely to become increasingly pronounced.

The observed tropical DC of precipitation is one of many examples across the sciences of a complex but dominantly single-peak cycle. Other phenomena that these waveforms may be well suited to characterise include the annual cycle of sea surface temperature (e.g. Wang et al., 2022), the surface elevation signal associated with shallow water tidal constituents (e.g. Zhang et al., 2018) and the vertical isopycnal displacement signal associated with internal solitary waves (e.g. Helfrich & Melville, 2006). For the latter examples, either time or distance may be used as the independent variable. Another example of a cyclic quantity for which these waveforms may be well suited is the phase of the MJO (e.g. Peatman et al., 2014; Bai & Schumacher, 2022). There are likely to be many further characterisation applications beyond the research experience of the authors.

The intuitive range of behaviours that these waveforms provide may also prove useful in idealised modelling studies if applied as parameter drivers, or in characterising its output (e.g. Sobel & Maloney, 2012). For instance, in an atmosphere-only climate model, the DC of sea surface temperature may be idealised to follow the shape of the spike-permitting waveform, and the implications of variable warm layer longevity may be investigated by varying the spike parameter of the driving waveform. Alternatively, a hydrological model might idealise the DC of precipitation to follow the shape of the skew-permitting waveform, and the sensitivity of land drainage to the rate of precipitation intensification may be investigated by varying the skew parameter of the driving waveform.

2.8 Conclusions

In this study, high-resolution satellite-derived GPM-IMERG data were used to analyse the observed temporal and spatial complexities of the DC of precipitation over the MC, and two new waveform approximations were applied to enable intuitive characterisation of these complexities. In previous studies, the FDH has typically been the waveform of choice, but the DC cannot be accurately approximated by a sinusoidal wave in many places. Therefore, characterisation with this simple waveform misrepresents the magnitude of diurnal variability and the time of maximum precipitation and hinders accurate interpretation of the underlying dynamics. By restricting use of the best-fit waveform to areas where a sufficiently accurate characterisation is offered, accurate interpretation is more assured, but the FDH fails to offer an accurate characterisation over many areas with a strong DC such as Java. The two new waveforms developed and applied in this study, the skew-permitting and spike-permitting waveforms which each add one degree of freedom to the shape of the FDH, provide a more complete accurate characterisation of the DC across the MC.

By comparing the phase of the FDH with the time of the peak in the (non-best-fitted) composite DC, it was found that the phase tends to lag behind the peak time by an average of around an hour (and frequently up to three hours) over most land areas. The skew-permitting waveform was shown to be able to accurately capture the rapid intensification and gradual weakening of diurnal precipitation over land and produce a phase parameter which is more

accurate with respect to the observed peak time. The amplitude parameter of the FDH was shown to significantly under-represent the true magnitude of diurnal variability observed over land areas including Java, parts of western Sumatra and many minor islands, and it was found that the spike-permitting waveform is able to capture the full magnitude of the brief but strong diurnal peak in precipitation in these areas. On average across the study area, the spike-permitting waveform was shown to provide the greatest improvement in diurnal variability characterisation, with waveform characterisation considered sufficiently accurate over more than 90% of the key subset of the study area with one dominant diurnal maximum-minimum pair. The DC over the eastern lowland areas of Sumatra, Borneo and peninsular Malaysia features two distinct diurnal maximum-minimum pairs, therefore these areas require a more complex multi-peak characterisation beyond the scope of this study, however these areas tend to experience a weaker DC than single-peak areas.

The more representative values of the phase parameter of the skew-permitting waveform and the amplitude parameter of the spike-permitting waveform will help to ensure unbiased assessment of model performance at DC generation. The newly developed skew parameter and spike parameter distributions can be used to constrain the diurnal dynamical mechanisms at play locally. In the observational data considered here it was found that positive spike and positive skew are associated with precisely timed rapid intensification of diurnal convection and precipitation, while negative skew is associated with a variably timed initiation of precipitation and a more regular suppression. Negative spike appears to be associated with high day-to-day variability in the DC over land, while over water it appears to diagnose a strong, precisely timed precipitation suppression mechanism, which is suggested to be the result of afternoon gravity waves nucleated over Java.

Future work will use this characterisation methodology to assess model performance, and investigate whether the same mechanisms are responsible for positive and negative skew and spike DCs. It is hoped that the new waveforms developed, investigated and made available here will be applied more broadly across the sciences in scenarios where qualitatively intuitive characterisation of a single-peak cycle is desired. Programming code (in Python programming language) to enable form-fitting of cyclic data with the skew-permitting waveform and the spike-permitting waveform is publicly available at https://github.com/jm-mustafa/Single_Peak_Waveforms.

Chapter 3

Characterisation of model-generated diurnal cycles of precipitation over the Maritime Continent

3.1 Introduction

The previous chapter established the strength and complexity of the observed diurnal cycle (DC) of precipitation over the Maritime Continent (MC). As a result, there are also strong interactions between the DC and lower-frequency tropical modes of variability, such as the Madden-Julian Oscillation (MJO) and convectively-coupled equatorial Kelvin waves, which lead to a substantial modulation (often weakening) of the convective signature of the lower-frequency modes of variability as they cross over the MC (e.g. Oh et al., 2012; Peatman et al., 2014; Birch et al., 2016; Lu et al., 2019; Worku et al., 2020). This modulation or weakening is commonly referred to as the "MC barrier effect", and many recent studies support a critical role for the DC in the barrier effect (e.g. Hagos et al., 2016; Zhang & Ling, 2017; Ajayamohan et al., 2021; Zhou et al., 2021). One proposed mechanism is that a strong DC concentrates precipitation over land and inhibits the formation of mesoscale convective systems over surrounding waters, which in turn smothers the convective signature of the MJO (e.g. Ling et al., 2019b; Savarin & Chen, 2023).

Challenges in accurately simulating the MC barrier effect in global weather models result in an "MJO prediction barrier" (e.g. Kim et al., 2016; Kim &

Benedict, 2023). If observed teleconnection responses are well represented by a model, MJO convective activity over the Pacific Ocean in the model may lead to predictable teleconnection responses in areas such as the North Atlantic Ocean (e.g. Cassou, 2008, Vitart & Molteni, 2010; Lee et al., 2019). However, this source of intra-seasonal predictability cannot be accurately extended back beyond the prediction barrier to MJO convective activity over the Indian Ocean. Many models exaggerate the strength of the MC barrier effect, leading to too many MJO events being blocked by the MC, and these blocked MJO events have been shown to offer shorter-lasting potential predictability than those events that cross the MC (Abhik et al., 2023). It follows that accurate simulation of the DC over the MC in global weather models is a condition that must be met in order to fully harness the intra-seasonal predictive potential offered by MJO dynamics.

In their analysis of biases in the DC of precipitation simulated across a range of 20 global climate models (GCMs), Baranowski et al. (2019) demonstrated that GCMs tend to misrepresent the mean distribution of precipitation rate across the MC and also misrepresent the amplitude of the DC relative to the mean rate. There are some commonly observed biases, including a dry bias over the eastern Indian Ocean and an underestimated land–sea contrast in the relative DC amplitude, however many GCMs also feature more unique bias distributions. There is also substantial variability between models in the skill with which the DC phase is represented. In regional climate models, which are frequently run at higher resolution than GCMs but often still require convective parametrisation schemes, the key features of the DC of precipitation tend to be represented more reliably, with some convective parametrisation schemes found to be more successful than others (e.g. Love et al., 2011; Bhatt et al., 2016). Running models at a convection-permitting resolution has been suggested to be necessary in order to simulate key features of MC precipitation variability, including the DC, with reliable accuracy (Argüeso et al., 2020; Argüeso et al., 2022). Due to computational expense, existing model investigations over the MC run at a convection-permitting resolution tend to be restricted in their temporal and/or spatial extent. With a restricted spatial domain, the influence of boundary forcing may be strong across much of the domain, making it difficult to determine whether accurate representation of modes of weather variability are actually the result of skillful internal model dynamics. With a limited temporal domain, each mode of variability might only occur a handful of times, or perhaps not even complete a typical cycle, and so it might not be

prudent to conclude that the results are representative of the long-term diversity of variability.

In this chapter, output from a convection-permitting configuration of the UK Met Office (UKMO) Unified Model (MetUM) and from a convection-parametrised counterpart are discussed. Each model configuration was run across a relatively large spatial domain covering much of the MC, and ten three-month boreal winter hindcast simulations were performed. These suites of model runs provide new insight into the skill of a convection-permitting model at simulating key modes of weather variability with minimal boundary forcing influence, relative to the skill of a convection-parametrised model. The structure of the remainder of this chapter is as follows: Section 3.2 details the configuration of the two MetUM hindcast suites. Section 3.3 summarises an existing analysis of the mean states, presents key metrics describing the composite DC and compares each of the model suites with the corresponding composite DC in IMERG. Section 3.4 discusses the skill and limitations of the convection-parametrised and convection-permitting model set-ups in simulating diurnal processes.

3.2 Data and Methods

Two suites of MetUM regional hindcasts were run within the *TerraMaris* project, referred to as MC12 (convection-parametrised) and MC2 (convection-permitting). Each suite contains ten 90-day DJF simulations run over a limited-area domain over the MC. The ten selected seasons — 2003–4, 2005–6, 2007–8, 2009–10, 2012–3, 2014–5, 2015–6, 2016–7, 2017–8, and 2018–9 — were chosen to cover a broad and roughly balanced range of states of the dominant interannual modes of climate variability that operate over Southeast Asia and the MC. For instance, these seasons include 2 to 3 El Niño years and 2 to 3 La Niña years (depending on the chosen index and threshold), 6 years with positive Indian Ocean Dipole (IOD) and 4 years with negative IOD, 6 years with easterly Quasi-Biennial Oscillation (QBO) and 4 years with westerly QBO. Further details of the model configuration are given below, based on the more complete description provided by Howard et al. (in review).

3.2.1 MC12 Hindcast Suite

The MC12 domain extends from 20°N to 20°S and 85°E to 160°E, covering the main islands of the MC, parts of Southeast Asia and northern Australia, the eastern Indian Ocean and the western Pacific Ocean. A standard MetUM grid configuration, N1280, is used with a zonal spacing of 0.140625° and a meridional spacing of 0.09375°, averaging approximately 12 km horizontal spacing in the equatorial region. The science settings of the atmospheric component of MC12 follow the Global Atmosphere 7 (GA7) configuration of Walters et al. (2019). This configuration includes a mass flux parametrisation for atmospheric convection, following Gregory & Rowntree (1990), since the horizontal grid spacing is too coarse to explicitly resolve deep convective processes. Atmospheric conditions are simulated with a time step of three minutes.

Over water, the MetUM atmosphere is coupled to an ocean mixed layer driven by the multi-column *K*-profile parametrisation (KPP; Large et al., 1994), with each atmospheric column coupled to one underlying ocean mixed layer column. The KPP model is updated and recoupled once per hour. Over land, the atmosphere is coupled to soil columns (one soil column per atmospheric column) simulated by the Joint UK Land Environment Simulator (JULES) with four soil levels.

Each hindcast simulation is initialised at the start of November and the first 30 days are discarded as spin-up time. Atmospheric initial conditions and boundary conditions, which are updated every six hours, are taken from ECMWF Reanalysis v5 (ERA5). Coupling at the ocean-atmosphere and land-atmosphere interfaces is achieved with the Ocean Atmosphere Sea Ice Soil (OASIS) coupler (Valcke, 2013) and, for simplicity, coastal grid cells are classified as either fully land or fully ocean. The data sources used to initialise and maintain the KPP ocean mixed layer model and the JULES soil moisture model are detailed in Section 3.2.3.

To standardise the analysis of the DC, the composite DC of precipitation is interpolated onto a 0.1° by 0.1° horizontal grid to align with the IMERG observational comparison data. Similarly, the temporal grid is interpolated from 15-minute time intervals to 30-minute time intervals, in line with IMERG.

3.2.2 MC2 Hindcast Suite

The MC2 domain is nested within the domain of MC12 with a buffer zone of 5°, such that it extends to 15°N, 15°S, 90°E and 155°E. 0.02° grid spacing is applied in both zonal and meridional directions, which is approximately 2 km near the equator. The science settings of the atmospheric component of MC2 follow the tropical version of the Regional Atmosphere and Land 2 (RAL2T) configuration of Bush et al. (2023), and since the fine-scale grid configuration is sufficient to resolve deep convective processes, no mass flux parametrisation is applied.

As with MC12, the MetUM atmosphere is coupled to the KPP ocean mixed layer. The horizontal resolution of the ocean mixed layer is not increased relative to the MC12 resolution, meaning that each ocean column interacts with the mean of several overlying atmospheric columns, and each atmospheric column is coupled to its nearest ocean column. This also means that coastlines remain resolved only to the coarser (≈12 km) resolution of MC12. Following the initialisation of the atmosphere of each hindcast simulation at the beginning of November according to ERA5 conditions, boundary conditions are taken from the corresponding MC12 hindcast simulation. Atmospheric conditions are simulated with a time step of one minute.

The composite DC is interpolated onto a 0.1° by 0.1° horizontal grid for uniformity with IMERG and interpolated MC12. For MC2, the new grid is much more coarse than the native grid; an area-weighted average of the original grid cells within each new cell is used to preserve representation of each original grid cell, which also reduces the dominance of noise relative to each individual grid cell. The temporal resolution is also standardised to match the 30-minute time interval of IMERG.

3.2.3 Model Ocean and Land Components

Instead of coupling a computationally expensive explicit model of the ocean mixed layer to the MetUM atmosphere, the KPP model (Large et al., 1994) is used, which parametrises air–sea interactions and represents vertical mixing of temperature and salinity with the use of location-specific calibrated forcing and relaxation. Each ocean mixed layer column, up to 250 m deep, interacts only with the overlying atmosphere, and not with adjacent ocean mixed layer columns. Since the KPP model does not explicitly simulate ocean advection, the ratio of the time step to the grid spacing is not limited by the

Courant-Friedrichs-Lewy condition, therefore a long time step (one hour) in comparison with the necessary atmospheric time step may be appropriately used for computational efficiency while also using a relatively fine vertical grid spacing (70 layers, surface layer 0.8 m deep) for detailed resolution of the ocean mixed layer. The use of the KPP ocean mixed layer model has been demonstrated to limit biases in MC sea surface temperature (SST) to within ±0.5°C (Hirons et al., 2015), in contrast to many other ocean models which feature warm biases of over 1°C (Wang et al., 2022), and consequently simulate a strong wet bias.

For consistency with the data sources used in ERA5, sea surface temperature (SST) data are sourced from the HadISST2.0 data set from the UKMO Hadley Centre up to 2007, and then from the daily foundational Operational Sea Surface Temperature and Ice Analysis (OSTIA) SST (Good et al., 2020) from 2007 to 2019. The reference temperature and salinity fields, towards which the relaxation terms of the KPP model act, are calculated based on data from the Nucleus for European Modelling of the Ocean (NEMO) reanalysis.

The soil moisture profile is initialised according to reanalysis output of the JULES soil moisture model using an atmospheric analysis data set (JRA-55) from the Japanese Meteorological Agency. The initialised state of the soil moisture field is on a coarse 1° by 1° horizontal grid, and the November spin-up time of each hindcast simulation allows for the soil moisture state to equilibrate to the finer resolution of MC12.

3.2.4 Phase Comparison Methodology

The results presented here include comparisons between the DC phase characteristics of the models and IMERG, and comparisons between apparent model biases in phase across the different phase characteristics. Due to the cyclic nature of the phase characteristic, the mean of differences in phase can be misleading: for instance, if the model simulates the phase 11 hours late (+11) in one location, and nine hours early (-9) in another location, the linear mean (+1) opposes the true cyclic midpoint (-11), and is therefore highly unrepresentative. To account for this, area-averaged comparisons of phase or of phase bias are based on the polar midpoint.

The polar midpoint calculation considers the placement of all phases or phase biases on a 24-hour "clock" (i.e. a 2-D circle of unit radius with 0, 6,

12 and 18/-6 at 90° angles). The mean of all points is calculated in Cartesian coordinates, and the radial angle to the mean is converted back into a phase or phase bias. It should be noted that this process results in non-conservative comparisons of phase, meaning that if two measures of phase have polar midpoints of ϕ_1 and ϕ_2, the polar midpoint of the difference between the two measures of phase need not equal $\phi_2 - \phi_1$, although it tends to be somewhat close.

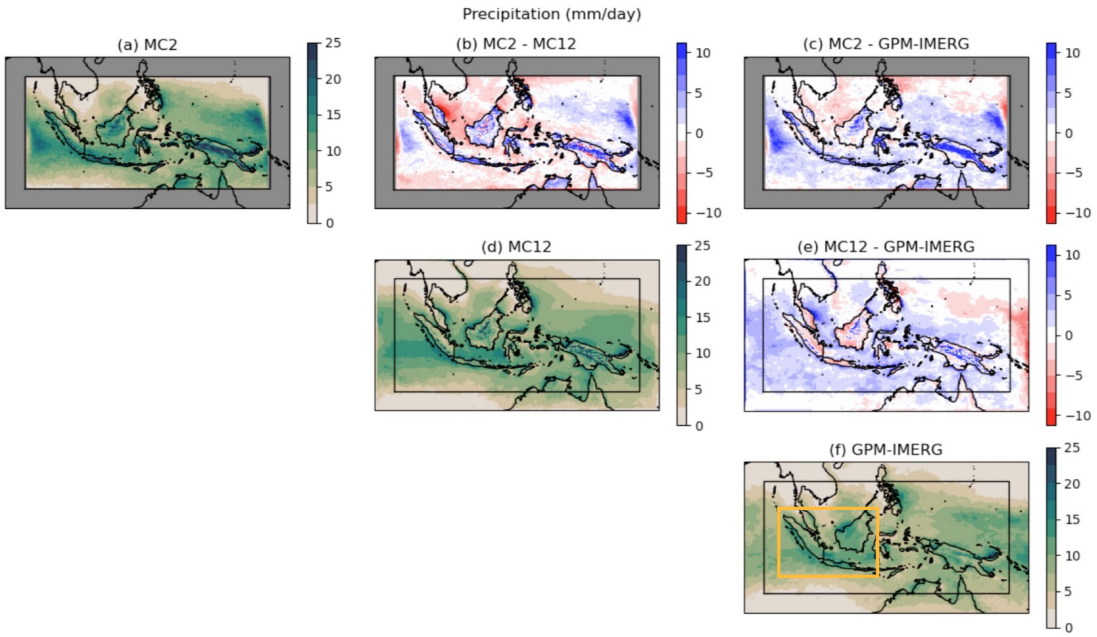

Figure 3.1: Precipitation mean state of (a,d) each of the two hindcast model suites and (f) IMERG over the same ten seasons, and (b,c,e) their differences (note that the colour scheme in these difference panels opposes the red-positive convention used in other results figures). Each panel shows the full domain of the respective model. The orange rectangle in panel (f) marks the western MC domain that is focused on within this thesis. *Image adapted from Howard et al. (in review), Figure 4.*

3.3 Results

3.3.1 Mean State

A brief overview of each of the two hindcast suites has been provided by Howard et al. (in review), and some of their key results will be reviewed here before proceeding to the new detailed analysis of the simulated DCs to which this chapter is dedicated. Their discussion includes an overview of the mean precipitation rate in each of the hindcast suites, summarised in their Figure 4

which is adapted here (Figure 3.1). It was shown that both MC12 and MC2 feature a mean wet bias across the MC domain, of the order of 1 mm day^{-1} in both cases, relative to IMERG (Figure 3.1c&e). This wet bias is consistent with previous MetUM modeling studies across a range of resolutions (e.g. Roberts et al., 2019). The wet bias manifests predominantly over the ocean in MC12, and both models simulate excess precipitation over regions of high topography, including northern-central Borneo. A strong wet bias is observed a few degrees inside of the western and eastern model boundaries of MC2 around the equator. This is believed to be a result of strong boundary effects; in many regional models, the moisture flux convergence imposed at the lateral boundaries is too low to expend the excess atmospheric moisture that results from strong evaporation across the model domain, forcing equilibration by excess precipitation around parts of the boundaries (Goergen & Kollet, 2021). A dry bias over the western Pacific Ocean in MC12 may also be influenced by boundary forcing. Precipitation over land in MC12 is highly focused over high topography, such that lowland areas such as eastern Sumatra and southern Borneo feature a dry bias.

3.3.2 Basic Characteristics

In Chapter 2, a diverse range of parameters were used to characterise and quantify the DC of precipitation. In keeping with the structure of that chapter, this chapter will consider the DC parameters beginning with the most simple — the "basic characteristics" — which are measures of cycle magnitude ("half range") and timing ("peak time") that are not associated with a waveform fit method. Unless otherwise stated, area-averaged results presented in this chapter relate to the western MC region (10°S - 8°N, 94°E - 120°E; Figure 3.1f), for continuity with Chapters 2 & 4.

The high half range of MC2 (Figure 3.2a), particularly over land, is indicative of strong diurnal variability in this convection-permitting model. The MC2 half range is too high in most locations, averaging 0.094 mm hr^{-1}, or approximately one-third (34%), excess diurnal variability relative to IMERG across the western MC region (Figure 3.2c). The positive half range bias in MC2 is most extreme over land (averaging approximately 41% greater than in IMERG), especially over areas of high topography. However, the model wet bias is also generally strongest over land, with an excess in precipitation of 0.072 mm hr^{-1} (17% wetter than IMERG). Therefore, some of the overestimation of the half range

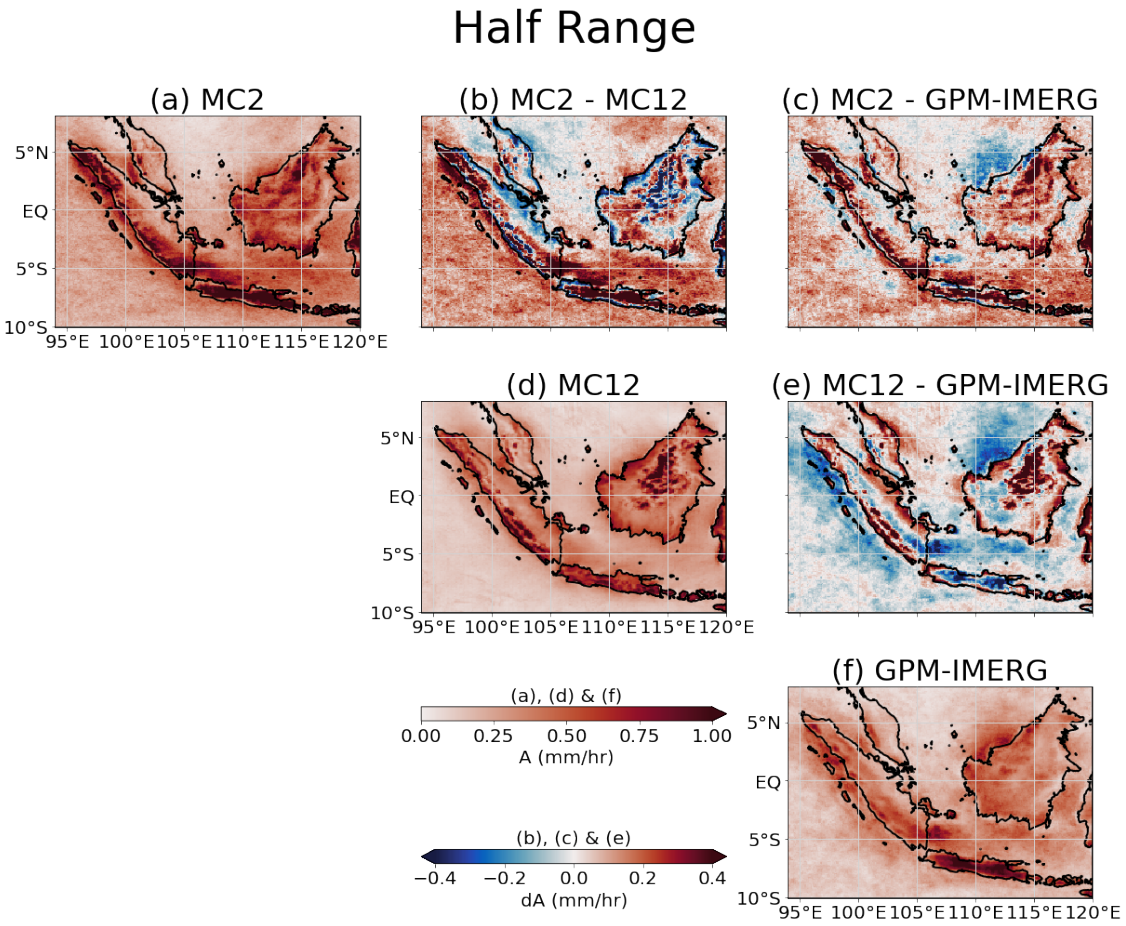

Figure 3.2: Comparison between the DC half range characteristic quantified in model suites and observations across the western MC region, each based on the composite DC from 10 DJF seasons. Following the layout of Figure 3.1, panels on the left of each row show the absolute half range in (a) MC2, (d) MC12, and (f) IMERG. Panels (b), (c) and (e) show the differences between these three measures of half range.

in MC2 can be attributed to the general wet bias, assuming that any model bias in mean precipitation has a linearly proportional influence on the magnitude of diurnal variability rather than a uniform non-diurnal increase across the day. Certain coastal land and lowland areas underestimate the half range in MC2, as do some offshore locations such as the South China Sea near northwest Borneo. The influence of the MC2 wet bias on the high half range is less strong over water. Even over land, however, the model wet bias does not account for the full extent of half range exaggeration. Therefore, when half range is used to quantify the magnitude of diurnal variability, MC2 appears to exaggerate diurnal processes. This apparent exaggeration is dependent on the metric with which DC amplitude is defined, as is discussed in Section 3.3.3.

In MC12, the mean half range across the western MC region is close to that

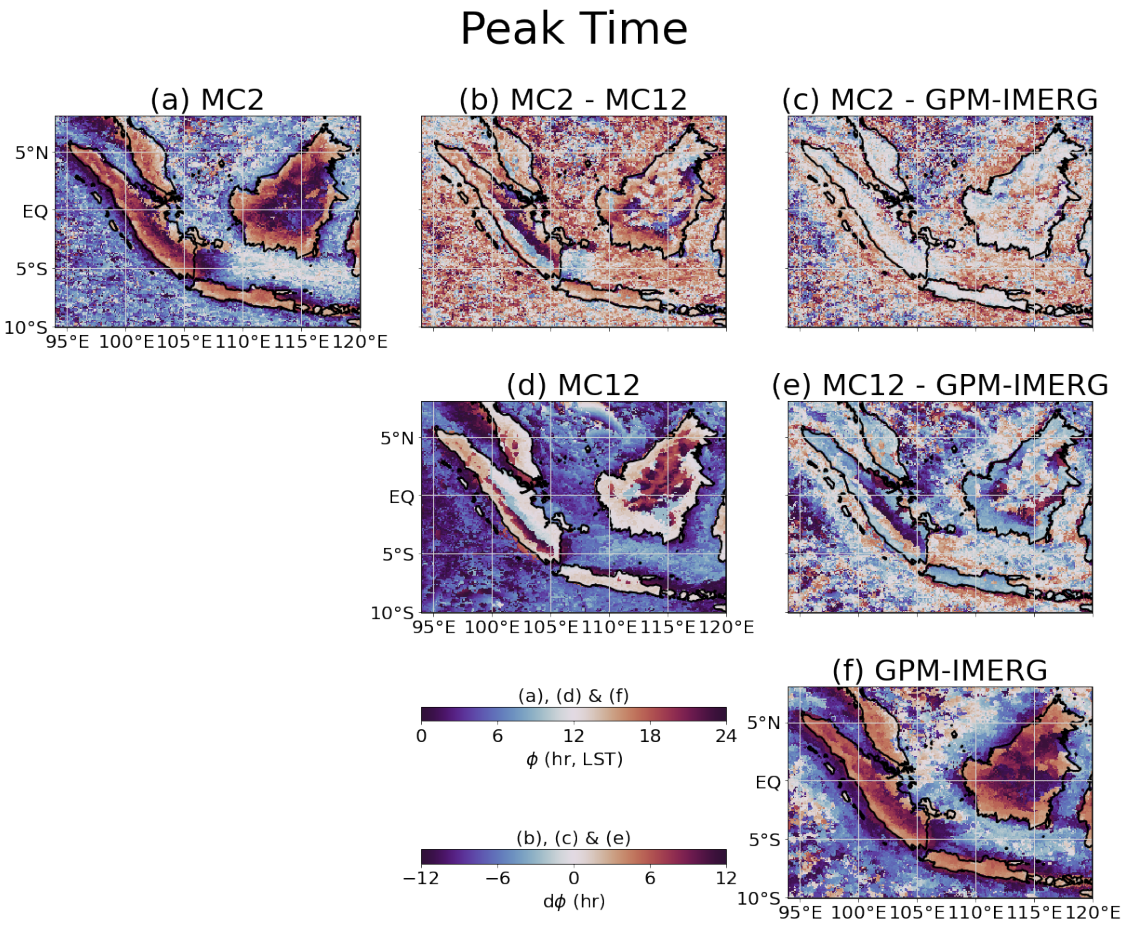

Figure 3.3: As for Figure 3.2, but for the peak time characteristic.

observed in IMERG, however this disguises substantial regional model biases. The half range tends to be too low over near-coastal waters and non-coastal lowland areas, but too high over coastal and mountainous land areas (Figure 3.2e). Unlike for MC2, these half range biases cannot be partially attributed to the model wet bias. In fact, over the western MC domain of MC12, the half range is too low over water (-15%) despite a mean wet bias over water of 26%, and the half range is typically too high over land (29%) despite a mean dry bias over land of nearly 10%. These results suggest that diurnal processes are too strongly land-locked in MC12. Inland Java is an interesting exception to this generalisation, as even though the convection-parametrised model tends to produce strong diurnal variability over high topography elsewhere, it is unable to simulate the unique processes leading to the extreme diurnal variability observed over Java in IMERG (Figure 3.2d&f). The convection-permitting model performs better in this regard (Figure 3.2a&c).

The convection-permitting model also demonstrates more accurate

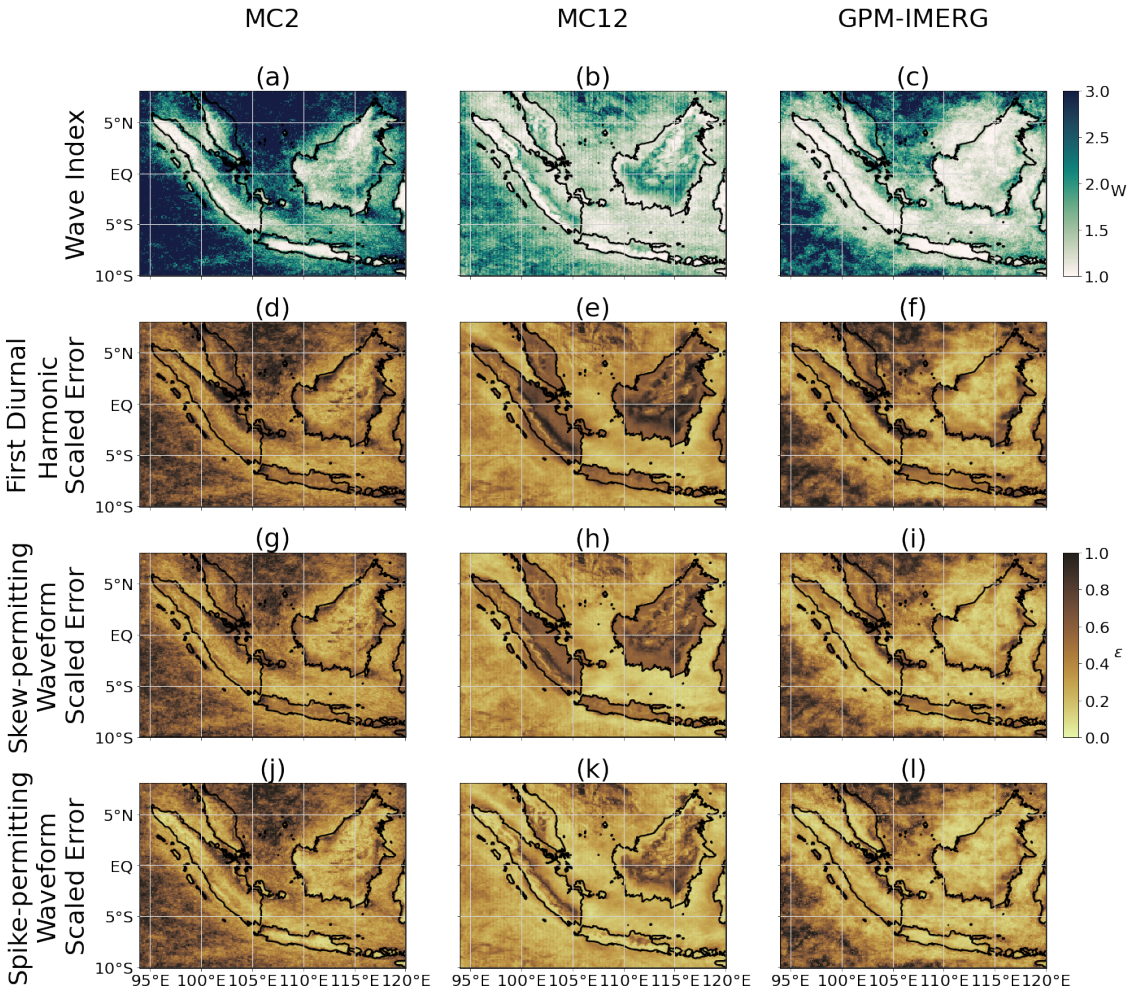

Figure 3.4: Wave index and scaled error metrics for the DC of each data source: (left) MC2, (centre) MC12, and (right) IMERG. Top row shows the wave index, and the following three rows show the scaled error for the FDH, the skew-permitting waveform and the spike-permitting waveform, respectively. See Equations (2.3) and (2.2) for definitions of the wave index and scaled error metrics.

representation of the phase of the DC, as measured by the peak time (Figure 3.3). The peak time in MC2 (Figure 3.3a) shows the same key features as the peak time in IMERG (Figure 3.3f): peak precipitation in the late afternoon and evening over land, with clear inland progression of the peak over Sumatra and Borneo, and peak precipitation overnight through to as late as midday over the Java Sea, but less late over other surrounding seas and oceans. The accuracy of the peak time is very high over land, particularly in near-coastal areas, with a slight tendency towards a late precipitation peak in some parts of inland Borneo (Figure 3.3c). Over near-coastal seas, MC2 peak time tends to be too late, particularly along the northwest coast of Borneo and the south coast of Java. Further offshore, MC2 peak time tends instead to be too early. There is

therefore a weaker contrast in peak time between coastal waters and offshore in MC2 than in IMERG, suggesting that offshore propagation of precipitation is not accurately simulated in the convection-permitting model. The MC2 peak time also becomes dominated by fine-scale noise less far offshore than in IMERG, which suggests that offshore propagation mechanisms in MC2 are relatively weak.

While the convection-parametrised model generally shows the correct first-order spatial pattern in peak time (i.e. an afternoon or evening peak over land and an overnight peak over water, Figure 3.3d), there are major differences between the peak time of this model suite and IMERG (Figure 3.3e). Over near-coastal land, the precipitation peak in MC12 tends to occur shortly after midday, a few hours earlier than in IMERG (Figure 3.3d). Over Sumatra and Borneo, inland areas generally fall into one of two peak time categories: evening peak and late morning peak. Late morning peak time in MC12 contrasts strongly with the late evening peak time observed in these same areas in IMERG, which are primarily in lowland areas to the east of high topography. The peak time characteristic gives the impression of discontinuous diurnal behaviour between these two inland categories, however inspection of the complete 24-hour DC exposes the bimodal diurnal distribution of precipitation across non-coastal lowland areas. This is reflected in the wave index of order two in these areas (Figure 3.4b). MC12 simulates the peak time of precipitation slightly more accurately over coastal seas, however the peak time further offshore tends to be hours too late. As for MC2, this is suggestive of poor representation of the processes driving offshore propagation of precipitation.

3.3.3 Waveform Amplitudes and Phases

Since the basic characteristics are highly susceptible to outliers, describing the DC with a waveform approximation can be an effective way to reduce the contribution of outliers to noise. In Chapter 2, three waveforms were used to describe the DC: the first diurnal harmonic (FDH), a skew-permitting waveform and a spike-permitting waveform. For each of these waveforms, the difference in amplitude (Figure 3.5) and in phase (Figure 3.6) between each model and observations is considered. The qualitative patterns of model bias in amplitude and phase are very similar for all definitions of amplitude and phase, including the half range (Figure 3.2c&e) and the peak time (Figure 3.3c&e) described in Section 3.3.2.

Some subtle quantitative differences are observed, however. Generally, the model bias in waveform amplitude tends to be proportionally less extreme than the model bias in half range. In MC2, the model bias in mean half range across the western MC region (34%) is more positive than the model bias in the mean of any of the three waveform amplitudes (19%/19%/23%), and this holds when considering the DC over either land or water in isolation. In other words, MC2 appears to do a better job of simulating the observed DC with the correct amplitude when the amplitude is quantified by a waveform. This is likely due to the composite DC in MC2 being more affected by noise than IMERG, which is demonstrated by the higher wave index of MC2 (Figure 3.4a&c).

On average across the region for MC12, the model bias in the amplitude of the FDH and of the best-fit skew-permitting waveform is proportionally less extreme than the model bias in half range, as for MC2. However, the amplitude of the best-fit spike-permitting waveform is substantially greater in MC12 than in IMERG, particularly over land where there is a positive model bias of 37%. This exceeds the mean half range model bias of 29% observed over land in MC12. The difference between model bias based on the best-fit spike-permitting waveform amplitude and model bias based on the other amplitude metrics is positive across most land area, but it is greatest over some localised regions around high topography over Sumatra and Borneo. In such localised regions, the DC in MC12 features a single extreme, but brief, maximum in precipitation in the evening, as will be discussed further in Section 3.4. In general, the spike-permitting waveform is more able to morph to the intense but short-lasting maxima and minima in precipitation observed over land in MC12 (also observed in IMERG, but not to the same degree) than the other waveforms, resulting in much greater waveform amplitude.

While the half range over water in MC12 is widely too low, particularly over coastal seas (Figure 3.2e), the waveform amplitudes show a less negative model bias which actually tends toward a positive model bias in half range with distance offshore (Figure 3.5b,d&f). This suggests that the DC over water in MC12 does not typically feature extreme outliers, and therefore that there is a consistent DC over water that is not subject to substantial noise from transient weather systems. The low wave index over the waters of MC12 attest to the comparative lack of noise in the convection-parametrised model (Figure 3.4b).

For both models and over both land and water, the model bias in phase for both the FDH and the best-fit spike-permitting waveform is generally more negative than the model bias in peak time. This means that the models appear

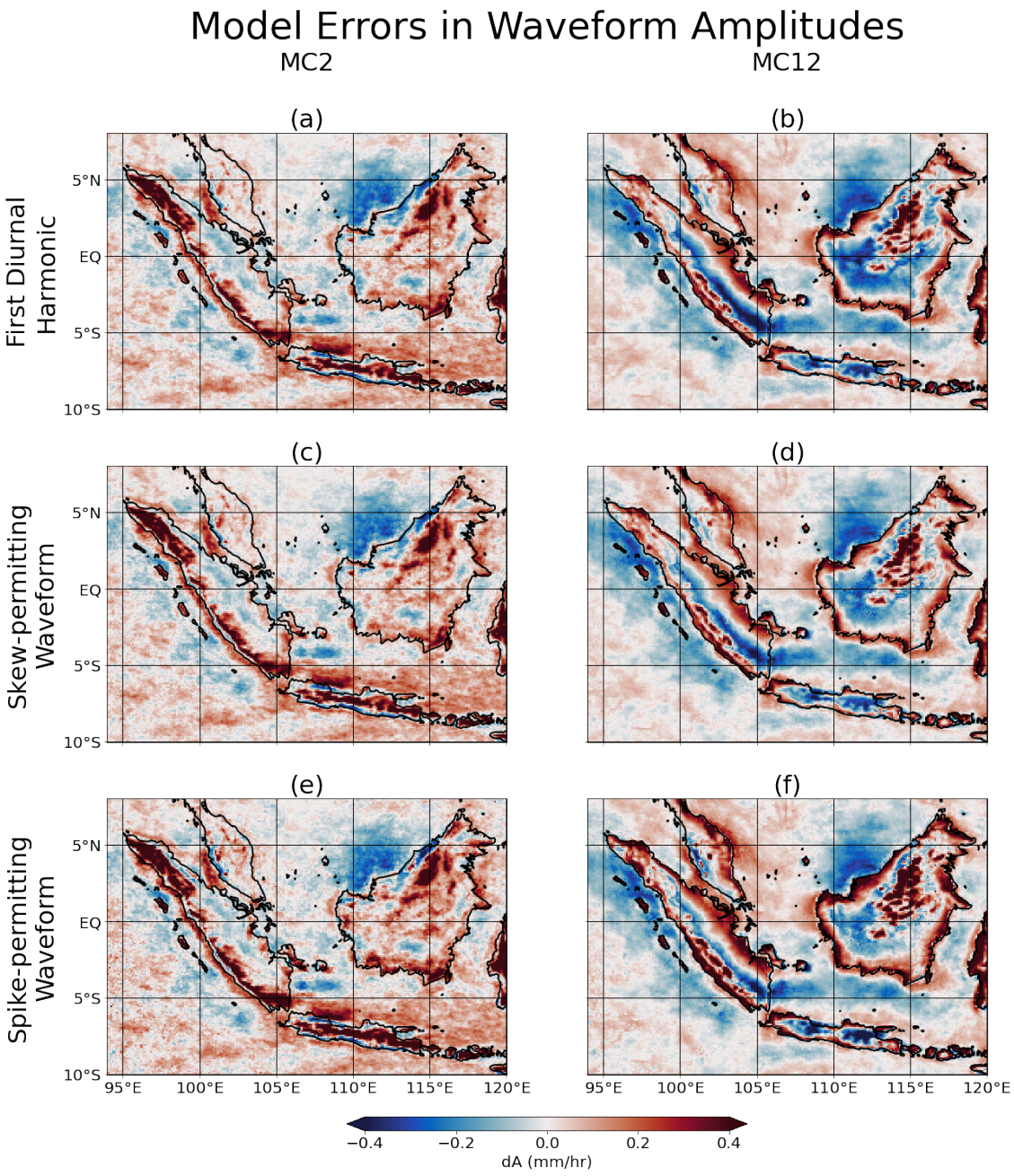

Figure 3.5: Model biases across a range of waveform measures of DC amplitude, relative to the equivalent definition of amplitude in IMERG. Left column relates to MC2 and right column relates to MC12. Top row shows the difference between the FDH amplitude for each model relative to IMERG, and the following two rows show the same but for the amplitudes of the skew-permitting waveform and the spike-permitting waveform, respectively.

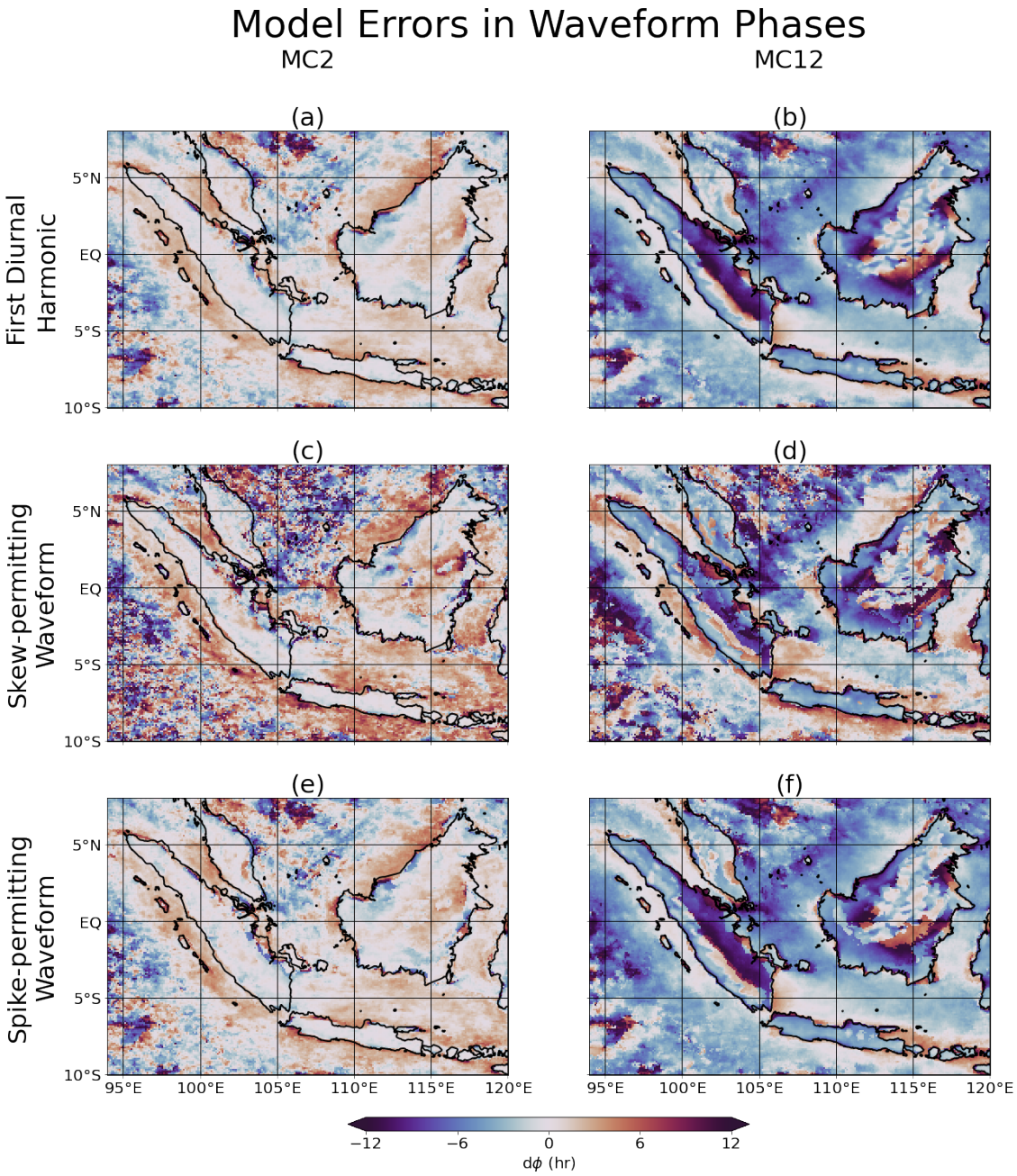

Figure 3.6: As for Figure 3.5, but for waveform measures of DC phase.

to simulate an earlier precipitation peak relative to observations when the phase is quantified with these waveforms, in comparison to the peak time characteristic. Using the polar midpoint method for averaging phase biases (Section 3.2.4), MC12 has an area-averaged peak time bias of -2.1 hours (a negative value implies the model peaks too early), but quantifying the phase bias with the phase of the FDH or the best-fit spike-permitting waveform leads to an area-averaged phase bias of approximately -3.1 hours. Effectively, MC12 appears to simulate the phase of the DC less accurately when quantified using the FDH or spike-permitting waveform.

Similarly with MC2, the FDH and best-fit spike-permitting waveform present the area-averaged model phase bias as less positive than the peak time, however since the phase bias tends to be positive across MC2 (indicating a late model precipitation peak), this means that MC2 phase simulation appears more favourable when quantified by either of the above waveforms ($+0.3$ hours) than when quantified by the peak time ($+0.7$ hours). For both models, the phase of the best-fit skew-permitting waveform leads to an area-averaged phase bias measurement close to that of the peak time. The discrepancy in phase bias between metrics is less extreme for MC2 than for MC12. The lesser dependence of the phase bias on the chosen phase metric for MC2 is one indicator that the nature of diurnal variability in MC2 is comparable with the nature of diurnal variability in IMERG, and that the general patterns of cycle asymmetry may be reasonably accurate.

3.3.4 Waveform Skew and Spike

In Section 2.6, the concepts of the skew and spike of the DC were introduced as means to contextualise waveform amplitude and phase with measures of composite DC asymmetry. Both the skew parameter and the spike parameter are quantified on a scale from -1 to 1. Non-zero skew infers asymmetry in the rate of precipitation intensification before the peak and precipitation weakening after the peak, with positive values indicating rapid intensification. Non-zero spike infers asymmetry in the durations of the precipitation peak and the precipitation trough, with positive values indicating a brief but extreme peak in precipitation.

The best-fit skew-permitting waveform and best-fit spike-permitting waveform were calculated at every location across the western MC region for both MC12 and MC2, resulting in an associated skew parameter and spike parameter at every location. However, as in Section 2.6, these values are only

considered where the waveform offers a sufficiently accurate characterisation as assessed by the scaled error metric (Equation (2.2), using the same sufficiency threshold of 0.4 as in Chapter 2). Generally, the waveforms characterise the DC slightly less well in MC2 than in IMERG, but characterisation is generally strongest in the same regions, over Java, the western areas of other major land areas, and near-coastal seas (Figure 3.4). In contrast, the waveforms provide poor approximations of the DC over land in MC12, with the exception of the spike-permitting waveform over near-coastal land and high topography, however they all provide good approximations over water, even far offshore.

In MC2, the skew parameter is positive across the near-coastal land areas of southwestern Sumatra and northern and southern Borneo, and across the near-coastal waters to the southwest of Sumatra (Figure 3.7a). Most other marine areas, including the Java Sea, around the northwest and east coasts of Borneo and the south coast of Java, simulate negative skew, strongest across the northern Java Sea. Inland Borneo also simulates weakly negative skew. This compares quite favourably with the skew observed in the DC of IMERG precipitation; across the area of MC2 sufficiently accurately characterised by the best-fit skew-permitting waveform, the mean model bias in skew is approximately -0.12 (Figure 3.7c). Due to the poor waveform characterisation further offshore, it is difficult to assess whether the tendency in IMERG skew to become more negative further offshore is simulated by MC2.

In MC12, almost no land area is sufficiently accurately characterised by the best-fit skew-permitting waveform, therefore the skew parameter over land in MC12 is not meaningful (Figure 3.7d). However, the best-fit skew-permitting waveform characterises marine areas well, especially close to the coasts, and it is found that MC12 simulates moderately negative skew (of order -0.1 to -0.4) over most near-coastal waters. Some marine areas, including the open Indian Ocean, the Strait of Malacca (between Sumatra and peninsular Malaysia) and the southeastern Java Sea, instead feature moderately positive skew. The skew simulated in MC12 is substantially too negative over near-coastal waters (Figure 3.7e), typically by order -0.1 to -0.5. If the skew parameter were to be considered over land in MC12, it would manage to offer a fair comparison to IMERG skew in some coastal and high topography areas, however the simulated skew is incoherent and highly erroneous across most land area; 42% of MC12 land area has an absolute model bias in skew of greater than 0.5, compared with 18% of MC2 land area.

The spike parameter in MC2 is, much like the skew parameter, considered

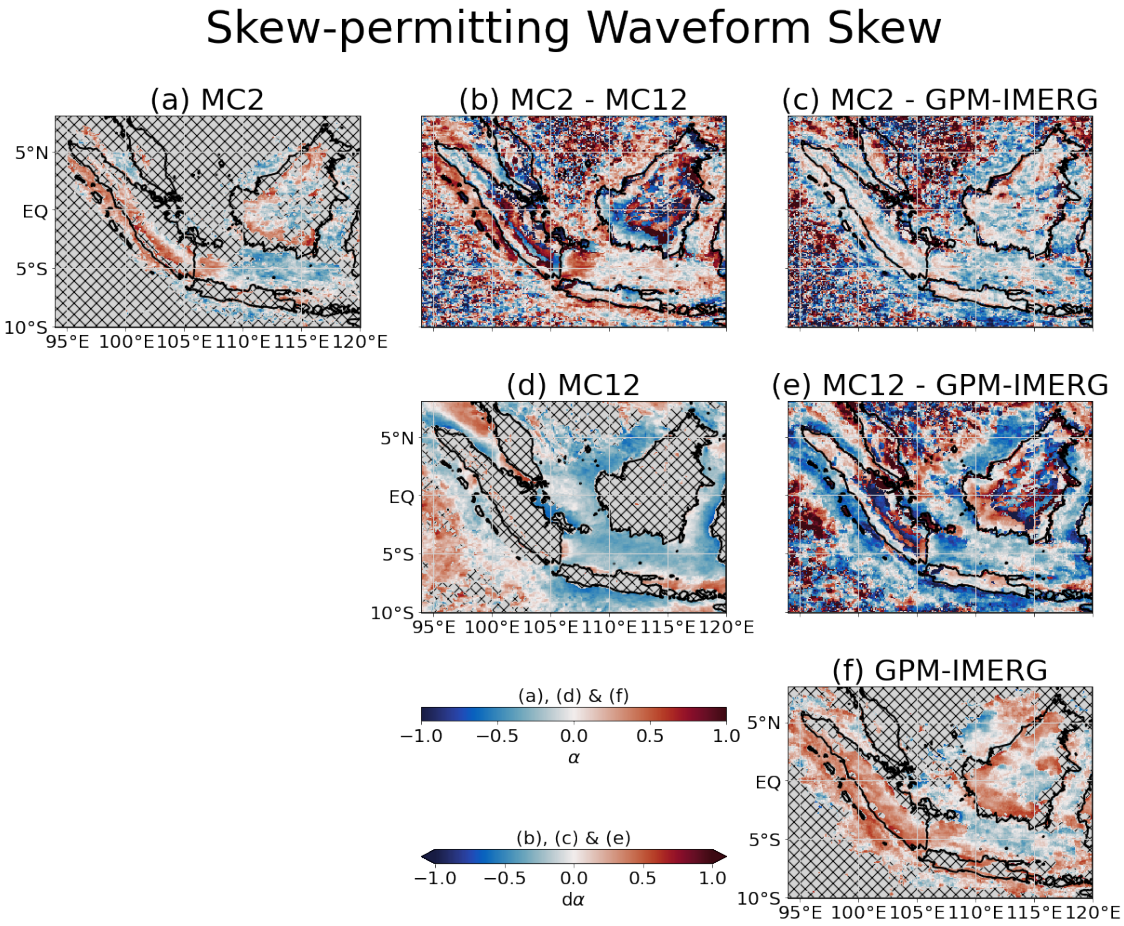

Figure 3.7: As for Figure 3.2, but for the skew parameter of the best-fit skew-permitting waveform. Skew values are linearised according to the procedure described in Section 2.6.1. In panels (a), (d) & (f), hatching is applied where $\epsilon > 0.4$ for the best-fit skew-permitting waveform (see Equation (2.2)), to restrict interpretation to locations where the best-fit skew-permitting waveform provides a sufficiently accurate characterisation of the DC.

representative only over land and near-coastal waters, however the island of Java is also sufficiently accurately characterised (Figure 3.8a). Positive spike dominates across MC2; strongest over Java (typically of order 0.4 to 0.6) and some of the minor islands, moderately strong across much of southwestern Sumatra and near-coastal Borneo (typically of order 0.2 to 0.5), and weakly positive over most near-coastal waters and parts of inland Borneo (typically of order -0.1 to 0.2). The simulated spike parameter strongly resembles the spike observed in the DC of IMERG (Figure 3.8c). Over most land, particularly Java, the bias in the spike parameter is negligible. Over water, there are some regional biases including a positive spike bias over the Java Sea and a negative spike bias around the southwest coast of Sumatra, however these biases are small and the regional average of spike in MC2 is highly accurate.

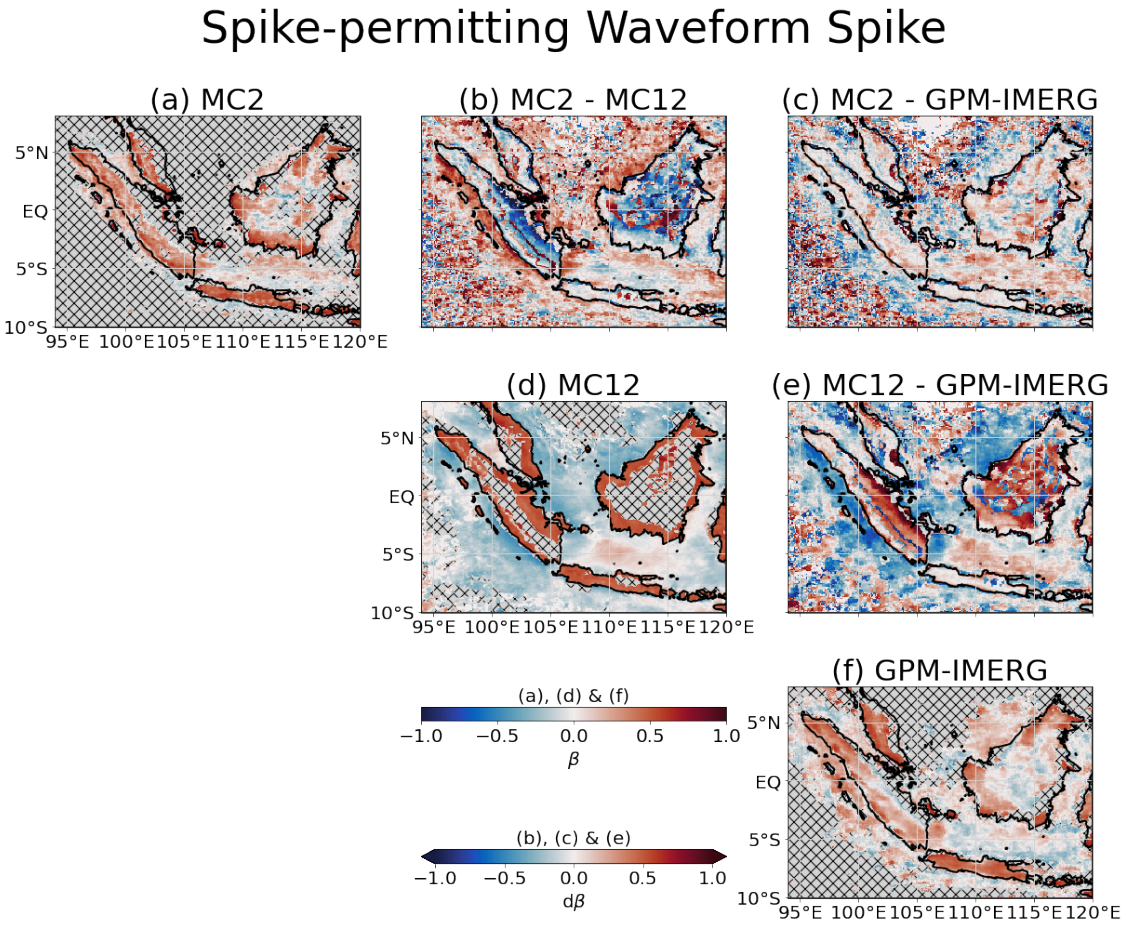

Figure 3.8: As for Figure 3.7, but for the spike parameter of the best-fit spike-permitting waveform. Spike values are linearised according to the procedure described in Section 2.6.2. In panels (a), (d) & (f), hatching is applied as for Figure 3.7, but based on the accuracy of the characterisation of the best-fit spike-permitting waveform.

In MC12, the best-fit spike-permitting waveform surpasses the best-fit skew-permitting waveform by providing a sufficiently accurate characterisation of the DC over near-coastal land and some parts of high topography, as well as over the surrounding waters (Figure 3.8d). There is an approximate land–sea binary in spike parameter in MC12, with land simulating a near-uniform, strongly positive spike (typically of order 0.4 to 0.6 where sufficiently accurately characterised), and surrounding waters simulating a moderately negative spike (typically of order -0.3 to 0). The main exception to this is the central Java Sea, which features weakly positive spike. Over near-coastal land, this strongly positive spike compares well with the spike observed in IMERG (Figure 3.8e), however the inland comparison is quite incoherent and erroneous. Over water, however, the pattern of spike in MC12 opposes the observed pattern, where spike is negative over much of the Java Sea but positive across most other near-coastal marine areas (Figure 3.8f).

3.3.5 Model–Observations Correlations

Both the basic characteristics and the best-fit waveforms are useful tools with which to characterise DCs. However there are locations in both observations and models, particularly over inland areas of MC12, where the complexity of the local DC renders these characterisation tools less appropriate. Correlation analysis between the observed and modelled DC at each location provides a simple assessment of model performance, irrespective of the complexity of either cycle.

The Pearson correlation coefficient (r) for MC2 shows that correlation is very strong across most land area, with the eastern lowland areas of Sumatra and Borneo among the less strongly correlated areas (Figure 3.9a). The DC over near-coastal waters also reliably correlates strongly, with correlation weakening toward approximate neutrality far offshore. 46% of the western MC domain in MC2, and 72% of its land area, has $r > 0.75$. In MC12, only 18% of the western MC domain, and scarcely 5% of its land area, has $r > 0.75$ (Figure 3.9b). 39% of MC12 land area has a negative correlation with the DC of IMERG; there is a clear divide in correlation between high topography (positive correlation) and lowland areas (negative correlation). Over near-coastal waters, MC12 correlates with IMERG similarly strongly as does MC2. Far offshore, areas of both positive and negative correlation are observed in both models, but the correlations and anti-correlations tend to be stronger in MC12.

This correlation analysis was extended into a lagged correlation analysis by temporally rolling the model DC by multiples of 30 minutes and recalculating the correlation at each multiple to determine how far temporally offset the model DC is from its optimal correlation with the DC of IMERG. The optimal correlation of the DC in MC2 tends to be very close to the true correlation, especially over land where only 30% of land area is over one hour offset, with a slight tendency for the model DC to lag behind that of IMERG over near-coastal waters by 0–2 hours (Figure 3.9e). Since most areas are already close to their optimal correlation, the optimised r-value is generally little higher than the true r-value (Figure 3.9c). In contrast, MC12 shows widespread improvement in correlation strength when the model DC is shifted forward in time by some hours (indicated by blue colours in Figure 3.9f). When optimally aligned, 70% of the western MC domain, and 62% of its land area, has $r > 0.75$ (Figure 3.9d). However, certain lowland areas remain over Sumatra and Borneo where the DC of MC12 has a fundamentally different nature to the DC in IMERG, therefore

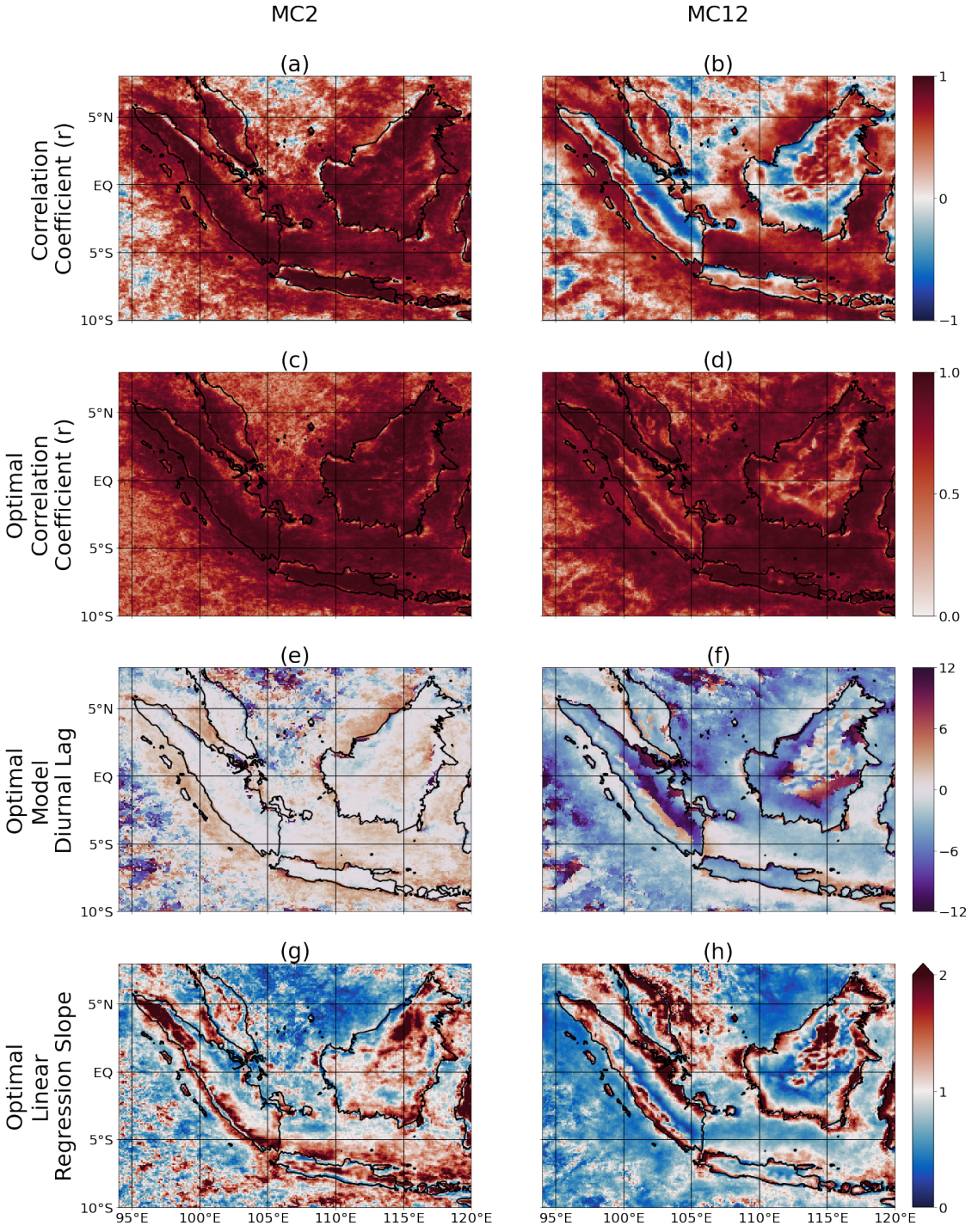

Figure 3.9: Metrics describing the linear correlation of the DC of precipitation in each model against the DC in IMERG. Left column relates to MC2 and right column relates to MC12. Top row shows the Pearson correlation coefficient, second row shows the Pearson correlation coefficient when the model DC has been temporally offset to its optimal alignment with IMERG, third row shows the temporal offset of the model DC relative to its optimal alignment, and the bottom row shows the linear regression slope for the optimally aligned correlation.

the correlation is weak with any amount of model offset. In far offshore areas of MC12 and MC2, weak optimised correlation is more likely to be a result of a weak diurnal signal in both or either of the modelled and observed DCs. Reassuringly, but perhaps unsurprisingly, the optimal model diurnal lag (Figure 3.9e&f) strongly resembles the measures of phase bias presented earlier in this section (Figures 3.3c&e and 3.6), particularly the phase bias quantified by the FDH and the best-fit spike-permitting waveform.

While the *r*-value informs on the accuracy of the timing of the modelled DCs, it does not inform on whether the magnitude of diurnal variability matches that of the DC in IMERG. The gradient of the optimally aligned linear regression is an indicator of the relative magnitudes of diurnal variability, where a gradient of one indicates equal magnitudes of diurnal variability, more than one indicates that diurnal variability in the model is too strong, and less than one indicates that diurnal variability in the model is too weak. In MC2, the optimally aligned linear regression gradient greatly exceeds one over high topography land area and in the near-coastal seas around Java, and it is below one across the South China Sea and in some lowland parts of Sumatra and Borneo (Figure 3.9g). In MC12, the linear regression gradient strongly exceeds one in the immediate vicinity of topographic peaks and coastlines, and much of the western South China Sea, and it is substantially below one across lowland areas, Java and most seas and ocean area (Figure 3.9h). These gradient distributions correspond well to the measures of amplitude bias discussed earlier (Figures 3.2c&e and 3.5), however there is some tendency for the linear regression gradient to indicate weaker model diurnal variability than the amplitude bias metrics. For instance, the MC2 model bias in half range is positive across most of the western MC domain, while the MC2 linear regression slope is widely around or below one. This discrepancy is likely to be due to the fact that high model diurnal variability will only result in a high linear regression gradient if the simulated DC has a similar nature to the observed DC nature, such that it projects onto it.

3.4 Discussion

These results have presented the characteristics of the boreal winter (DJF) composite DC of precipitation across the western MC simulated by convection-parametrised (MC12) and convection-permitting (MC2) configurations of the MetUM, and these cycles have been compared with a satellite-derived precipitation data product

(IMERG). MC12 simulates diurnal activity much too early (typically around three hours) across both land and water, while MC2 simulates diurnal activity at very close to the right time over land, and only slightly late over near-coastal seas. This contrast in DC phase simulation skill is in keeping with other studies of convection-parametrised and convection-permitting models (e.g. Slingo et al., 2003; Baranowski et al., 2019; Argüeso et al., 2020). Interestingly, Argüeso et al. (2020) found that the slight late bias over water in their 2 km model experiment was corrected when a deep convection parameterisation scheme was incorporated at the same resolution. It has also been suggested that the time of day at which deep convection initiates over land is influenced by whether a valley breeze, associated with steep gradients in topography, develops before the sea breeze arrives from the closest coastline (Wei et al., 2020). The early onset of precipitation over land in MC12 and the fixation of the strongest diurnal variability over high topography suggest that steep topography is too readily able to induce a valley breeze and trigger parametrised deep convection.

MC12 features some locations with extreme diurnal variability; a maximum half range of over 3.5 mm hr^{-1} was simulated at 2.95°N, 114.65°E (Figure 3.2e). In combination with the positive bias of the simulated spike parameter in this area (Figure 3.8e), it is strongly suggested that there is little day-to-day variability in the manifestation of the DC in MC12, at least in high topography areas. Over most near-coastal waters of MC12 where the simulated spike parameter is too low/negative, it is less straightforward to intuit whether this difference is due to higher day-to-day variability or due to longer-lasting overnight precipitation without investigating the variability in precipitation between individual days, such as with the event-based analysis used for observed variability in Section 2.7.2. The observed strong and invariable DC over Java noted in the previous chapter was suggested to induce a gravity wave that strongly inhibits precipitation over the Java Sea for a brief period of the early evening, leading to a strong but brief negative perturbation to the precipitation cycle and a negative spike DC over the Java Sea (Figure 3.8f). This dynamic may be weaker in MC12 as a result of the low amplitude of the simulated DC over Java, and be responsible for the positive model bias in spike in this area.

Both MC12 and MC2 simulate a negative model bias in skew, particularly over coastal waters (Figure 3.7c&e). This suggests that the mean weakening of precipitation in the composite is too rapid in both models, relative to the rate of intensification. This may be due to excessive day-to-day variability in the timing of precipitation initiation, too much day-to-day consistency in the timing

of precipitation termination, or different typical evolution of precipitation events such that individual precipitation events take longer to intensify in the models. While an event-based analysis (see Section 2.7.2) has not been performed on MC12 or MC2 to help constrain the interpretation of the negative model bias in skew, the lack of non-diurnal noise in MC12 (as inferred by the low wave index; Figure 3.4b) is suggestive of high day-to-day consistency in the manifestation of the DC. It is likely that both the precipitation initiation and termination occur at a consistent time day-to-day in MC12, but that the precipitation maximum occurs later on in the precipitation event than it does in IMERG. In contrast, MC2 exhibits substantial non-diurnal noise (Figure 3.4a), which is suggestive of high day-to-day variability in the manifestation and timing of diurnal precipitation. As such, it is suggested that the timing of diurnal precipitation initiation may be too variable in MC2, leading to a more gradual apparent intensification (and less positive skew) in the composite, though the rate of intensification on any individual day may be more accurate.

In Section 2.7.2, offshore negative skew was hypothesised to relate to the great span of time between arrival of a fast-propagating gravity wave (at which time composite precipitation may being to intensify) and the arrival of the slow-propagating density current (around which time maximum precipitation occurs). If the negative skew over near-coastal waters in the models is viewed in this dynamical framework, one possible explanation for the negative model bias in skew is that a modelled offshore-propagating gravity wave is triggered too early relative to the density current. This explanation makes a large assumption that gravity waves and density currents are simulated with reasonable accuracy, however the poor simulation of offshore phase propagation suggests significant deficiencies in model representation of either or both of these propagation mechanisms. Additional model fields, particularly the wind components, should be considered in order to better diagnose model representation of these propagation mechanisms.

As shown above, both the skew-permitting and spike-permitting waveforms offer useful quantification of the nature of the diurnal oscillation in precipitation and its comparison to the observed nature, with particular value in certain locations. The spike-permitting waveform is especially valuable over high topography — its parameters demonstrate that the DC has too brief, as well as too strong, a maximum. In contrast, the skew-permitting waveform is especially valuable over near-coastal waters — the lower/more negative skew in both models suggests that the intensification of diurnal precipitation is too gradual.

These insights into the nature of the DC can be used to constrain understanding of the processes operating in the models — such as the positive spike bias over high topography in MC12 suggesting more consistent and/or briefer diurnal activity — however, further analysis is required to confidently diagnose model processes.

It has been shown that comparison of the DC in models and in observations may be coloured by the choice of characteristic upon which comparisons are made. For example, in this study, it was found that MC2 simulates a half range that is 34% too strong across the western MC region, while the three best-fit waveforms produce an amplitude averaging between 19–23% too strong compared with their counterparts in IMERG. As such, interpretation of the magnitude of the DC drawn from the half range characteristic is strongly suggestive of over-exaggerated diurnal dynamics in MC2. However, interpretation of the magnitude of the DC drawn from a best-fit waveform amplitude is more in line with the magnitude of the model wet bias (17% across the western MC region), and therefore is not suggestive of strongly exaggerated diurnal dynamics in MC2.

MC12 typically simulates diurnal precipitation in both the late morning and late evening across non-coastal lowland areas, in stark contrast to the observed DC in most locations where there is only an evening peak. In such areas, problems in the simulation of diurnal variability cannot be solved by shifting the modelled cycle backwards or forwards in time. However, in many other areas, the correlation of the modelled DC with the observed DC can become strong simply by temporally shifting the modelled DC, suggesting that the timing of diurnal activity in MC12 is the dominant problem in these areas. The comparatively strong simulation of the phase of the DC by MC2 means that there is not as much scope to widely improve the simulation by temporally shifting the modelled DC, therefore the dominant problems with the MC2 DC are its amplitude distribution and its nature.

Both models simulate highly excessive diurnal variability in precipitation over high topography, at least over Sumatra and Borneo, at the expense of diurnal variability in precipitation in lowland areas. This is a common issue in convection-parametrised models, where parametrised deep convection is triggered too readily by valley breeze dynamics over steep model terrain, however the MC2 model suite highlights that this issue is not entirely attributable to problems with the convection parametrisation. MC12 also simulates excessive diurnal variability in precipitation in the immediate vicinity

of coastlines, where both the land and marine diurnal regimes extend all the way to the coastline with negligible amplitude decay, while the observed DC around coastlines has a much lower amplitude due to a broader coastal boundary region separating the diurnal regimes of land and water. MC2 improves on the performance of MC12 in some coastal areas, but the correlation with the observed DC remains weak around other coastlines, including much of northern and western Borneo.

This analysis has demonstrated the considerable difference in DC simulation skill between a convection-parametrised and a convection-permitting model configuration. Large biases in phase representation are to be expected in a parametrised model, particularly over land, while a convection-permitting model is able to simulate the DC of precipitation with high accuracy over land and moderate accuracy over coastal waters. Amplitude representation is also more accurate in the convection-permitting model in spite of excessive diurnal variability over high topography. The convection-permitting model, coupled to a model ocean, has been demonstrated to capture the main features of the DC of precipitation with high accuracy, though further work might consider the model representation of nocturnal offshore propagation of precipitation and its contributing mechanisms in closer detail. The accurate simulation of the DC in a convection-permitting simulation with a relatively broad regional domain and across several seasons strongly evidences the capacity of convection-permitting models to generate accurate diurnal variability internally, and not merely as an artifact of the diurnal signal fed in through lateral boundary conditions or through the ocean surface mixed layer in an atmosphere-only model.

Chapter 4

Modulation of the observed diurnal cycle of precipitation over the Maritime Continent by the Madden-Julian Oscillation

4.1 Introduction

In Chapter 2, the DC was established as a dominant mode of variability for observed precipitation across the MC, with increasingly well-resolved spatiotemporal complexities, and in Chapter 3 the skill of the MetUM at simulating the key features of the observed DC of precipitation was analysed. It was demonstrated that the nature of the DC is simulated well by the MetUM when configured at a sufficiently high resolution to explicitly resolve deep convective processes, while the DC simulated by a convection-parametrised configuration of the MetUM featured considerable contrasts with the observed DC of precipitation. At present, it is far too computationally intensive to run operational global weather forecasting models at a convection-permitting resolution, therefore the representation of the DC over the MC in such global forecasts is unreliable. As such, global weather forecasts are susceptible to degradation from the systematic errors in DC simulation over the MC.

Weather conditions over the MC are known to influence global weather at the medium range, particularly across North America and Europe (e.g. Neale & Slingo, 2003; Cassou, 2008). A key teleconnection mechanism is the triggering of

subtropical Rossby waves by the MJO; for example, Skinner et al. (2022) evidence a strong link between MJO phase 6 (as defined by the Real-time Multivariate MJO (RMM) index; Wheeler & Hendon, 2004) and the negative North Atlantic Oscillation (NAO-) weather regime, with a lag of order 10-15 days. In a typical MJO event where enhanced convection develops over the Indian Ocean, the region of enhanced convection must propagate eastward across the MC before it reaches the western Pacific Ocean, which is where the MJO active envelope is typically centred in MJO phase 6. The convective signature of the MJO has been shown to interact strongly with that of the DC as it passes over the MC (between MJO phases 3 and 5), with the MJO being frequently weakened or entirely blocked by the MC (e.g. Rui & Wang, 1990; Hendon & Salby, 1994; Hsu & Lee, 2005; Kim et al., 2014; Zhang & Ling, 2017). This series of interactions suggests that the signature of the DC over the MC has a systematic downstream impact on global weather at the medium range, and by extension, that errors in the simulation of the MC DC in convection-parametrised weather models are likely to degrade the quality of global weather forecasts. The strength of the interaction between the MC DC and the MJO dictates the potential severity of the anticipated medium-range weather forecast degradation by the subtropical Rossby wave teleconnection mechanism.

The scale interactions of the DC and the MJO have been the subject of a range of past studies. It is widely acknowledged that the amplitude of the DC over the islands of the MC strongly varies through the MJO cycle (e.g. Peatman et al., 2014), although there is not a strong consensus on the spatial pattern of lag (or absence thereof) between the MJO cycles of mean precipitation and DC amplitude, nor is there a strong consensus on the extent to which the MJO modulates the amplitude of the DC over water. There is also poor consensus on the influence of the MJO on the timing of the DC (note that, in this chapter, the quantity described as the "phase" of the DC is instead, but equivalently, described as the "timing" to reduce potential confusion with the phase of the MJO). Some studies have found no remarkable differences in the timing of the DC of deep convection between the MJO phases (Tian et al., 2006; Suzuki, 2009; Lu et al., 2019), while other studies have demonstrated the ability of the MJO to influence the timing of the DCs of precipitation and convection (e.g. Rauniyar & Walsh, 2011; Oh et al., 2012; Sakaeda et al., 2017; Wei et al., 2020).

In this chapter, the downscale influence of the MJO on the DC is investigated by characterising the composite DC for each of the eight phases of the MJO, as defined by Wheeler & Hendon (2004), and further characterising the strength

and nature of any variability in the DC characteristics across the MJO cycle. Many previous studies investigating this downscale influence have tended to consider the response of land and sea as a whole to the MJO cycle, preventing assessment of the detailed spatial variability of the scale interaction. Peatman et al. (2014) was an exception, however their analysis was across the entire MC region and discussion focused on the large-scale patterns, and did not consider variability of the DC timing due to the insufficient temporal resolution of the TRMM data product. Discussion in this chapter focuses on a smaller region of the western MC for clearer resolution of fine-scale spatial variability in the nature of the scale interaction, and presents a clear assessment of the spatial pattern of MJO-induced variability of DC timing. The results of this study will provide a detailed benchmark for the observed downscale influence of the MJO on the DC of precipitation across the western MC, against which the nature of the equivalent scale interaction in model simulations may be compared.

The structure of the remainder of this chapter is as follows: Section 4.2 describes the DC compositing methodology and the MJO index used to diagnose the state of the MJO. Section 4.3 presents analysis of the MJO cycles of mean precipitation, DC amplitude, DC timing, DC skew and DC spike, and Section 4.4 discusses the nature of DC variability across the MJO cycle, the strength of variability in different parts of the MC, and the likely physical processes leading to variability in the observed DC.

4.2 Data and Methods

As in the prior chapters, satellite-derived precipitation is sourced from IMERG. The real-time multivariate MJO (RMM) index (Wheeler & Hendon, 2004) is used to quantify the phase of the MJO. In order to consider the influence of each phase of the MJO on the DC, a composite DC of precipitation was calculated for each of the eight MJO phases using the days when the RMM index reports an amplitude of at least 1.0. Using IMERG data from each DJF season between and including January 2001 and January 2021 (the same data span as was used in Chapter 2 plus the month of January 2021), each of the eight composite DCs incorporates at least 74 days (and up to 244 days), which proves to be easily sufficient to isolate the influence of the MJO.

The RMM index is perhaps the most widely used metric to quantify the phase of the MJO, hence its use here allows for direct comparison with

many other studies on the interaction of the MJO with the DC. This index considers both dynamical (200-hPa zonal wind and 850-hPa zonal wind) and thermodynamical (outgoing long-wave radiation; OLR) parameter fields in its diagnosis of MJO activity. Several alternative MJO indices have been developed in the years since the RMM index was developed, featuring subtle differences in the methodology and the weighting of dynamical/thermodynamical parameter fields used to diagnose MJO activity. The analysis presented in this chapter has also been carried out after classifying the days by the OLR-based MJO index (OMI; Kiladis et al., 2014), another popular MJO index, to help ensure that any conclusions drawn are robust across MJO indices. The RMM index presents the MJO in integer phases from one to eight, according to the two leading principal components (PCs). Kiladis et al. (2014) show that RMM PC1 is analogous to OMI PC2, and RMM PC2 is analogous to $-1\times$OMI PC1, therefore these substitutions may be used to express the OMI MJO phase on the same 1–8 scale as RMM. For brevity, results based on the RMM index are presented, and the strongest contrasts based on the OMI are briefly discussed in Section 4.3.5.

As was thoroughly discussed in Chapter 2, there are a range of ways to characterise a cycle, and this issue presents itself again in the characterisation of the variability of any DC parameter across an MJO cycle. The amplitude of the MJO cycle (A_{MJO}) is measured in the units of the DC parameter that it is measuring, while the phase of the MJO cycle (ϕ_{MJO}) quantifies the phase of the MJO cycle when the DC parameter is most positive, with the exception of DC timing, for which ϕ_{MJO} quantifies the MJO phase when the DC timing is earliest. The different measures of MJO amplitude and phase are denoted with the following subscripts: bc for the basic characteristics (Section 2.4), fh for the first MJO harmonic (analogous to the first diurnal harmonic (FDH); Section 2.5.1), sk for the best-fit skew-permitting waveform (Section 2.6.1), and sp for the best-fit spike-permitting waveform (Section 2.6.2). The basic characteristic of MJO phase ($\phi_{MJO,\ bc}$) must be an integer from 1 to 8, while the other measures of MJO phase range continuously from 0.5 to 8.5. Use of the asymmetric waveforms for the characterisation of the MJO cycle of a DC parameter risks needlessly complicating the study with a phantasmagorical inception of waveforms! Therefore, presentation and discussion of the best-fit skew- and spike-permitting waveforms are restricted to when the skew (α_{MJO}) or spike (β_{MJO}) parameter of the MJO cycle has a magnitude greater than 0.3, such that there is a notable asymmetric component to the MJO cycle.

For calculations of an MJO cycle averaged over a given area, the mean of the

DC parameter of interest is calculated for each MJO phase, instead of calculating the mean DC across the area and then computing the DC parameter of interest from the spatially-averaged DC (i.e. mean of a parameter, not parameter of a mean). This approach allows for the spread of DC parameter values across the area in each MJO phase to be represented. The polar mean methodology described in Section 3.2.4 is used here for calculations of the area-averaged mean DC timing.

4.3 Results

4.3.1 Influence of the MJO on Mean Precipitation

Before considering the variability of the DC of precipitation across the MJO cycle, the context of mean precipitation variability across the MJO cycle should be considered. Across the western MC region, 65% of land area experiences maximum mean precipitation during either MJO phase 2 or 3, while 74% of marine area experiences maximum precipitation during either MJO phase 3 or 4 (Figure 4.1b). The MJO harmonic of mean precipitation over western MC land has a phase of 2.6 (Figure 4.1c), while the equivalent phase over western MC water is 3.4 (Figure 4.1d), indicating that the cycle of mean precipitation over land precedes that over water by nearly one MJO phase, or about one tenth of an MJO cycle.

The amplitude of the MJO cycle is stronger over water than over land, by the order of 50% (Figure 4.1a). The amplitude of the MJO harmonic of mean precipitation is 0.11 mm hr^{-1} for the land average, and 0.17 mm hr^{-1} for the marine average. On average across the western MC region, precipitation over land is stronger than over water, particularly during MJO phases 8 and 1, but mean precipitation over water becomes stronger than that over land during MJO phases 4 and 5.

There is subtle variability in the MJO cycle of mean precipitation between different bodies of land and water (Figure 4.1). While the amplitude and phase of the MJO cycle of mean precipitation is reasonably uniform across both Sumatra and Java, there is a clear regime divide between western and eastern Borneo, either side of approximately 115°E, with the MJO cycle over western Borneo being stronger and earlier in MJO phase. Considering western Borneo and eastern Borneo separately, all four averaged land regions experience a rapid

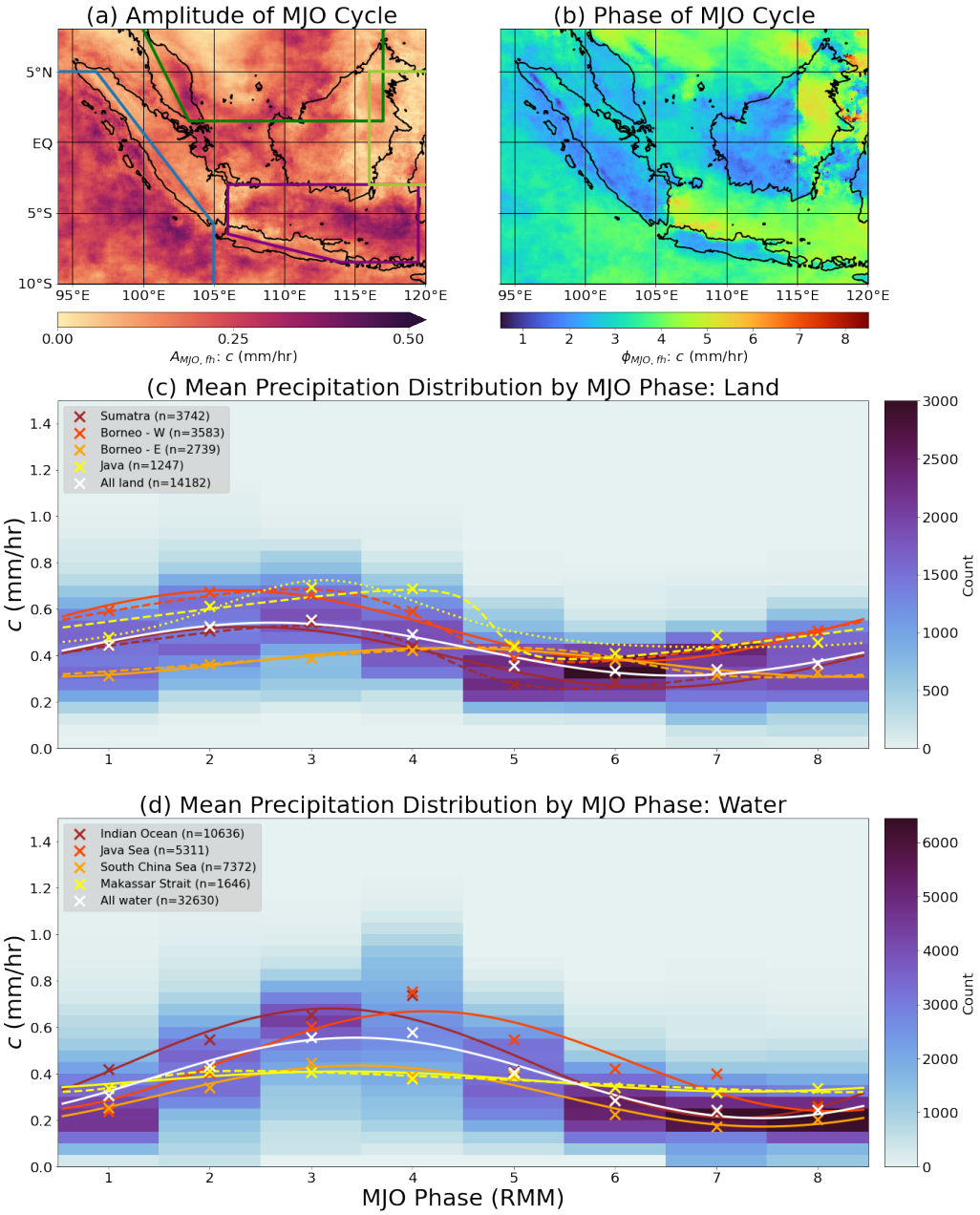

Figure 4.1: Variability of mean precipitation rate by MJO phase. (a&b) The amplitude and phase, respectively, of the MJO cycle variability in mean precipitation, quantified by the MJO harmonic. The blue, purple, dark green and lime green polygons outline the regions containing the waters defined as the Indian Ocean, the Java Sea, the South China Sea and the Makassar Strait, respectively. (c&d) Histograms of mean precipitation rate across the eight MJO phases over land and water, respectively. "Count" denotes the number of grid cells in a histogram bin. Crosses show the spatial mean precipitation against MJO phase for each region. Solid lines follow the MJO harmonic of each mean MJO cycle, while dashed and dotted lines follow the best-fit skew-permitting and best-fit spike-permitting waveforms for the mean MJO cycle, respectively. Only waveforms that sufficiently accurately characterise the MJO cycle variability are shown ($\epsilon \leq 0.4$; Equation (2.2)). Asymmetric waveforms are only presented if the magnitude of the asymmetry parameter exceeds 0.3.

weakening of mean precipitation following their respective local maximum, meaning that the MJO cycle may be described well using the skew-permitting waveform with negative skew parameter (dashed lines in Figure 4.1c). For Java, the strength of this asymmetry ($\alpha_{MJO} = -0.66$) results in the MJO phase of maximum mean precipitation being one MJO phase later based on the best-fit skew-permitting waveform than based on the MJO harmonic ($\phi_{MJO,\ sk} = 4.0$, $\phi_{MJO,\ fh} = 3.0$). α_{MJO} ranges from -0.38 to -0.34 for the other averaged land regions. The MJO phase of the best-fit skew-permitting waveform spans from 2.9 over western Borneo, through 3.0 over Sumatra and 4.0 over Java, to 4.8 over eastern Borneo. Although the MJO phases of maximum mean precipitation either side of Borneo are only a quarter of an MJO cycle apart, the rapid weakening means that minimum mean precipitation over western Borneo occurs very shortly after maximum mean precipitation over eastern Borneo. While Sumatra, Java and western Borneo all have MJO cycle amplitudes between 0.13 mm hr^{-1} and 0.16 mm hr^{-1}, eastern Borneo experiences a much weaker MJO cycle in mean precipitation with an amplitude of approximately 0.06 mm hr^{-1}.

Over water, MJO phase 4 is the dominant phase for maximum mean precipitation south of 2°S across the western MC region's span of longitudes. There is more regional variability further north, with maxima mostly between MJO phases 2 and 5 (Figure 4.1b). The major water bodies within the western MC region — the Indian Ocean, the South China Sea, the Java Sea and the Makassar Strait (outlined in Figure 4.1a) — show composite MJO phases ($\phi_{MJO,\ fh}$) of 3.2, 3.5, 4.1 and 3.3, respectively, for maximum mean precipitation. Unlike for the land regions, no strong systematic asymmetry in the MJO cycle of mean precipitation is found for any of these water bodies, with the exception of the Makassar Strait where the amplitude of the MJO cycle is very low. Between the equator and 2°S, between Sumatra and the Mentawi islands and also between Borneo and Sulawesi, the MJO phase of maximum mean precipitation is considerably earlier than over surrounding waters.

4.3.2 Influence of the MJO on the Amplitude of the Diurnal Cycle

Unless otherwise stated, results in this subsection focus on the MJO harmonic measure of the DC half range; the MJO harmonic provides good spatial coherence and the DC half range ensures an accurate measure of diurnal

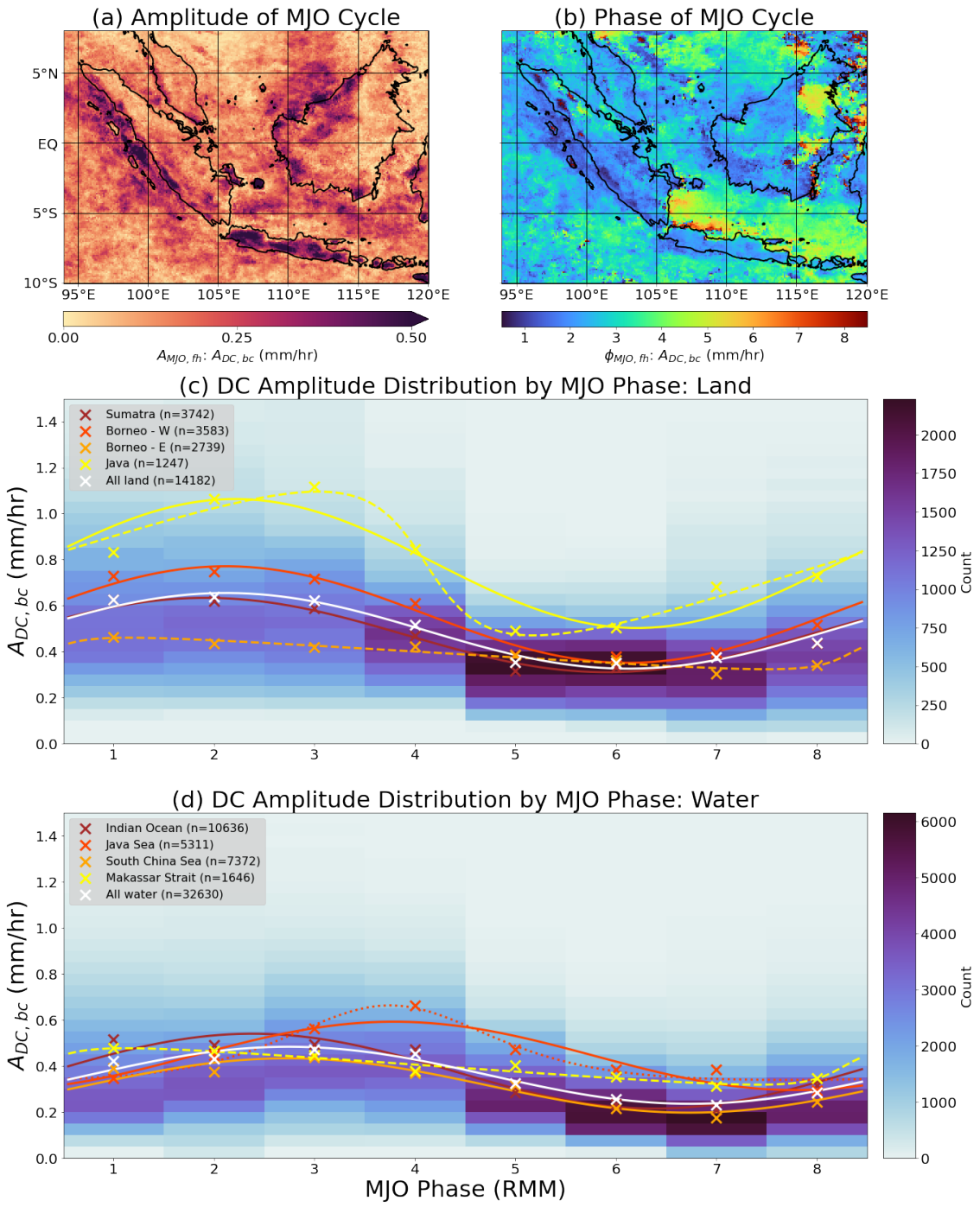

Figure 4.2: As for Figure 4.1, but for the half range measure of DC amplitude.

activity even in locations where waveforms fail to characterise diurnal variability well. The MJO harmonic phase of the mean DC amplitude over land is 2.1 (Figure 4.2c), and over water the equivalent MJO harmonic phase is 2.7 (Figure 4.2d). These MJO harmonic phases are slightly earlier than the corresponding phases for the cycle of mean precipitation, and indeed the MJO cycle of DC amplitude precedes the MJO cycle of mean precipitation in most locations (Figure 4.3b). The MJO cycle of DC amplitude precedes the MJO cycle of mean precipitation over 86% of western MC marine area; the polar mean MJO phase lag over water is 0.54, meaning that the strongest diurnal activity precedes the strongest mean precipitation by approximately half an MJO phase in the average marine location. Correspondingly, 75% of western MC land area experiences its strongest diurnal variability in an MJO cycle in advance of the strongest mean precipitation, with a comparable polar mean MJO phase lag of 0.46. There is more regional variability over land than over water; parts of eastern Borneo experience the highest phase lags observed across the region, near-coastal land areas typically show only a slight MJO phase lag, tending toward being in phase or slight phase lead of the MJO cycle of mean precipitation further inland.

The MJO phase lag calculations are subtly dependent on the measure of DC amplitude considered. If a waveform amplitude is used to describe the DC instead of the half range, the polar mean MJO phase lag decreases to as low as 0.24 over land and 0.37 over water. In contrast, the lag calculations are not strongly dependent on the measure of MJO phase with which the MJO cycles of mean precipitation and of DC amplitude are compared.

The amplitude of the MJO harmonic of DC amplitude shows substantial regional variability. The strongest MJO cycles in DC amplitude are over Java, Indian Ocean waters close to the west Sumatra coast, parts of onshore and offshore northwest Borneo, some of the smaller islands, and the northern stretch of the Java Sea (Figure 4.2a). Weaker MJO cycles in DC amplitude are found over eastern Borneo, parts of north and east Sumatra, the southern stretch of the Java Sea, and the west South China Sea. Some of these areas of high and low variability of DC amplitude align with areas of high and low variability of mean precipitation (Figure 4.1a), however some areas, such as Java, experience a strong MJO cycle of DC amplitude in spite of a moderate MJO cycle of mean precipitation (Figure 4.4b). In general, land areas, especially over Java, high topography and small islands, experience a stronger MJO cycle in DC amplitude, while marine locations typically experience a stronger MJO cycle in mean precipitation, especially far offshore. The MJO harmonic amplitude of

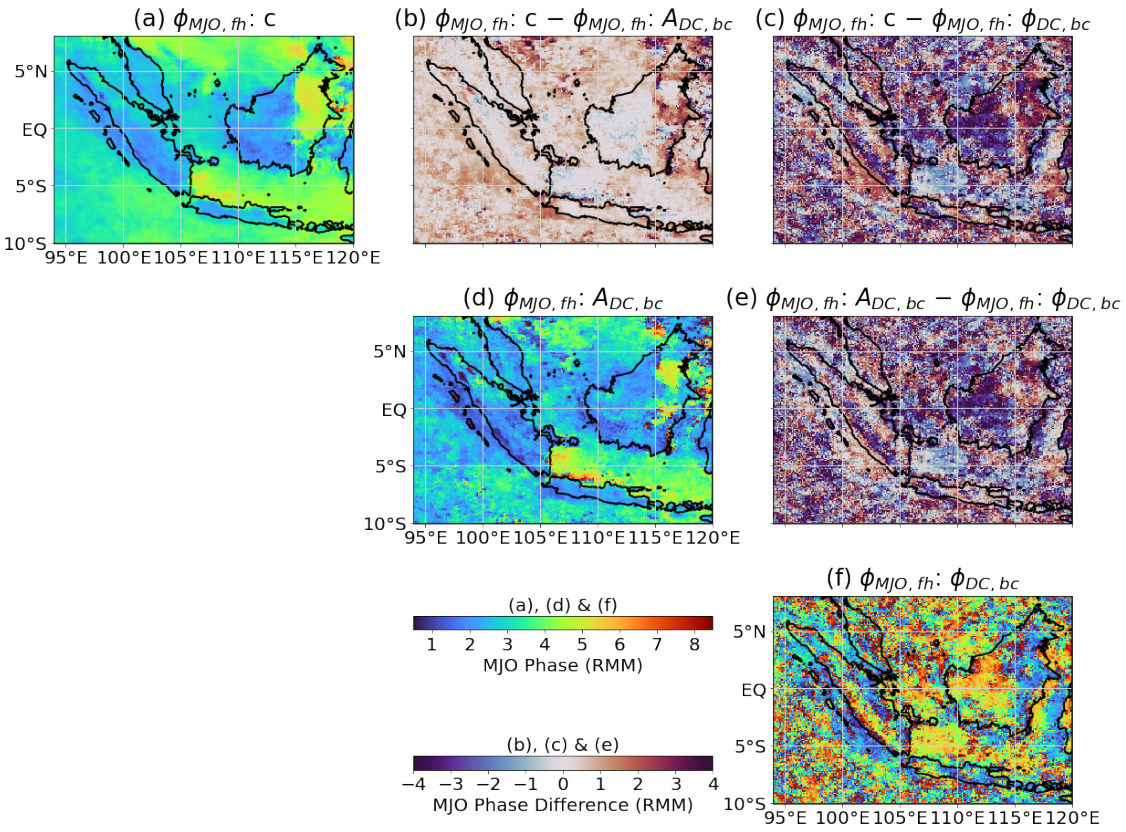

Figure 4.3: Comparison of the phase of the MJO cycles of mean precipitation, DC amplitude and DC timing. The leftmost panel in each row shows the MJO harmonic phase of the MJO cycle of (a) mean precipitation, (d) the DC half range, and (f) the DC peak time. Remaining panels (b,c,e) compare the MJO harmonic phases and show their phase lags.

the mean DC amplitude over land is 0.16 mm hr^{-1}, however the individual land regions have MJO harmonic amplitudes ranging from 0.06 mm hr^{-1} (eastern Borneo) to 0.28 (Java). Over water, the amplitude of the MJO cycle of mean DC amplitude (defined by the MJO harmonic) is 0.12 mm hr^{-1}, with the Indian Ocean and Java Sea areas both showing slightly above-average MJO harmonic amplitude.

There is a similar tendency toward negative skew of the MJO cycle of DC amplitude over land as was noted for the MJO cycle of mean precipitation over land. In particular, Java shows a rapid weakening of diurnal variability between MJO phases 3 and 5, with $\alpha_{MJO} = -0.51$; this is similar to the rapid weakening of mean precipitation over Java between MJO phases 4 and 5 ($\alpha_{MJO} = -0.66$). The Java Sea shows an especially high DC amplitude in MJO phase 4 (Figure 4.2d), which mirrors the high mean precipitation it also experiences in this MJO phase (Figure 4.1d).

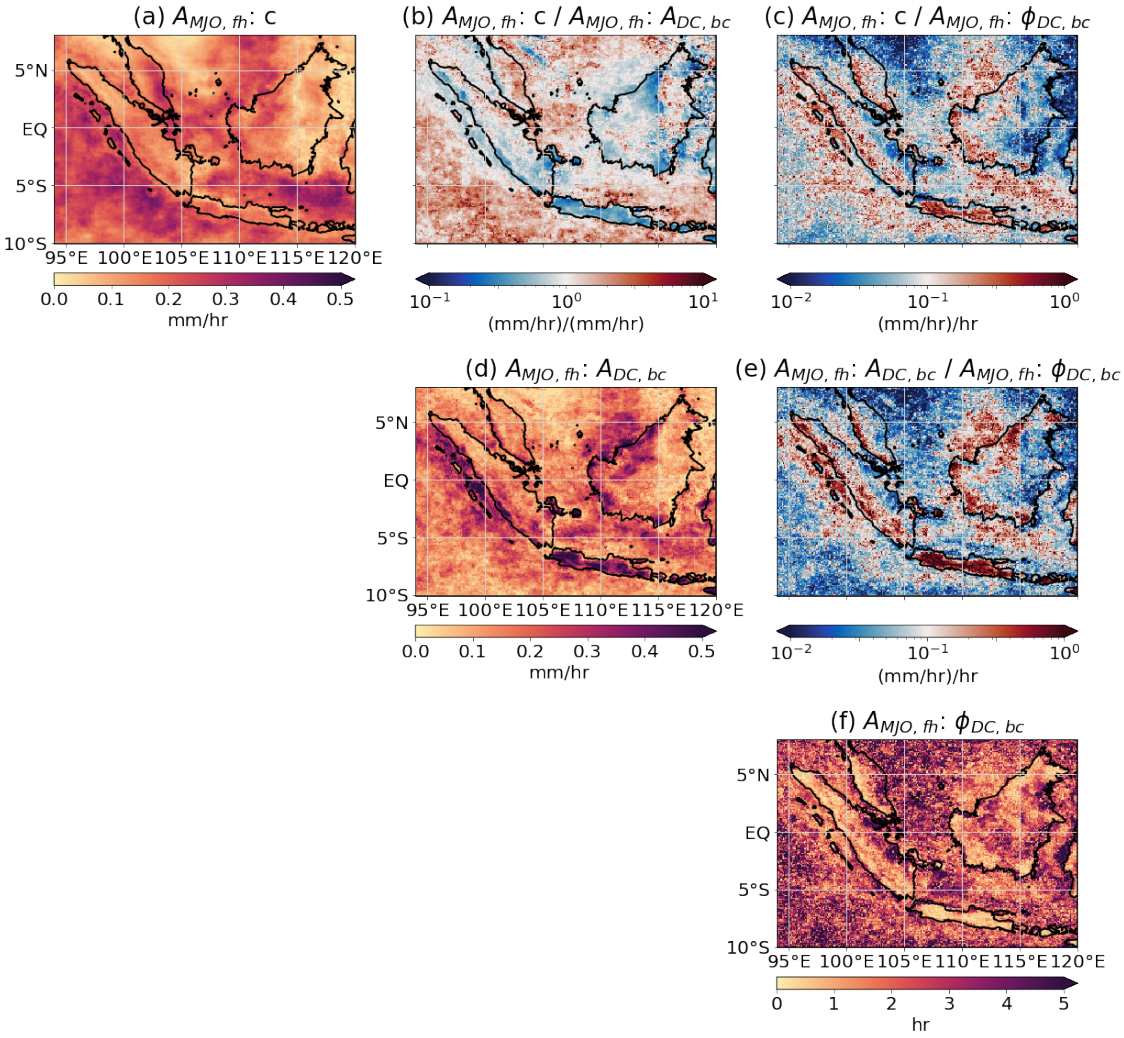

Figure 4.4: As for Figure 4.3, but for (a,d,f) MJO harmonic amplitudes, and (b,c,e) MJO harmonic amplitude ratios.

4.3.3 Influence of the MJO on the timing of the Diurnal Cycle

In keeping with Section 4.3.2, results in this subsection focus on the MJO harmonic measure of the DC peak time, where not otherwise stated. While dependence of the DC amplitude on the MJO phase is expected, it is not necessarily obvious that the MJO should influence the DC timing. Assuming that any variability of the DC timing with the MJO phase is subtle, the study of this relationship has only become possible with the advent of very high temporal resolution data sets such as IMERG. The MJO harmonic of DC peak time was calculated at each location in a similar manner as for DC half range, with two key differences. First, at each location, the DC peak times across the eight MJO phases were centred on the polar midpoint before the MJO harmonic was calculated, to avoid complications arising from the peak time varying either

side of local midnight at some locations. Second, the phase of the MJO harmonic marks the earliest DC peak time (relative to the polar midpoint across the eight MJO phases at a location), to mark the MJO phase when diurnal precipitation develops soonest.

One complicating factor affecting these results is that the DC timing is highly susceptible to noise where the DC is weak. As such, offshore areas, which are known to experience weak diurnal variability, often produce high MJO harmonic amplitude of DC timing (Figure 4.5a). It is, therefore, not straightforward to identify areas that experience a systematic MJO influence on DC timing based on the MJO harmonic amplitude alone. Spatial coherence of the MJO cycle phase helps to distinguish such areas. While the MJO harmonic phase of peak time is less spatially coherent than the MJO harmonic phase of either mean precipitation or DC half range (Figure 4.3f), areas of coherence exist across the west Java Sea (MJO phases 4–6), western and eastern Borneo (MJO phases 5–6 and 2–3, respectively), the Makassar Strait (MJO phases 5–6 and 2–3 along the west and east sides, respectively), western and eastern Sumatra (MJO phases 4–7 and 1–2), and Indian Ocean waters close to the southwest coast of Sumatra (MJO phases 1–2). Most of these locations have a consistently high MJO harmonic amplitude across the region. In contrast, many near-coastal land areas across the west side of the large islands have a small MJO harmonic amplitude.

Due to the substantial regional variability of the MJO cycle of DC timing, it is unsurprising that the MJO cycles of polar mean DC timing over land and over water are reasonably subtle. Over land, the MJO cycle of DC timing is well characterised by the best-fit skew-permitting waveform, which has an amplitude of 0.65 hr, a phase of 2.1 and a skew of -0.32 (white dashed line in Figure 4.5c). This characterises a change of slightly over one hour in the timing of peak diurnal precipitation over land across the MJO cycle, with an earliest polar mean peak time of 17.6 hr in MJO phase 2 and latest polar mean peak time of 19.2 hr in MJO phase 5. Both Sumatra and Java experience an MJO cycle in polar mean peak time with similar characteristics to the polar mean land cycle, albeit over one hour earlier in the day in the case of Java. The MJO cycle of DC timing over eastern Borneo has a similar phase ($\phi_{MJO,sk} = 2.2$) and a similar negative skew ($\phi_{MJO,sk} = -0.38$), inferring rapid progression of DC timing to later in the evening following MJO phase 2. However, eastern Borneo shows a much more pronounced MJO cycle amplitude ($A_{MJO,sk} = 2.3$ hr), oscillating between a polar mean peak time of 16.1 hr in MJO phase 2 and 21.0 hr in MJO phase 5. The MJO cycle of DC timing over western Borneo is out of phase with the other land

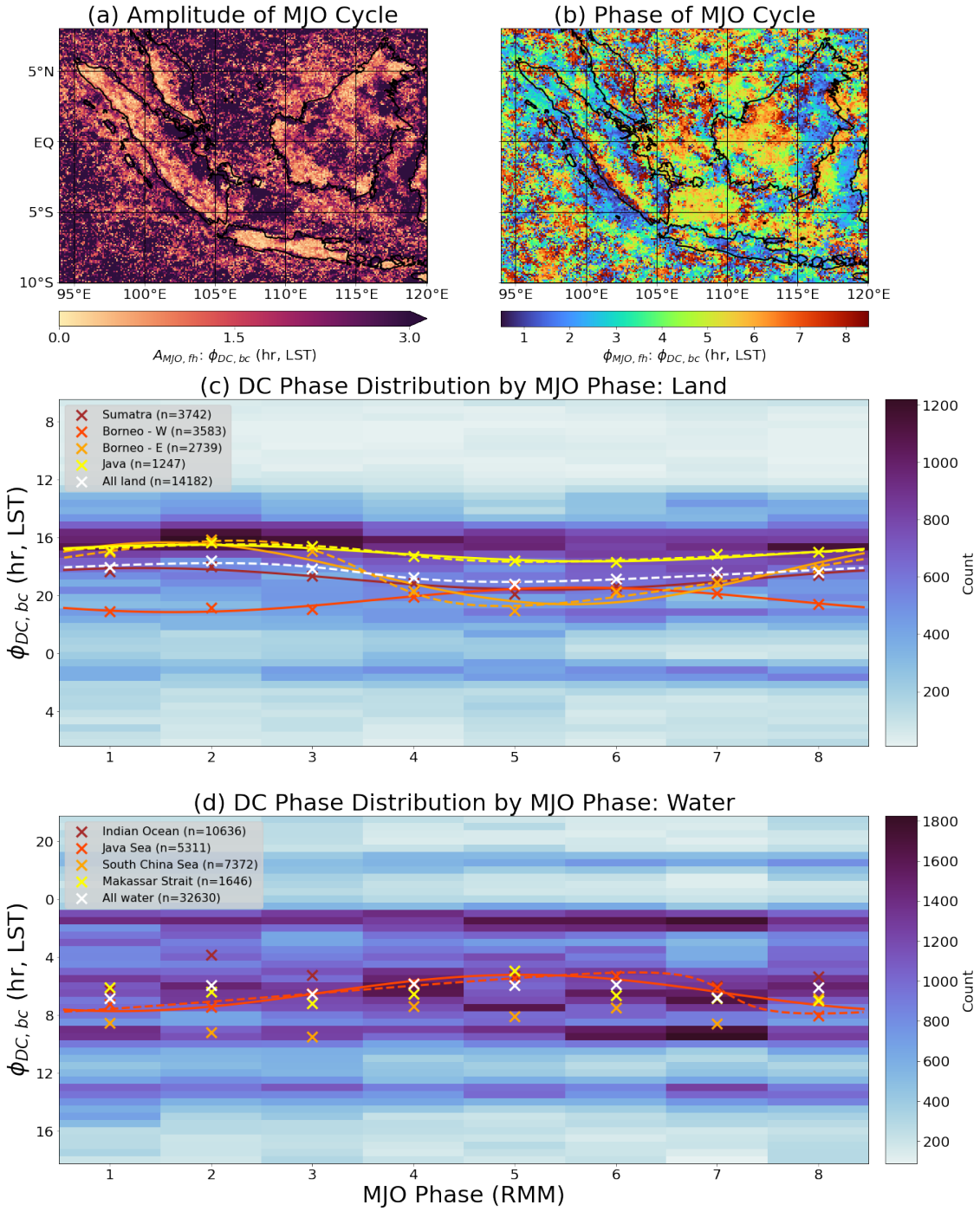

Figure 4.5: As for Figure 4.1, but for the peak time measure of DC timing. Crosses show the polar midpoint of the DC timing distribution for each MJO phase, and the vertical axis is set to centre on the polar midpoint of the eight all-encompassing MJO phase polar midpoints (white crosses). Time progresses downwards in panels (c&d).

regions considered; the earliest polar mean peak time (19.3 hr) occurs in MJO phase 5 while the latest polar mean peak time (21.1 hr) occurs in MJO phase 1. If, like for Sumatra and Java, the polar mean DC timing across all of Borneo is considered in each MJO phase, the strong but opposing variability in each of the two regimes approximately cancels out to produce a weak island-mean MJO cycle in DC timing, slightly favouring the eastern regime. Sumatra clearly shows the same west–east regime divide as Borneo, and to a lesser extent, there is evidence of longitudinal influence on MJO cycle phase of DC timing over Java (Figure 4.5b).

The MJO cycle of polar mean marine DC timing is very weak, as for land, and none of the single-peak waveforms sufficiently accurately characterise the weak variability that is observed (white crosses in Figure 4.5d). Polar mean marine peak time varies between 5.9 hr and 6.9 hr, but fluctuates noisily within this range through the MJO cycle. The Indian Ocean and South China Sea marine regions (outlined in Figure 4.1a) also fail to demonstrate a coherent single-peak oscillation in DC timing, although the variability in DC timing between MJO phases is stronger (varying by at least two hours in both regions). Due to the broad region of coherence across the western Java Sea, the Java Sea marine region shows a coherent MJO cycle in DC timing, best characterised by the best-fit skew-permitting waveform ($A_{MJO,sk} = 1.4$ hr, $\phi_{MJO,sk} = 6.2$, $\alpha_{MJO,sk} = -0.61$). The polar mean DC timing rapidly progresses from 5.3 hr in MJO phase 6 to 8.1 hr in MJO phase 8. The pattern of MJO harmonic phase of DC timing over the Java Sea resembles the pattern over Sumatra and Borneo in featuring earliest DC timing around MJO phase 5–6 across the western part of the region, however in contrast, there is not a coherent opposite MJO phase across the eastern part of the Java Sea marine region, and the western part shows stronger variability. This west–east phase regime is also mirrored over the Makassar Strait, however, the stronger MJO harmonic amplitude over the eastern part of the strait mirrors the regime over Sumatra and Borneo instead of that over the Java Sea.

The emerging pattern across most large land and sea bodies of the western MC region is that western parts of bodies experience a late DC and eastern parts of bodies experience an early DC while the MJO is active over the Indian Ocean (MJO phase 2), and this pattern reverses (often rapidly) as MJO activity crosses the MC into the western Pacific Ocean (MJO phase 5–6). The explicit variability of the DC timing, which shows an MJO cycle qualitatively consistent with the peak time metric while being more spatially coherent, emphasises westward

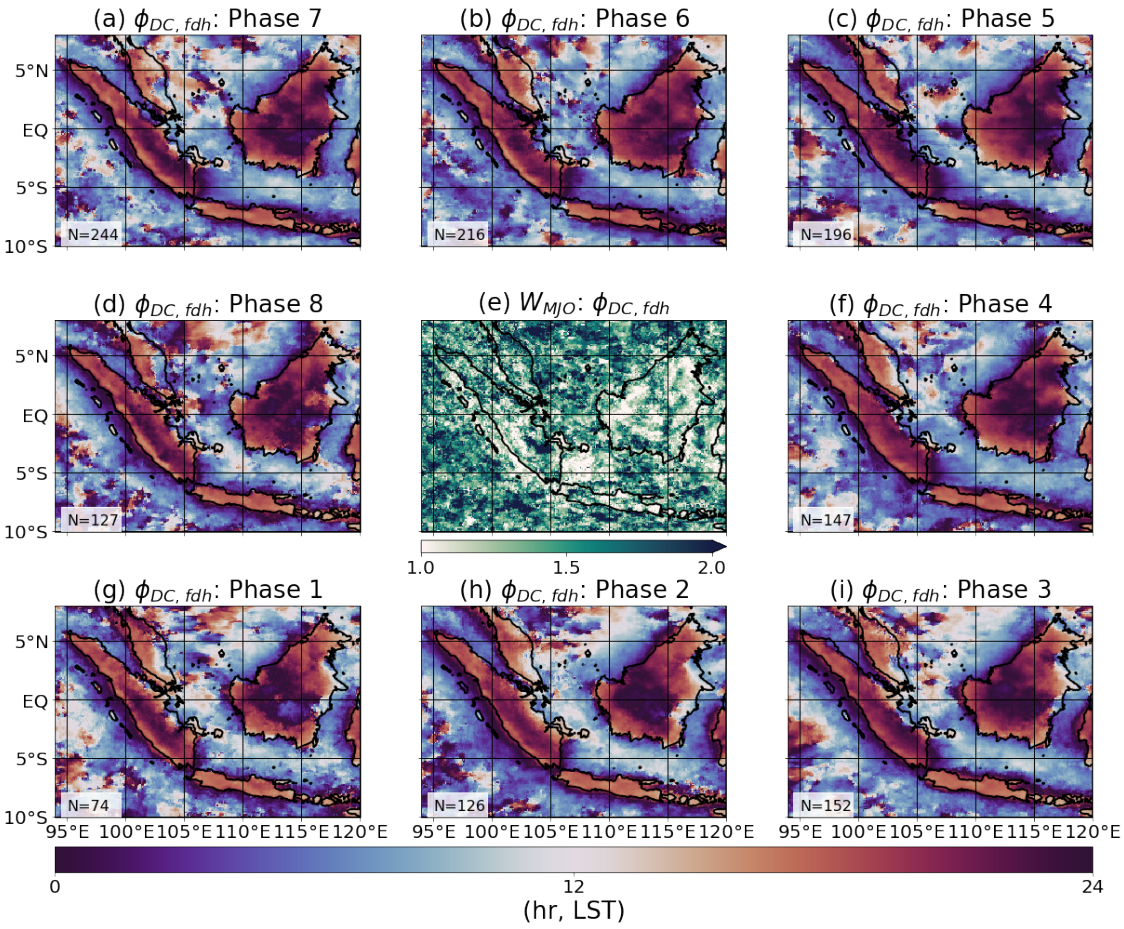

Figure 4.6: Explicit demonstration of the variability of DC timing through an MJO cycle. Outer panels show the DC timing according to the FDH, in LST, for each of the eight MJO phases, progressing anti-clockwise from Phase 1 in the bottom left panel (g). The number of days per composite is shown in the bottom left of each panel. Centre panel (e) shows the wave index associated with the MJO cycle of DC timing according to the FDH.

propagation patterns during MJO phase 2 (e.g. offshore from northwest and southwest Borneo and west Sulawesi, onshore from east Sumatra and east Borneo; Figure 4.6h) and eastward propagation patterns during MJO phase 5 (e.g. offshore from southeast Sumatra and east Borneo, and across the widths of Sumatra and Borneo; Figure 4.6c).

The relationship between the MJO harmonic phase of DC timing and the MJO harmonic phase of either mean precipitation or DC amplitude is complex. Over Borneo, the MJO harmonic phase of DC timing is far out of phase with the MJO harmonic phase of mean precipitation across both the western and eastern regions (Figure 4.3c), suggesting that the earliest diurnal precipitation maximum at any given location in Borneo occurs when mean precipitation is weak. This approximate phase opposition is also observed across much of western Sumatra

and western Java, while the majority of remaining areas that show a coherent phase lag show that the earliest DC occurs within two MJO phases of maximum mean precipitation. Eastern Sumatra, eastern Java and the area around and slightly offshore of the southern southwest Sumatra coast show a positive phase lag, meaning that the earliest DC timing precedes maximum mean precipitation. In contrast, the west Java Sea shows a slight negative phase lag and infers that maximum mean precipitation shortly precedes the earliest DC timing.

The ratios of the MJO harmonic amplitudes of mean precipitation and DC amplitude to the MJO harmonic amplitude of DC timing identify areas where variability of DC timing is the dominant impact of the MJO cycle. The lowest values of these ratios, which identify areas where the DC timing varies substantially despite limited change in mean precipitation or DC amplitude, are found across the Makassar Strait and the eastern parts of Sumatra and Borneo (and far offshore areas, however this is due to non-systematic variability of DC timing across the MJO cycle, i.e. noise).

4.3.4 Influence of the MJO on the Asymmetry Parameters of the Diurnal Cycle

As with the variability of DC timing across the MJO cycle, high variability of the DC asymmetry parameters — skew and spike — across the MJO cycle may either be due to a systematic DC interaction with the MJO or due to noise, since noise-dominated DCs often favour extreme values of skew and spike. The asymmetry parameters are most susceptible to noise-induced variability when the asymmetric waveform does not offer an accurate fit. Therefore, by hatching over areas of the map of skew where the best-fit skew-permitting waveform does not offer a sufficiently accurate characterisation according to $\epsilon \leq 0.4$ (Figure 4.7a&b), and likewise for the map of spike and the best-fit spike-permitting waveform (Figure 4.8a&b), much of the noise in the MJO cycles of skew and spike is masked. Hatching follows from that in Figure 2.5b&d, based on the DC across all MJO phases, not the scaled error for any of the eight MJO phase composites. It is important to note that, in order to exclude misrepresentative (often extreme) values of skew and spike, only non-hatched locations are incorporated into the calculations of areal-mean skew and spike by MJO phase (Figures 4.7c&d and 4.8c&d). The pattern of the MJO harmonic phase of DC skew is comparable to the MJO harmonic phase of DC timing (Figure 4.5b); areas including western Sumatra, western Borneo and the western

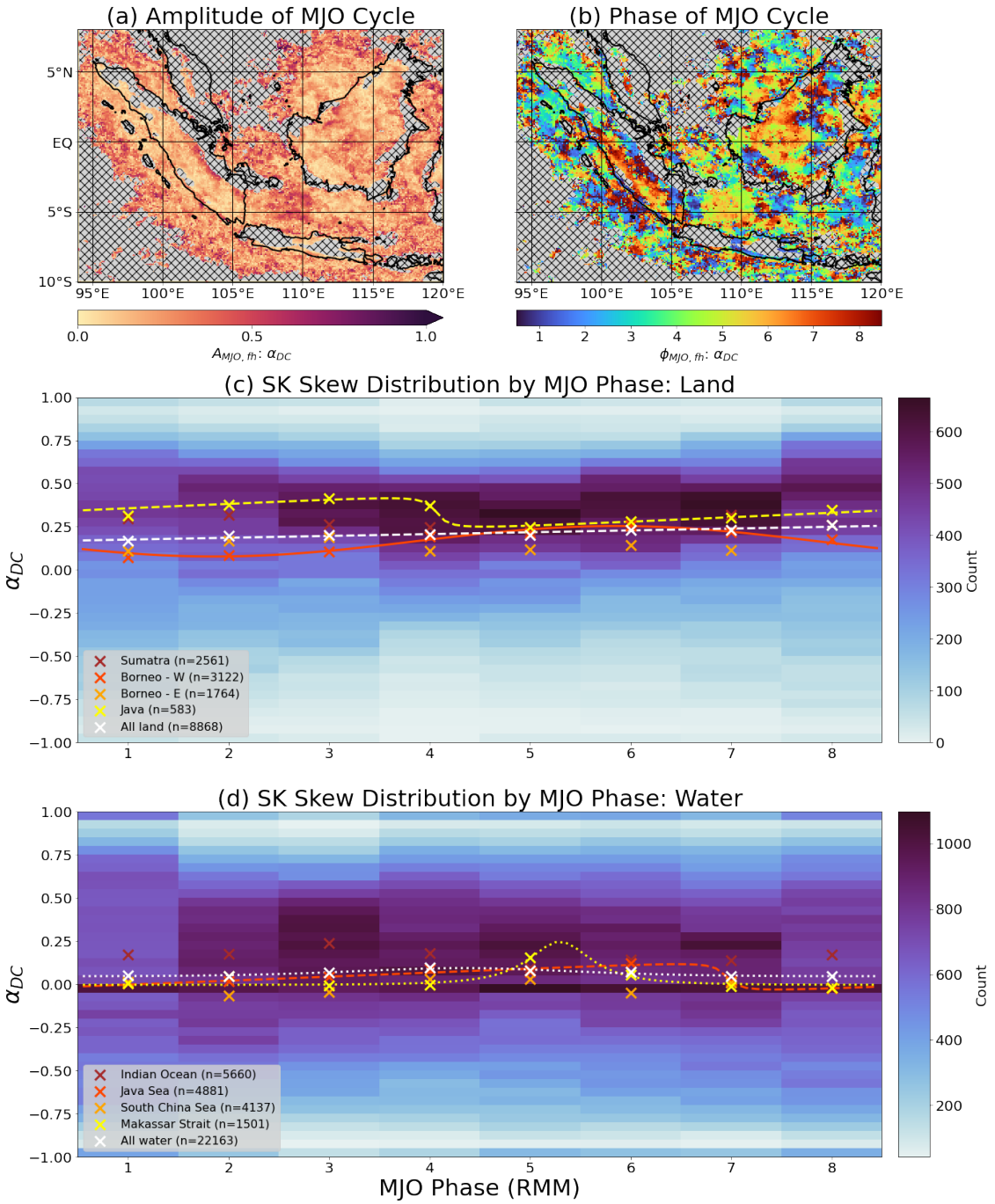

Figure 4.7: As for Figure 4.1, but for the DC skew parameter derived from the best-fit skew-permitting waveform. Hatching is applied in panels (a) and (b) where the best-fit skew-permitting waveform fails to sufficiently accurately characterise the mean DC, complementing Figure 2.5b. The crosses in panels (c) and (d) show the areal-mean skew values of only sufficiently accurately characterised locations.

Java Sea have MJO harmonic phases typically between MJO phases 4 and 7, with the western Java Sea in particular featuring a high MJO harmonic amplitude. In contrast, those eastern parts of land and water bodies that are sufficiently accurately characterised by the best-fit skew-permitting waveform have earlier MJO harmonic phases, typically between MJO phases 1 and 3. The comparison between the MJO harmonic phases of DC skew and DC timing means that maximum DC skew, and therefore the most rapid intensification of precipitation in the composite sense, approximately coincides with the earliest DC timing, as quantified by the peak time.

Averaging across all land area with a sufficiently accurate best-fit skew-permitting waveform characterisation, there is a subtle but coherent MJO cycle in DC skew, featuring a gradual increase in mean DC skew from 0.17 in MJO phase 1 to 0.26 in MJO phase 8 (Figure 4.7c), with a rapid decrease as the MJO cycle begins again. When key land regions are considered separately, western Borneo shows the strongest and most coherent variability, ranging from mean DC skew of 0.07 in MJO phase 1 to 0.26 in MJO phase 6. Similarly, considering the average across all marine area with a sufficiently accurate best-fit skew-permitting waveform characterisation, there is a very subtle but coherent MJO cycle in mean DC skew, ranging from a broad minimum of around 0.04–0.05 between MJO phases 7 and 2 to a maximum of 0.09 in MJO phase 4 (Figure 4.7d). The different marine regions demonstrate very distinct MJO cycles of DC skew; the Makassar Strait features especially positive DC skew in MJO phase 5, while the Java Sea shows a gradual increase in DC skew with a rapid decrease around MJO phase 7. Other regions, including Java, eastern Borneo, the Indian Ocean and the South China Sea, do not show a coherent single-peak MJO cycle of DC skew at the regional scale. In general, the distribution of DC skew values over land is most constrained between MJO phases 4 and 7, with more negative and extremely positive DC skew values outside of these MJO phases (Figure 4.7c). The spread of DC skew values over water is, similarly, lowest between MJO phases 2 and 7, though the contrast in spread between MJO phases is less strong than over land.

The MJO harmonic phase of DC spike also shows spatial coherence in selected regions (Figure 4.8b). While not very high anywhere, the highest MJO harmonic amplitudes are found across the Java Sea and over the Indian Ocean to the south and west of the Mentawi Islands (Figure 4.8a), and these locations show maximum DC spike typically between MJO phases 8 and 2. Some coherence of MJO harmonic phase is evident over land, such as across central

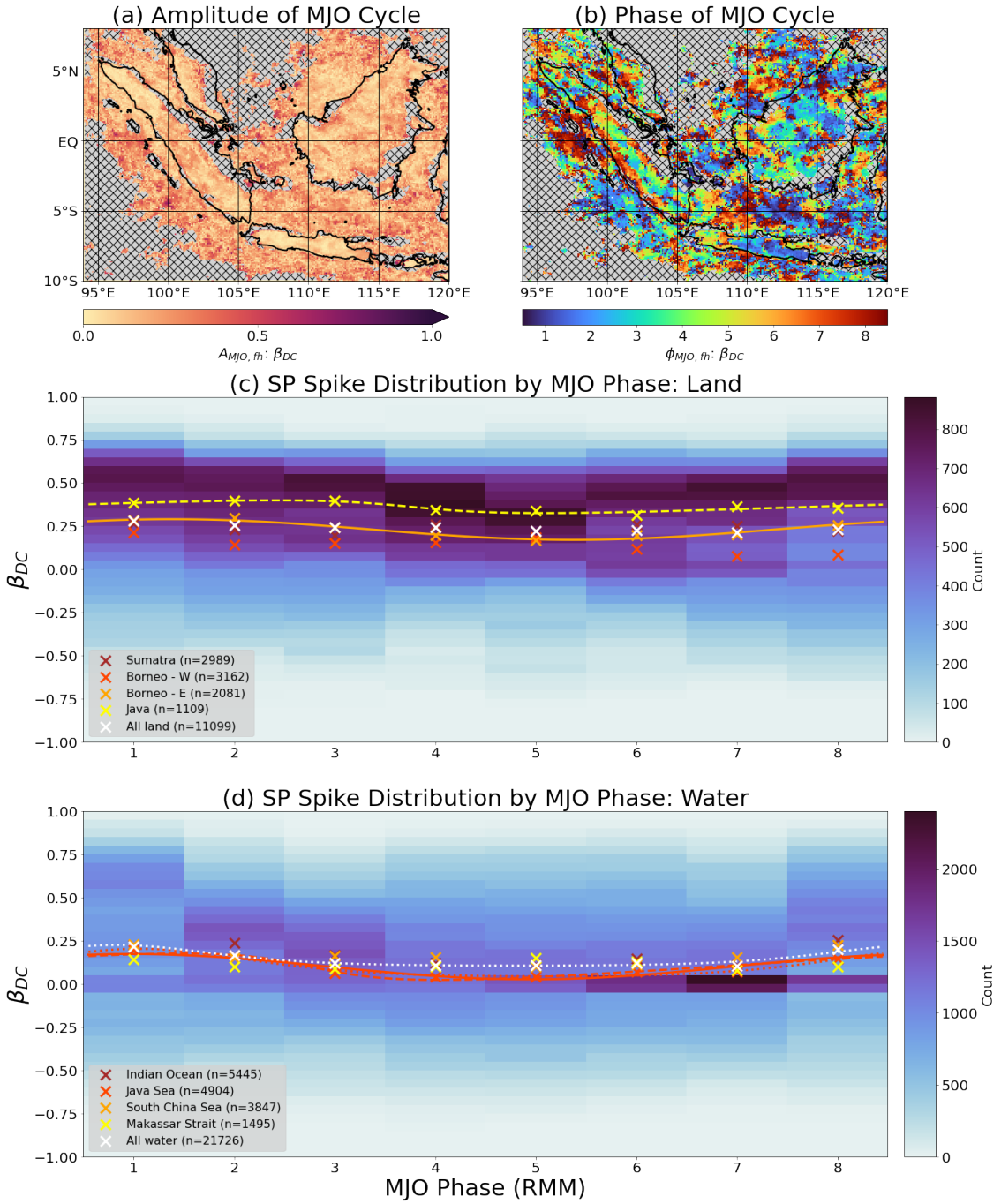

Figure 4.8: As for Figure 4.1, but for the DC spike parameter derived from the best-fit spike-permitting waveform. Hatching is applied in panels (a) and (b) where the best-fit spike-permitting waveform fails to sufficiently accurately characterise the mean DC, complementing figure 2.5d. The crosses in panels (c) and (d) show the areal-mean spike values of only sufficiently accurately characterised locations.

and eastern Java which has a typical MJO harmonic phase of approximately MJO phase 2, though different land areas vary greatly in MJO harmonic phase. There is no coherent single-peak land-averaged MJO cycle in DC spike (absence of white best-fit lines in Figure 4.8c), however at the regional level, both Java and eastern Borneo show a coherent MJO cycle. The strongest coherent regional MJO cycle of DC spike over land is over eastern Borneo, where DC spike ranges from a minimum of 0.17 in MJO phase 5 to a maximum of 0.30 in MJO phase 2. Over water, there is a coherent single-peak land-averaged MJO cycle in DC spike (white dotted line in Figure 4.8d), featuring a broad minimum mean DC spike of 0.11–0.12 from MJO phase 3 to 7 and a maximum mean DC spike of 0.22 in MJO phase 1. The only marine region to demonstrate a coherent single-peak MJO cycle of DC spike is the Java Sea, where mean DC spike ranges from 0.04 in MJO phases 4–5 to 0.20 in MJO phase 1. The MJO harmonic phase pattern of DC spike appears to show some coherence in the same regions as DC timing (Figure 4.5b) and DC skew (Figure 4.7b), but there does not appear to be a systematic correlation. Despite DC spike being intrinsically linked to DC amplitude (Figure 4.2b), there is no clear pattern of correlation between the MJO harmonic phase patterns of these two DC parameters either. Much like for DC skew, the distribution of DC spike values over land is most constrained around MJO phases 4 and 5, and over water, maximum spike between MJO phase 8 and 2 seems most common, but there is much spatial variability.

4.3.5 Sensitivity to MJO Index

Qualitatively, most of the results presented here are not strongly influenced by the choice of MJO index, particularly concerning the amplitude of the various MJO cycles. In some cases, moderate differences in the phase and skew of the MJO cycle are observed when the MJO phase is defined by the OMI instead of the RMM index. For conciseness, figures depicting the results based on the OMI are not presented, however, some of the greatest contrasts are mentioned here.

The mean MJO cycle of mean precipitation over water shows an MJO phase nearly half an MJO phase later using OMI ($\phi_{MJO,\ fh} = 3.8$) than when using RMM ($\phi_{MJO,\ fh} = 3.4$). In contrast, the MJO phase over land varies by less than one tenth of an MJO phase, therefore results based on OMI suggest an even greater phase lag of the MJO cycle of mean precipitation over water relative to that over land, exceeding one MJO phase ($\Delta\phi_{MJO,\ fh} = 1.1$). Further, over land, the skew of the MJO cycle is much less negative (not below -0.3 in any of the

land regions), which suggests a more gradual weakening of mean precipitation over land in the MJO cycle than RMM.

This phase discrepancy between RMM and OMI is mirrored and further exaggerated for the MJO cycle of DC amplitude. Over land, the OMI typically suggests MJO cycle phases that are very slightly later. Over water, the mean MJO cycle is shifted 0.8 MJO phases later in OMI relative to RMM, from 2.7 to 3.5. As a result, the contrast between the phases of the MJO cycle of DC amplitude over land and water doubles, such that OMI suggests that the DC amplitude over land, on average across the western MC region, peaks more than a whole MJO phase earlier than over surrounding waters. Another result of this disparity is that the in-situ lag of the MJO cycle of peak precipitation behind the MJO cycle of DC amplitude is less positive according to the OMI than to the RMM index, especially over water.

Interestingly, the difference between the phases of MJO cycle of DC timing for RMM and OMI is similar to that of DC amplitude; MJO phases according to the OMI are typically later, especially over water. This suggests that, although the lag relationship between the phases of the MJO cycles of DC amplitude and DC timing is complex and regionally-dependent (Figure 4.3e), the relationship is generally independent of the MJO index considered.

4.4 Discussion

The results of this study are in accordance with several previous studies demonstrating that the amplitude of the DC varies roughly in phase with mean precipitation, across an MJO cycle. Comparison of the phases of the MJO harmonics of mean precipitation and of DC amplitude highlights a characteristic phase lag of the cycle of mean precipitation behind that of DC amplitude by approximately half an MJO phase (Figure 4.3b), both over water and land, though with greater consistency over water. Peatman et al. (2014) qualitatively reflect that the MJO cycles of both mean precipitation and DC amplitude, based on 14 boreal winter seasons of precipitation from the Tropical Rainfall Measuring Mission (TRMM) satellite, tend to lead the MJO cycle of OLR by one MJO phase over land, implying that mean precipitation and DC amplitude vary approximately in phase, while Vincent & Lane (2016) describe the calm, clear and humid conditions in the days immediately preceding arrival of an active MJO envelope as very favourable for a strong DC. As was demonstrated

in Chapter 2, the choice of phase characteristic may influence such subtle comparisons of phases, however this study finds that this half-an-MJO phase lag of mean precipitation behind DC amplitude is robust, observed in the basic characteristic of peak phase as well as the MJO harmonic phases. This complements the findings of Birch et al. (2016), who showed that over the far western MC (predominantly Sumatra and peninsular Malaysia), mean DC amplitude in TRMM peaks in MJO phase 2 before mean precipitation peaks in MJO phase 3 (with both reaching a minimum in MJO phase 5), however no clear evidence was found in their study for DC amplitude phase lead over water.

The results of this study also consolidate the existing evidence for the phase lead of land ahead of surrounding waters, concerning both mean precipitation and DC amplitude (e.g. Oh et al., 2012; Peatman et al., 2014; Birch et al., 2016; Vincent & Lane, 2017). For example, Peatman et al. (2014) demonstrated a phase lead of approximately one MJO phase of both mean precipitation and DC amplitude over land ahead of their marine counterparts. The present study found a slightly lower phase lead, of 0.8 MJO phases for mean precipitation and 0.6 MJO phases for DC amplitude, of the MJO harmonic of the mean land cycle ahead of the mean marine cycle. The precise values presented in this study compare land and sea broadly across the western MC region, rather than comparing specific land areas with nearby waters, however since there is not a strong bias in land distribution toward either the west or the east of the western MC region, it is reasoned that this broad comparison should reflect local land–sea phase contrasts reasonably well. Previous studies have suggested that while mean precipitation is generally enhanced within the active envelope of the MJO, increased cloud cover weakens the land–sea breeze circulations that largely drive the DC of precipitation (e.g. Birch et al., 2016). When uninhibited by the increased cloud cover of the active MJO envelope, strong diurnal convection results in precipitation being concentrated over land, whereas precipitation is more evenly distributed between land and water under the influence of the active MJO. Therefore over land, mean precipitation begins to decrease as soon as the front of the active MJO envelope arrives and inhibits the strong DC. Sakaeda et al. (2017) found that this lag relationship is not statistically significant, however the strong spatial coherence of the lag between the MJO cycles of mean precipitation and DC amplitude shown in this study are suggestive of a robust relationship.

Variability of the timing of the DC across the MJO cycle has been a more contentious topic. The methodology applied by a handful of studies to

understand MJO-associated variability of the timing of the DC relied on broad areal averaging (Tian et al., 2006; Suzuki, 2009; Lu et al., 2019), which as shown in the present study, masks strong opposing cycles in different local areas. Other studies do identify a non-trivial relationship between MJO phase and DC timing (e.g. Chen & Houze, 1997; Fujita et al., 2011; Rauniyar & Walsh, 2011; Oh et al., 2012; Sakaeda et al., 2017), however the present study is unique in considering this relationship at a grid cell level as opposed to solely considering areal averages. The results of this study demonstrate clear shifts in DC timing of a few hours or more in some locations; the eastern parts of Sumatra, Borneo and the Makassar Strait, along with the western side of the Java Sea, show the greatest systematic dependence of DC timing on the MJO (Figure 4.5). The west side of land and water masses typically experience their earliest DC timing around MJO phase 5, while east sides of land and water masses typically experience their earliest DC timing around MJO phase 2. Westward propagation of precipitation, at least in the composite sense, is seen in MJO phases 1 and 2 across the Makassar Strait and inland from the east coasts of Sumatra and (less coherently) Borneo (Figure 4.6g&h). In contrast, these same locations show apparent eastward propagation of precipitation around MJO phase 5, and over Sumatra and Borneo this propagation extends across the full width of the island (Figure 4.6c). These observations hold for the peak time characteristic of DC timing (though less smoothly), which is a more appropriate indicator of peak precipitation propagation than FDH phase as discussed in Section 2.5.1. These propagation directions mirror the expected large-scale wind directions of the lower troposphere; low-level wind anomalies are directed towards the active envelope of the MJO, which is to the west of the MC over the Indian Ocean during MJO phases 1 and 2, and to the east of the MC over the eastern MC during MJO phase 5. Ichikawa & Yasunari (2006) emphasised the influence of the large-scale circulation pattern on diurnal precipitation with their finding that, over Borneo, afternoon diurnal precipitation is favoured on the leeward (i.e. downwind) side of the central mountainous area — consistent with the west–east divide in mean precipitation regime identified over Borneo in Section 4.3.1. Further to this, Fujita et al. (2011) demonstrated that offshore propagation westward from Sumatra is highly favoured during MJO phases 2 and 3 while the MJO circulation favours large-scale low-level easterly winds, and that the rate of offshore propagation differs even between these adjacent phases. MJO phases 2 and 3 feature an early mean DC timing over the Indian Ocean region (Figure 4.5d), which is likely to be due to the broad expanse of near-coastal water around the Mentawi islands that receives fast-propagating precipitation

with the early morning land breeze. In contrast, during other MJO phases, this area of near-coastal ocean does not receive substantial precipitation with the weaker and slower land breeze and peak precipitation instead occurs later in the morning in phase with the typical open ocean DC. It is noteworthy that Java, where it is common to make the simplifying assumption that the dominant circulation dynamics occur in the meridional direction, also shows evidence of a west–east divide in DC timing regime, suggesting that subtle variability of zonal propagation of precipitation occurs even over Java.

Over the eastern sides of Sumatra and Borneo, there is a strong contrast in DC timing between in MJO phases 1–2, when precipitation is likely rapidly triggered by a sea breeze coming in from the adjacent east coast, and in MJO phase 5, when precipitation arrives late evening after propagating across the width of the island from the west coast. This may justify the strong amplitude of the MJO cycle of DC timing over the eastern sides of Sumatra and Borneo, meanwhile the typically less strong amplitude of variability over the western sides of the islands is due to the fact that diurnal precipitation over the western sides of the islands is triggered by the sea breeze coming in from the west coast regardless of MJO phase. Over the Makassar Strait, during MJO phases 1 and 2 when the DC amplitude is greatest, precipitation is likely to be triggered by a westward-propagating land breeze triggered over Sulawesi, likely reinforced by mountain breeze dynamics. However, during MJO phase 8, there is no evidence of westward propagation of precipitation across the Makassar Strait, and precipitation across the eastern Makassar Strait is triggered substantially later in the morning. Interestingly, during MJO phase 5, the eastward propagation of precipitation across Borneo appears to continue offshore into the Makassar Strait, which hints at the possibility of direct propagation of precipitation from over Borneo without the triggering of offshore precipitation by a distinct land breeze. Over the western Java Sea, a similar phenomenon is observed as across the eastern Makassar Strait; around MJO phase 5, precipitation propagates rapidly eastward from southeastern Sumatra early in the night, whereas around MJO phase 1, propagation from southeastern Sumatra only extends a short distance and most of the western Java Sea therefore experiences precipitation much later in the morning. The variability over the Java Sea is consistent with that found by Oh et al. (2012), who also suggested that the intense precipitation in this area during the active MJO phases (specifically MJO phase 5 in their study, but noted in MJO phase 4 in the present study) is due to strengthened air–sea surface heat and moisture exchange resulting from the superimposing of

the large-scale low-level anomalous westerlies of this MJO phase on the strong westerly mean flow over the Java Sea.

While a robust relationship was demonstrated between the MJO cycles of mean precipitation and DC amplitude, neither of those MJO cycles bear a consistent relationship to the MJO cycle of DC timing (Figure 4.3c&e). Some regions, such as eastern Sumatra, the western Java Sea and the eastern Makassar Strait, show an approximate alignment of the timing of maximum DC amplitude with the timing of the earliest DC timing. Other regions, such as western Borneo, show an approximate opposition, which suggests that the timing of maximum DC amplitude is likely aligned with the latest DC timing. Alignment of the maximum in DC amplitude with a DC timing that contrasts strongly with the DC timing at other MJO phases (early or late) may diagnose areas where a mechanism for a strong DC exists only under specific large-scale conditions. In contrast, most remaining regions lack clear alignment between DC timing and DC amplitude. In such regions, there is not an approximate one-to-one relationship between DC amplitude and timing — knowing one parameter is not enough to allow reliable estimation of the other. Physical interpretation of such a lagged relationship is not straightforward and highly regionally specific, though fortunately, most of the few areas with strong systematic variability of DC timing have an approximately in-phase or opposing-phase alignment.

Changes in the timing of the DC of precipitation may be related to changes in the relative proportions of convective and stratiform cloud cover. Stratiform clouds and precipitation tend to dominate within the active envelope of the MJO, while convective precipitation is more dominant during suppressed MJO conditions (e.g. Rauniyar & Walsh, 2011; Sakaeda et al., 2017; Alber et al., 2023). Sakaeda et al. (2017) showed that the timing of peak precipitation shows more day-to-day consistency under suppressed MJO conditions, while under active MJO conditions a later peak time tends to be favoured, proposed to be associated with the greater longevity and horizontal extent of stratiform anvils following convective events under active MJO conditions. The MJO cycle of DC spike, which generally indicates more positive spike over water during suppressed MJO phases, suggests greater day-to-day consistency in the timing of diurnal activity under suppressed MJO conditions, which is consistent with the findings of Sakaeda et al. (2017). However, the regime contrast between western and eastern land masses and water masses was not noted in previous studies investigating the modulation of the DC by the MJO. While the eastern sides of land and water masses are found in this study to experience later

diurnal precipitation under active MJO conditions, which is consistent with previous studies and the suggested mechanism of increased late stratiform precipitation, the earlier DC timing observed across the western sides of land and water masses under active MJO conditions requires explanation by an alternative mechanism. The transition from low-level easterlies to low-level westerlies during active MJO conditions may result in slightly more rapid eastward advection of convective cells away from the western sides of the large islands than during suppressed MJO conditions.

As in the previous two chapters, the skew-permitting and spike-permitting waveforms have broadened the characterisation of the DC and its variability by considering elements of its oscillatory nature. The MJO cycle of DC skew was found to vary approximately in phase with the MJO cycle of DC timing, or in other words, the earliest DC maximum and the most rapid intensification roughly align. This suggests that the timing of the diurnal minimum is less influenced by the MJO than the timing of the diurnal maximum. Meanwhile, the DC spike tends to be more positive during the suppressed MJO phases when diurnal activity dominates, suggesting that there may be less day-to-day variability in the manifestation of diurnal activity during the suppressed MJO phases. In addition, the skew-permitting waveform has shown to offer a very different characterisation of MJO cycles than the first MJO harmonic in many cases, such as the MJO cycle of mean precipitation over Java, which weakens rapidly between MJO phases 4 and 5 and gradually intensifies through the remainder of the MJO cycle.

This chapter has investigated the modulation of the DC by the MJO by considering variability of the various DC parameters, and has demonstrated a systematic influence of the MJO on the amplitude, timing and asymmetric characteristics (skew and spike) of the DC. By considering the MJO cycle of the DC parameters at each grid cell, a clear west–east regime divide was identified across a range of islands and water masses, indicating westward propagation of precipitation prior to the arrival of the MJO active envelope (MJO phases 1 and 2) and a transition to eastward propagation once the MJO active envelope has passed over to the east (MJO phase 5). These results consolidate the significant modulation of the DC by the MJO that has been demonstrated in previous studies, and have shed light on the complexities of this modulation. This spatially detailed modulation benchmark across the western MC may prove a useful point of reference for future studies investigating of the modulation of the DC by the MJO in weather forecasting models.

Chapter 5

Synthesis

The research presented in this thesis was motivated by the importance of understanding the nature of dominant modes of variability of precipitation over the Maritime Continent (MC), specifically focusing on the diurnal cycle (DC) and to what extent the increasingly well-resolved spatio-temporal complexities of the DC allow for more detailed characterisation and understanding of the nature of the DC. Within this theme, three research questions (RQs) were defined (Section 1.5), and the research insights from across the previous three chapters will be considered in response to these RQs across the following three sections. Further questions are then discussed in Section 5.4, with concluding remarks in Section 5.5.

5.1 RQ1: Resolution, Complexities and Characterisation

Much critical research on the observed DC of precipitation across the MC has been based on data from the Tropical Rainfall Measuring Mission (TRMM) satellite. The TRMM 3B42 data product offered the finest temporal resolution of gridded precipitation data at a 3-hour spacing, meaning that the DC could be resolved to eight data points. With the advent of the Global Precipitation Measurement (GPM) satellite in 2014 and its Integrated Multi-satellite Retrievals for GPM (IMERG) data product, precipitation may now be resolved to a 30-minute temporal resolution (and an improved spatial resolution). This enables investigation of rapid changes in precipitation rate associated with diurnal dynamics and allows for much more precise characterisation of, for instance, the time of maximum precipitation. A new DC characterisation

framework was developed and applied in this thesis with the intention of capturing the more complex characteristics of the DC that might be better resolved by IMERG. RQ1 poses the question: "Does improved spatio-temporal resolution of the DC of precipitation allow for more complex features to be identified than in previous research?," which the remainder of this section will address.

In Section 2.4, the amplitude and phase of the observed DC of precipitation were characterised by the "basic characteristics" of diurnal half range and peak time. More so than the first diurnal harmonic (FDH) amplitude, the half range is liable to be greater in IMERG than in TRMM 3B42 purely due to the effect of finer temporal resolution. In many locations, maximum precipitation in IMERG is much stronger than the precipitation rate around two hours before or after the maximum (e.g. Figure 2.3d&e), therefore the equivalent DC at 3-hour resolution will feature a watered down maximum magnitude. In locations with a weaker DC, the dominance of noise is more profound in IMERG, again resulting in a greater half range than TRMM 3B42, though misleadingly in this circumstance. The temporal resolution of IMERG is sufficient to resolve multiple data points around the precipitation maximum, therefore further improvements in temporal resolution beyond IMERG are not likely to lead to further substantial changes in resolved amplitude (except by effect of added noise). The greater dominance of noise in IMERG also impacts on the peak time characteristic; open ocean locations are more prone to an incoherent peak time signal in IMERG (e.g. the southwestern corner of Figure 2.2b) than in TRMM 3B42 (Figure 1.2c).

One of the implications of greater precision of the peak time characteristic in IMERG is improved resolution of phase propagation. Since propagation typically extends for a time span of up to 9–12 hours offshore and less for inland propagation over the large islands, estimates of the speed of phase propagation from the 3-hour resolution of TRMM 3B42 come poorly constrained relative to those of IMERG. For example, offshore of northwestern Borneo, close inspection of Figure 1.2c reveals an offshore propagation through the five time intervals between (and including) 3am and 3pm LST — fewer time intervals are covered in the offshore transects of most other coastlines. In comparison, offshore phase propagation is resolved across the order of 20 time intervals in IMERG (Figure 2.2b); northwest of Borneo, propagation of peak time from midnight along the coastline to around midday some 350–400 km offshore indicates an average phase propagation speed of order 30 m s^{-1}. The finer spatial resolution of IMERG is necessary in combination with finer temporal

resolution in order to horizontally resolve subtle changes in peak time — based on a phase propagation speed of 30 m s^{-1}, each 30-minute peak time interval should span an average distance of about 54 km, which is approximately the width of two grid cells in TRMM 3B42. While it is possible to achieve a more continuous characterisation of the DC phase using the FDH approximation, this has a systematic tendency to lead to overestimation of phase propagation speed as discussed in Section 2.5.1.

Much of the research undertaken has been dedicated to the investigation of asymmetries of the DC which, in their extremes, feature very rapid changes in precipitation rate that require high temporal resolution in order to resolve well. Many land locations feature a rapid intensification of precipitation rate in the afternoon, characterised as positive skew (Figure 2.5a&b); a moderately extreme location may be characterised with $\alpha = 0.5$, which indicates an intensification of precipitation lasting just over six hours. In TRMM 3B42, this DC might only feature one time interval between the minimum and maximum, which would offer a very poor constraint on the intensification duration, likely between 3–9 hours. As such, attempts to apply form-fitting of the skew-permitting waveform to such locations in TRMM 3B42 data may not produce a very robust skew value (an example of this non-robust skew characterisation is the yellow dashed line in Figure 4.7c, which only features one data interval between the maximum and minimum). With IMERG, even the most rapid intensification and weakening is captured across several time intervals, offering a much more robust constraint. Further improvements in temporal resolution beyond that of IMERG are unlikely to significantly influence the robustness of the characterisation of such rapid changes in precipitation rate.

The skew-permitting waveform (Equation (2.4) and Figure 2.5a) and the spike-permitting waveform (Equation (2.5) and Figure 2.5c) have both proved to be effective at capturing and quantifying such complexities in certain circumstances. The skew-permitting waveform was especially useful for the characterisation of the rapid intensification of precipitation in the DC over parts of Borneo and Sumatra within 200 km or so of the coastline, and offshore of southwestern Sumatra parallel to the Mentawi Islands (Figure 2.6), where the rapid intensification of precipitation is followed by a reasonably steady prolonged weakening of precipitation. While Java, northern Sumatra and other isolated land areas also experiences a rapid intensification of precipitation, they do not experience a steady weakening akin to the aforementioned parts of Borneo and Sumatra, but a rapid weakening followed by much more gradual

continued weakening. This diurnal behaviour is better characterised by the spike-permitting waveform, because the asymmetry of duration of intense precipitation to weak precipitation is more quantitatively important than the asymmetry of intensification duration against weakening duration. One might consider formulating a hybrid waveform incorporating both the skewed and spiked forms of asymmetry, in order to capture both characteristics when present together. One complication would be ensuring an intuitively meaningful quantitative scale of both skew and spike across the two-dimensional parameter space; while it is easy to conceptualise adding spike to a DC with any magnitude of skew, skew would become a less meaningful mode of asymmetry as the magnitude of spike increases, and it would therefore become challenging to interpret any pattern in skew parameter independently of the pattern of spike parameter. Further, such a hybrid waveform would still be unable to appropriately characterise any DC with two (or more) distinct diurnal precipitation maxima.

The inability to characterise bimodal distributions in diurnal precipitation is one drawback of the characterisation framework utilised in this study. This is slightly problematic over the eastern parts of Borneo, Sumatra and peninsular Malaysia (Figure 2.3b), however these areas tend to experience a weaker DC than western land areas (Figure 2.2a), so might be considered less critical to the underlying dynamics. However, the DC simulated by the convection-parametrised configuration (MC12) of the Met Office Unified Model (MetUM) widely features a bimodal distribution of precipitation over inland parts of Sumatra and Borneo (Figure 3.4b). In places, the two diurnal maxima occur close to 12 hours apart, while in other places, they occur only a handful of hours apart. In cases where the maxima are close to one another, the improved temporal resolution of IMERG is necessary in order to resolve the observed DC sufficiently to be confident that there are not two distinct diurnal maxima in precipitation, as in the model, that are simply not resolved separately.

The waveform characterisation framework used here is not able to effectively characterise model errors in locations with a bimodal precipitation distribution in the modelled or observed DC, however it is applicable in other locations. For example, comparison of the skew parameter shows that intensification of precipitation is too gradual over the seas of both MC12 and the convection-permitting model (MC2) (Figure 3.7c&e) while comparison of the spike parameter shows that precipitation over the Java Sea is too temporally constrained in both MC12 and MC2, however the duration of the precipitation

peak over land tends to be accurate (Figure 3.8c&e).

The variability in DC timing through the course of the Madden-Julian Oscillation (MJO) cycle is also typically very subtle (Figure 4.5) and would not be detected in the cycle of TRMM 3B42 peak time. The DC timing might instead be characterised by the FDH phase in order to achieve a continuous representation of timing that might register subtle shifts in diurnal timing within the TRMM 3B42 temporal resolution of 3 hours, and in this way the results described in Section 4.3.3 might have been discoverable prior to the availability of IMERG-resolution precipitation data. However, as discussed above concerning the misrepresentation of phase propagation, this approach requires an assumption to be made that any time difference between the FDH phase and the peak time is fixed, in this case with respect to MJO phase rather than with respect to distance offshore. As discussed in Section 4.3.4, the DC skew parameter does show systematic variability according to the phase of the MJO across some land and sea areas, typically with more positive skew occurring after the active MJO phases over the western sides of land and water bodies (Figure 4.7), which implies a variable time difference between the FDH phase and the peak time. As such, the temporal resolution of IMERG might be considered necessary to resolve the impact of the MJO on the timing of peak precipitation across the MC.

5.2 RQ2: Model Simulations

Many previous studies have investigated the simulation of the DC of precipitation by convection-parametrised and convection-permitting configurations of various models. It is typically observed that convection-parametrised models trigger precipitation in phase with the peak in incoming shortwave radiation (ISWR) around midday, around six hours earlier than is observed (e.g. Figure 1.3b), while convection-permitting models simulate the phase of the DC much more faithfully but may struggle to achieve an accurate amplitude. Analysis of the DC simulated by the convection-parametrised and convection-permitting configurations of the MetUM (Chapter 3) suggests that the characteristics of the DC in these models is largely in keeping with these norms, however the modelled DCs here were also analysed with regard to their asymmetric characteristics. RQ2 poses the questions: "To what extent can either a *convection-parametrised* model or a *convection-permitting* model succeed at faithfully simulating the complex

features of the observed DC of precipitation, and what are the nature and likely dynamical causes of any differences?," which the remainder of this section will consider in light of the MetUM hindcast suites (see Section 3.2) developed in association with the *TerraMaris* project.

Diurnal variability over land in the convection-parametrised model (MC12) is heavily concentrated across high topography (Figure 3.2d), and very strong horizontal gradients in DC half range are observed. A close inspection of successive time intervals finds that the early afternoon development of precipitation is highly localised; at 9am UTC (around 4:30pm LST over central Borneo), a grid cell at 2.95°N, 114.95°E shows a precipitation rate of 2.9 mm hr^{-1} based on the 900-day composite, while all surrounding grid cells experienced a precipitation rate below 2.1 mm hr^{-1} at the same time. Such marked contrasts in half range between nearby areas is a strong indication that the diurnal variability in MC12 is exceptionally consistent from day to day, so the triggering and development of diurnal deep convection over land is both very consistent in location from day to day and too localised for too long. While the day-to-day variability of the DC in MC12 has not been explicitly analysed, there appears to be very little scope for different diurnal regimes dependent on the large-scale conditions, in contrast to the observed DC (Peatman et al., 2021). Diurnal variability is consequently far too strong over high topography, and too low over low topography (Figure 3.2e).

While there may be no evidence of day-to-day variability in diurnal regime at any land location in MC12, multiple diurnal regimes can be distinguished spatially across the islands. The near-coastal DC features one maximum in precipitation per day (Figure 3.4b) at around midday (Figure 3.3d). Topographic peaks also tend to experience one maximum in precipitation per day, but later in the afternoon. Remaining inland lowlands feature a bimodal diurnal distribution in precipitation with late morning and late evening maxima. There is not the same degree of spatial variability in the manifestation of the DC over land in IMERG, which shows a later afternoon maximum in precipitation over near-coastal areas (Figure 3.3f), and the only evidence for a bimodal diurnal distribution in precipitation over land is over the eastern parts of Sumatra, Borneo and peninsular Malaysia (Figure 3.4c), and in these places the maxima tend to occur in the late afternoon and in the small hours after midnight. There is also no evidence for inland phase propagation in MC12, nor is there as widespread evidence for offshore phase propagation as in IMERG; MC12 does clearly evidence nocturnal phase propagation to the east of Borneo over the

Makassar Strait, however the time of maximum precipitation does not appear to change substantially with distance offshore of southwest Sumatra. The relative lack of propagation of precipitation suggests deficient representation of density currents, particularly the land and sea breezes, in MC12. In contrast, valley breezes appear excessively dominant, with the highly localised onset of precipitation suggesting that valley breezes may be too fast and narrow. The parametrisation of turbulence may be insufficient to counteract the development of such strong horizontal wind shear.

The spike parameter in MC12 tends to be slightly more positive than that in IMERG over near-coastal land, while it is typically too negative over the seas of the MC with the exception of the central Java Sea (Figure 3.8e). Over land, this is consistent with the notion that the manifestation of the DC is too consistent in MC12, meaning that the peak in the composite DC is not broadened as a result of day-to-day variability in timing as it is in IMERG. Over water, precipitation rate tends to oppose that over land, with a brief drop in precipitation rate centred around early afternoon disturbing an otherwise rather consistent precipitation rate through the night; this resembles the first hypothesis for observed negative spike discussed in Section 2.7.2 (Figure 2.9g). The negative skew parameter over water (Figure 3.7d) indicates a rapid suppression of precipitation over water in MC12, occurring within a few hours of the onset of precipitation intensification over land. In the absence of clear offshore phase propagation, most of the seas surrounding the MC appear to experience a DC more comparable to the open ocean regime than the offshore coastal regime (Kikuchi & Wang, 2008). The dynamics governing the open ocean DC are slightly too strong (Figure 3.5b,d&f), but where the open ocean regime encroaches too close to the coastlines this results in too weak a DC over the near-shore seas. In general, MC12 has too sharp a land–sea regime boundary, resulting in a strong and consistent DC within tens of kilometres of the coastlines while in IMERG there is a slightly broader coastal boundary region separating the strong diurnal regimes of land and sea.

Previous modeling studies have found that it is the use or independence from convection parametrisation that has the most critical influence on the degree of faithfulness of a model at simulating the DC (e.g. Love et al., 2011; Argüeso et al., 2020), and the contrast between MC12 and the convection-permitting model (MC2) in this study is consistent with this view. MC2 is able to simulate the phase of the DC to within two hours, often much better, in most locations, with only a slight bias toward a late peak over most near-coastal seas

(Figure 3.3c). The amplitude is generally too strong (Figures 3.2c & 3.5a,c&e), particularly over high topography, however this largely mirrors the general wet bias of MC2 (Figure 3.1c), suggesting that large-scale conditions are more responsible for the positive amplitude bias than overactive physical mechanisms driving the DC. Beyond the amplitude and phase, the nature of diurnal variability, including areas with a bimodal diurnal distribution of precipitation (Figure 3.4a), is well represented, as evidenced by its widespread strong positive correlation with the IMERG DC across the western MC domain (Figure 3.9a). Phase propagation inland from the coastline through the afternoon is simulated very faithfully in MC2, however phase propagation offshore overnight does not extend as far from the coastline as in IMERG. A notable example is to the northwest of Borneo, where offshore propagation is evident in the composite as far as around 400-500 km offshore, in comparison with perhaps 100 km offshore in MC2. It may be that the physical processes responsible for the propagating precipitation signal close to the coast — density currents, such as land breezes and mountain breezes — are represented, while the physical processes responsible for the propagation signal further from the coastline — often demonstrated or suggested to be gravity waves (e.g. Love et al., 2011; Peatman et al., 2023) — may either be too weak in MC2 or the offshore lower troposphere may be too resistant to the triggering of convection by gravity wave destabilisation.

Subtle but robust biases are also present in the asymmetry parameters of MC2, often of the same nature as in MC12 but less extreme. These include too positive spike over the Java Sea and generally too negative spike over other near-coastal seas (Figure 3.8c and too negative skew over most land and near-coastal seas (Figure 3.7c). The magnitude of biases in the asymmetry parameter is no more striking than the magnitudes of amplitude and phase biases, which instills confidence that inspection of the amplitude and phase biases alone is also indicative of the degree of faithfulness of MC2 at simulating other gross characteristics of the DC. Indeed, overall, MC2 provides a good demonstration of the capacity of a convection-permitting model with a coupled ocean to faithfully simulate the DC broadly across the western MC.

5.3 RQ3: MJO Influence on Diurnal Cycle

A key part of the motivation for investigating the DC over the MC is because of its scale interactions with modes of intra-seasonal variability. The dominant mode of intra-seasonal variability is the MJO (Section 1.4) which triggers a range of atmospheric teleconnection responses that influence weather across much of the Earth over the following few weeks. In order for a model to accurately simulate the characteristics of the MJO and its teleconnection responses, the scale interaction between the MJO and the DC must faithfully reflect the observed scale interaction. Furthermore, extreme weather events over the MC tend to occur when multiple organised envelopes of convection — associated with multiple modes of variability often including the MJO — come together, and the manifestation of the extreme weather is also strongly influenced by the DC when the interaction is over the MC. In keeping with the DC-oriented discussion, RQ3 focuses on the downscale side of the scale interaction in posing the question: "What is the nature of the influence of the MJO on the manifestation of the DC of precipitation, and in how much detail is it possible to resolve this scale interaction?"

In Chapter 4, the composite DC was calculated for each of the eight MJO phases as defined by the real-time multivariate MJO (RMM) index of Wheeler & Hendon (2004), and fluctuations in the half range, peak time, skew and spike of the DC were considered. The half range (and other amplitude metrics) was found to increase and decrease substantially through the MJO cycle in many locations, especially over land (Figure 4.2a). Over land, the DC varies more in amplitude through an MJO cycle than mean precipitation does, while over water, the MJO cycle of mean precipitation is not typically coupled with a strong fluctuation in DC amplitude (Figure 4.4b). This is consistent with Peatman et al. (2014) who quantified the proportion of additional precipitation during the MJO active phase that manifests as a more extreme diurnal maximum (80% over land). The occurrence of the strongest DC slightly ahead of the MJO active envelope has been suggested to be the result of the optimal balance between a moist, convectively unstable lower troposphere and clear skies, allowing for strong diurnal solar radiative forcing.

The composite DC might be thought of as constituting a diurnal component — any precipitation beyond the diurnal minimum rate, variable through the day — and a non-diurnal component which is fixed at the diurnal minimum rate throughout the day (Figure 5.1). If 100% of the MJO signal over the

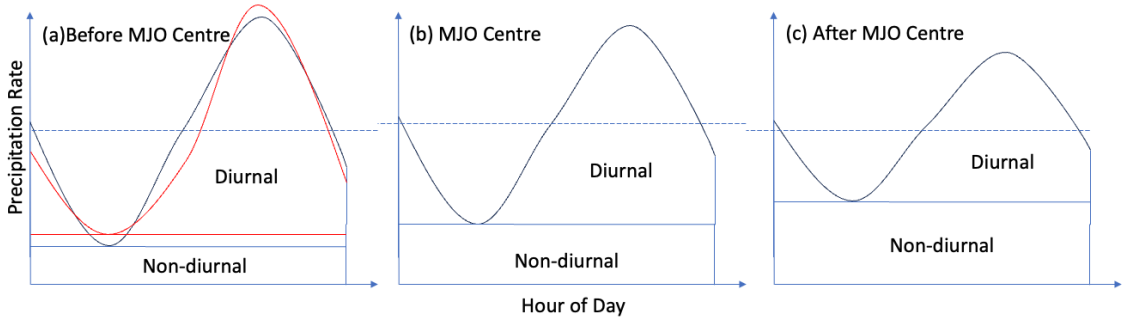

Figure 5.1: Schematic depiction of the diurnal and non-diurnal components of precipitation and their relative magnitudes (a) before, (b) during and (c) after the centre of the MJO active envelope. Mean precipitation is marked by the dashed blue lines and is greatest during the centre of the MJO active envelope. The most intense diurnal maximum occurs before the centre of the MJO active envelope, and the strongest non-diurnal precipitation occurs after the centre of the MJO active envelope. The red curve in panel (a) factors in the more positive spike parameter observed over water before the MJO centre, which raises the proportion of non-diurnal precipitation (horizontal red line) and raises the diurnal maximum relative to the assumption of a uniform MJO nature.

MC manifested as a strengthened DC (i.e. non-diurnal precipitation was constant throughout the MJO cycle), then the MJO phases of maximum mean precipitation and of maximum DC amplitude must match. However, a systematic phase lead of DC amplitude ahead of mean precipitation is observed (Figure 4.3b, especially robust over water. Since the diurnal component reaches a maximum before the maximum total precipitation associated with the MJO active envelope, this must be counterbalanced by a phase lag of the non-diurnal component of precipitation behind the maximum in mean precipitation. In other words, the wettest diurnal maximum occurs before the centre of the MJO active envelope arrives (Figure 5.1a), and the wettest diurnal minimum occurs after the centre of the MJO active envelope has passed (Figure 5.1c). Such a quantification relies on the nature of the DC being consistent throughout an MJO event: in this study, there is negligible variability of the skew parameter over either all land or all water (Figures 4.7c&d), however the spike parameter tends to be most positive before the MJO active envelope arrives over water (Figure 4.8d). Factoring in a slightly more positive spike over water before the MJO active envelope arrives, the non-diurnal component of precipitation before the MJO centre would be slightly stronger and the diurnal maximum would be yet stronger. This weakens the variability of non-diurnal precipitation relative to diurnal precipitation across an MJO cycle, therefore the proportion of MJO manifestation as changes to the DC is stronger over water than the FDH approximation suggests. There is no systematic variability of the spike

parameter over land as a whole (Figure 4.8c), therefore the 80% manifestation of the MJO as changes to the DC amplitude quoted by Peatman et al. (2014) holds even when variable DC nature is allowed for.

A general phase lead of land ahead of surrounding waters is observed for mean precipitation and, to a slightly lesser extent, DC amplitude. This is also consistent with previous findings (Peatman et al., 2014) and has been referred to as the "precipitation vanguard". This is considered to be a result of the contrast in the proportion of the diurnal component of precipitation over land versus water. Over land, the dominance of the diurnal component of precipitation means that maximum mean precipitation occurs close to (though slightly lagging) the time of strongest DC, which is ahead of the MJO active envelope. Over water, the more dominant non-diurnal component of precipitation peaks later while the MJO active envelope is overhead.

The results of the Chapter 4 support the notion that the MJO is capable of modulating the timing of the DC, as well as the amplitude. This modulation is too subtle to have been identified with confidence in TRMM data, as discussed in Section 5.1, but is nonetheless clearly systematic. After the MJO centre has passed, the western sides of the large islands experience an earlier diurnal precipitation maximum, while the eastern sides of the islands experience their earliest diurnal precipitation maximum during the early phases of the MJO before it arrives over the MC 4.5b). A similar pattern emerges across certain water bodies including the Java Sea, the Makassar Strait and the eastern Pacific Ocean close to southwest Sumatra. This west–east regime divide is present even over Java, where the dominant physical processes are often assumed to occur perpendicular to the length of the island, approximately in the meridional plane. This is the result of an oscillation between westward phase propagation of precipitation favoured during the early MJO phases and eastward phase propagation of precipitation favoured during the late MJO phases after the MJO centre has traversed the MC (mostly clearly observed over the Makassar Strait comparing MJO phases 1–2 with phases 5–6; Figure 4.6). These propagation directions correspond to the large-scale prevailing low-level zonal winds (Figure 1.15). Locations where the DC is most independent of the large-scale conditions can also be identified, including Java, much of northern and western Sumatra and Borneo, and western peninsular Malaysia (Figure 4.5a). In particular, parts of the coastline that have the longest, most convex surrounding coastline tend to experience the smallest fluctuations in DC peak time by MJO phase — these locations correlate with regions of most positive DC spike (Figure 2.5d), which

adds weight to the suggestion that positive DC spike indicates low day-to-day variability in the local timing of precipitation events (see Section 2.7.2).

The concept of the "MJO harmonic" has been used in the past to characterise the MJO cycle, specifically of the DC amplitude (Peatman et al., 2014). This characterisation parallels the FDH characterisation of the DC, for which certain systematic misrepresentations were highlighted in Chapter 2, therefore the asymmetric waveforms were used alongside the MJO harmonic in this study to characterise the MJO cycle. When the RMM index is used to composite by MJO phase, the skew-permitting waveform uncovers a systematic rapid weakening over land of mean precipitation and of DC amplitude following their respective maxima, most notably over Java (yellow dashed line in Figure 4.2c). The magnitude of the skew parameter in mean precipitation is comparable to that in DC amplitude, therefore the choice of phase parameter has only a slight effect on the magnitude of the identified phase lead of the DC amplitude, which was here found to be of order 0.5 MJO phases over both land and water; in contrast, Peatman et al. (2014) did not resolve a systematic phase lag between DC amplitude and mean precipitation. It is possible to resolve the impact of the MJO on the DC to greater resolution by subdividing each MJO phase into segments and calculating the composite DC for each segment, however there will be a limit beyond which the small number of days within each segment will contribute more noise to the MJO cycle than the improved resolution through the MJO cycle is worth. As such, with several years of IMERG data available, the downscale influence of the MJO on the DC can be resolved to at least eight (and likely more) intervals of the MJO cycle, and spatial averaging or coarsening is not necessary to extract the scale interaction signal so, theoretically, features of variability down to the 0.1° IMERG horizontal resolution may be resolved. In practice, features of spatial variability of length scale 100 km are evident, so this spatial resolution is more than sufficient.

5.4 Further Questions

A range of avenues for future research exist in light of this research. Having introduced two new characterisation methods for a DC in Section 2.6, an effort was made to correlate the new characterisation parameters — skew and spike — with patterns of day-to-day variability of DC manifestation. The "event-based analysis" described in Section 2.7.2 considered the timings

of individual precipitation events at a small handful of locations that were considered representative of other positive/negative skew/spike locations. A more complete analysis of the properties of the distributions of precipitation event timings may allow for more robust conclusions to be drawn on the nature of the DC and its variability implied by a positive/negative skew/spike in the composite. In turn, this may benefit studies that apply these characterisation methods to composites of other variables across the sciences; some ideas for potential applications were discussed in Section 2.7.3.

Another consideration on the theme of the nature of DC variability is the physical mechanisms associated with dual diurnal peaks in precipitation, or a bimodal diurnal distribution of precipitation, as is observed across the eastern sides of most large MC islands. Such a distribution may result from the existence of two distinct diurnal regimes dependent on background conditions, or it may result from a systematic initiation, weakening, and re-intensification of precipitation on a typical day. The wave index metric (Equation (2.3)) as applied to individual days, or to the MJO phase composites, may help to distinguish between these possibilities. In the latter case (which appears likely based on the findings of Chapter 4 but has not been thoroughly investigated), further work will need to carefully consider a suitable characterisation for the twice-daily precipitation events, though in the former case, the single-peak waveform characterisations here may do a better job of characterising the DC in these bimodal distribution regions once the diurnal regimes have been separated.

Precipitation is the only weather variable that has been explicitly analysed within this thesis, therefore consideration of wind and cloud components, humidity, temperature, pressure and other related variables would give a more complete view of the nature of the diurnal cycle and allow for propagation mechanisms such as density currents and gravity wave modes to be more rigorously identified. Variable output from the two regional hindcast model suites described in Chapter 3 — MC12 and MC2 — is at a higher resolution and would allow thorough investigation of the diurnal mechanisms operating in the model, as well as investigation of variability at other timescales including the intra-seasonal timescale. Howard et al. (in review) discussed a preliminary investigation of MJO variability in the models, finding MJO variability present at both resolutions. For the characterisation of the observed DC, other appropriate data products would need to be sourced. The ECMWF Reanalysis v5 (ERA5) is perhaps the closest data product, supplying a range of weather variables at a horizontal resolution of approximately 31 km by 31 km and at an hourly

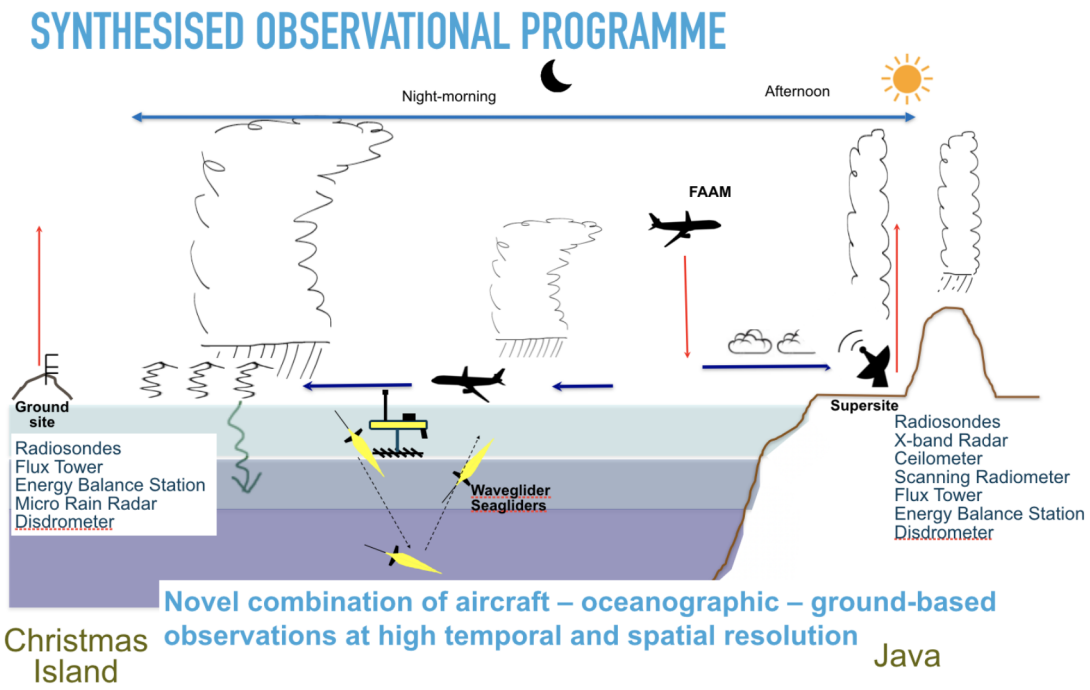

Figure 5.2: Schematic of *TerraMaris* field campaign plans for coordinated meteorological observations along a transect between Java and Christmas Island. *Adapted from the TerraMaris ground observations staff advert, produced by Cathryn Birch and Ryan Neely III.*

temporal resolution. This resolution would be sufficient to investigate most large-scale diurnal processes, however it is heavily dependent on reanalysis procedures to achieve complete gridded data.

Ideally, an intensive field campaign should be conducted to directly source the range of meteorological variables necessary for characterisation of the observed DC across the range of relevant meteorological variables. Many field campaigns have been conducted at selected locations across the MC, however there is scope for a large-scale field campaign to provide synchronous, coordinated observations of a broad range of meteorological variables across a broad study area for an extended duration of time — ideally at least two months for a good chance of gathering observations across a range of MJO phases (and magnitudes). Such a field campaign is by no means simple to arrange and is subject to a range of unforeseeable barriers; the *TerraMaris* field campaign had been designed to fill this observational data gap (Yoneyama & Zhang, 2020), but did not come to fruition as a result of the global helium shortage (2019) and the direct and lasting impacts of the Covid-19 global pandemic (2020-3). Such coordinated observations might include ground-based observations (e.g. radiosondes, flux towers,

rain radar, disdrometers), airborne observations (dropsondes deployed from aircraft) and oceanographic observations (temperature and salinity profiles and passive acoustics from autonomous underwater vessels such as Seagliders), as illustrated in the *TerraMaris* field campaign plans schematic (Figure 5.2).

While land-based precipitation is reasonably straightforward to measure at high temporal resolution with a rain gauge, rough sea surface conditions make direct precipitation measurements over water more challenging to reliably acquire. One route of investigation (and the original plan for this thesis subject to the success of *TerraMaris*) is the use of passive acoustic monitoring to acquire snippets of audio from within the water column. Rain droplets impacting the sea surface produce noise within a specific frequency range (dependent on sea surface roughness and droplet size), therefore studies have attempted the extraction of precipitation intensity via a function of the volume in the specific frequency band. While complicated, this may prove a valuable method with which to determine a high resolution time series of precipitation across the seas of the MC.

Following more directly from the works within this thesis, having established in detail the downscale influence of the MJO on the DC, it would be valuable to investigate the degree of success of models of different types/resolutions at representing this scale interaction. Both MC12 and MC2 have been shown to feature MJO-like variability (Howard et al., in review), so this scale interaction is relevant to both models discussed in Chapter 3. Scale interactions between the DC and other propagating modes of variability may also be considered; for instance, a similar analysis framework might be used to composite the DC for days with convectively-coupled Kelvin waves (CCKWs) present at various longitudinal. The upscale influences are also worthy of more research focus; the DC has been shown in a range of modelling studies to be an integral component of the observed MC barrier effect, however further observational evidence is required to determine the relationship between DC characteristics prior to MJO active envelope arrival and the fate of the MJO over the MC (Ling et al., 2019a). The impact of the DC on CCKWs over the MC has also been considered (Baranowski et al., 2016), and it may be enlightening to return to this scale interaction in the light of a higher temporal resolution DC characterisation.

5.5 Concluding Remarks

The research and discussion within this thesis has furthered understanding of the characteristics and variability of the diurnal cycle (DC) of precipitation over the Maritime Continent (MC), focusing on the impacts of improved resolution of the DC in observations and models. While it has been common practice in studies of the DC to approximate the cycle using the first diurnal harmonic (FDH), satellite-derived precipitation data with a half-hourly temporal resolution (IMERG) reveal that the nature of the DC often approximates poorly to a sinusoidally-varying oscillation, and systematic misrepresentations of the magnitude of variability and the time of maximum precipitation often occur. This has implications for the apparent speed of phase propagation, and suggests that the model evaluation based on comparison of the FDH may overlook significant differences in the nature of the DC.

A novel characterisation framework for cyclic data was developed and applied to describe asymmetries in the DC of precipitation, which provide an extra degree of insight into the nature of diurnal variability as well as helping to characterise the amplitude and phase of the DC more reliably. This novel characterisation framework was applied in the comparison of model-simulated DC with the observed DC, with major biases in amplitude, phase and asymmetry parameters described in a convection-parametrised model configuration and slighter biases described in a convection-permitting model configuration. The characterisation framework was further applied to the MJO cycle, and may prove useful for the approximate characterisation of a range of cycles across the sciences with one main maximum-minimum pair per cycle.

IMERG data were also used to resolve subtle shifts in the characteristics of the DC through an MJO cycle. The most significant result is the west–east regime divide over the large islands in the variability of the phase of the DC through an MJO cycle. While the MJO is in its early stages over the Indian Ocean, the west sides of the islands experience a late diurnal maximum while the east sides of the islands experience their earliest diurnal maximum. After the convective envelope of the MJO has passed east over the western Pacific Ocean, the west sides of the islands instead experience their earliest diurnal maximum while the east sides experience a late diurnal maximum. While the west sides of Sumatra and Borneo demonstrate eastward phase propagation inland from the coast across all MJO phases, the east sides of the islands demonstrate westward

phase propagation inland while the MJO is active over the Indian Ocean, and instead demonstrate a continuation of the eastward phase propagation on the west side of the island while the MJO is active over the western Pacific Ocean. As such, DC phase tends to vary more substantially over the east sides of the islands, and these two regimes may be distinct enough to explain the bimodal distribution of precipitation typical over the eastern sides of Sumatra, Borneo and peninsular Malaysia.

The detailed characterisations of the DC of precipitation and its variability through an MJO cycle will be of significance to those with an interest in weather forecasting and model validation over the MC.

References

Abhik, S., Hendon, H.H., & Zhang, C. 2023. The Indo-Pacific Maritime Continent Barrier Effect on MJO Prediction. J. Clim., **36**, 945–957.

Adames, Á.F., & Kim, D. 2016. The MJO as a dispersive, convectively coupled moisture wave: Theory and observations. J. Atm. Sci., **73**, 913–941.

Adames, Á.F., & Wallace, J.M. 2014. Three-dimensional structure and evolution of the vertical velocity and divergence fields in the MJO. J. Atm. Sci., **71**, 4661–4681.

Ahn, M.-S., Kim, D., Kang, D., Lee, J., Sperber, K.R., Gleckler, P.J., Jiang, X., Ham, Y.-G., & Kim, H. 2020a. MJO Propagation Across the Maritime Continent: Are CMIP6 Models Better Than CMIP5 Models? Geophys. Res. Lett., **47**.

Ahn, M.-S., Kim, D., Ham, Y.-G., & Park, S. 2020b. Role of maritime continent land convection on the mean state and MJO propagation. J. Clim., **33**, 1659–1675.

Ajayamohan, R.S., Khouider, B., Praveen, V., & Majda, A.J. 2021. Role of diurnal cycle in the maritime continent barrier effect on MJO propagation in an AGCM. J. Atm. Sci., **78**, 1545–1565.

Alber, K., Zhou, L., Roundy, P.E., & Solimine, S.L. 2023. Influence of the Madden-Julian Oscillation on the diurnal cycles of convection and precipitation over the Congo Basin. Atm. Res., **294**.

Albright, M.D., Recker, E.E., Reed, R.J., & Dang, R. 1985. The Diurnal Variation of Deep Convection and Inferred Precipitation in the Central Tropical Pacific During January–February 1979. Mon. Wea. Rev., **113**, 1663–1680.

Argüeso, D., Di Luca, A., & Evans, J.P. 2016. Precipitation over urban areas in the western Maritime Continent using a convection-permitting model. Clim. Dyn., **47**, 1143–1159.

Argüeso, D., Romero, R., & Homar, V. 2020. Precipitation Features of the Maritime Continent in Parameterized and Explicit Convection Models. J. Clim., **33**, 2449–2466.

Argüeso, D., Di Luca, A., Jourdain, N.C., Romero, R., & Homar, V. 2022. Mechanisms for Extreme Precipitation Changes in a Tropical Archipelago. J. Clim., **35**, 5519–5536.

As-syakur, A.R., Osawa, T., Miura, F., Nuarsa, I.W., Ekayanti, N.W., Dharma, I.G.B.S., Adnyana, I.W.S., Arthana, I.W., & Tanaka, T. 2016. Maritime Continent rainfall variability during the TRMM era: The role of monsoon, topography and El Niño Modoki. Dyn. Atm. Oceans, **75**, 58–77.

Bai, H., & Schumacher, C. 2022. Topographic Influences on Diurnally Driven MJO Rainfall Over the Maritime Continent. J. Geophys. Res.: Atm., **127**.

Baker, R.D., Lynn, B.H., Boone, A., Tao, W.-K., & Simpson, J. 2001. The Influence of Soil Moisture, Coastline Curvature, and Land-Breeze Circulations on Sea-Breeze-Initiated Precipitation. J. Hydromet., **2**.

Baldi, M., Dalu, G.A., & Pielke, R.A. 2008. Vertical velocities and available potential energy generated by landscape variability - Theory. J. App. Met. Clim., **47**, 397–410.

Ban, N., Schmidli, J., & Schär, C. 2014. Evaluation of the convection-resolving regional climate modeling approach in decade-long simulations. J. Geophys. Res.: Atm., **119**, 7889–7907.

Baranowski, D.B., Flatau, M.K., Flatau, P.J., & Matthews, A.J. 2016. Phase locking between atmospheric convectively coupled equatorial Kelvin waves and the diurnal cycle of precipitation over the Maritime Continent. Geophys. Res. Lett., **43**, 8269–8276.

Baranowski, D.B., Waliser, D.E., Jiang, X., Ridout, J.A., & Flatau, M.K. 2019. Contemporary GCM Fidelity in Representing the Diurnal Cycle of Precipitation Over the Maritime Continent. J. Geophys. Res., **124**, 747–769.

Bayr, T., Dommenget, D., Martin, T., & Power, S.B. 2014. The eastward shift of the Walker Circulation in response to global warming and its relationship to ENSO variability. Clim. Dyn., **43**, 2747–2763.

Bellenger, H., Guilyardi, E., Leloup, J., Lengaigne, M., & Vialard, J. 2014. ENSO representation in climate models: From CMIP3 to CMIP5. Clim. Dyn., **42**, 1999–2018.

Berg, P., Moseley, C., & Haerter, J.O. 2013. Strong increase in convective precipitation in response to higher temperatures. Nature Geoscience, **6**, 181–185.

Bhatt, B.C., Sobolowski, S., & Higuchi, A. 2016. Simulation of diurnal rainfall variability over the maritime continent with a high-resolution regional climate model. J. Met. Soc. Japan, **94A**, 89–103.

Biasutti, M., Yuter, S., Burleyson, C., & Sobel, A. 2012. Very high resolution rainfall patterns measured by TRMM precipitation radar: Seasonal and diurnal cycles. Clim. Dyn., **39**, 239–258.

Birch, C.E., Webster, S., Peatman, S.C., Parker, D.J. Matthews, A.J., Li, Y., & Hassim, M.E.E. 2016. Scale interactions between the MJO and the western Maritime Continent. J. Clim., **29**, 2471–2492.

Bray, E.N., & Dunne, T. 2017. Subsurface flow in lowland river gravel bars. Water Resources Res., **53**, 7773–7797.

Bush, M., Boutle, I., Edwards, J., Finnenkoetter, A., Franklin, C., Hanley, K., Jayakumar, A., Lewis, H., Lock, A., Mittermaier, M., Mohandas, S., North, R., Porson, A., Roux, B., Webster, S., & Weeks, M. 2023. The second Met Office Unified Model-JULES Regional Atmosphere and Land configuration, RAL2. Geosci. Model Dev., **16**, 1713–1734.

Cassou, C. 2008. Intraseasonal interaction between the Madden-Julian Oscillation and the North Atlantic Oscillation. Nature, **455**, 523–527.

Chang, C.-P., Wang, Z., McBride, J., & Liu, C.-H. 2005. Annual Cycle of Southeast Asia-Maritime Continent Rainfall and the Asymmetric Monsoon Transition. J. Clim., **18**, 287–301.

Chao, W.C. 2013. Catastrophe-concept-based cumulus parameterization: Correction of systematic errors in the precipitation diurnal cycle over land in a GCM. J. Atm. Sci., **70**, 3599–3614.

Chen, S.S., & Houze, R.A. 1997. Diurnal Variation and Lifecycle of Deep Convective Systems over the Pacific Warm Pool. Q. J. Roy. Met. Soc., **123**, 357–388.

Coppin, D., & Bellon, G. 2019a. Physical Mechanisms Controlling the Offshore Propagation of Convection in the Tropics: 1. Flat Island. J. Adv. Model. Earth Sys., **11**, 3042–3056.

Coppin, D., & Bellon, G. 2019b. Physical Mechanisms Controlling the Offshore Propagation of Convection in the Tropics: 2. Influence of Topography. J. Adv. Model. Earth Sys., **11**, 3251–3264.

Cravatte, S., Delcroix, T., Zhang, D., McPhaden, M., & Leloup, J. 2009. Observed freshening and warming of the western Pacific Warm Pool. Clim. Dyn., **33**, 565–589.

Da Silva, N.A., & Matthews, A.J. 2021. Impact of the Madden–Julian Oscillation on extreme precipitation over the western Maritime Continent and Southeast Asia. Q. J. Roy. Met. Soc., **147**, 3434–3453.

Dai, A. 2001. Global Precipitation and Thunderstorm Frequencies. Part II: Diurnal Variations. J. Clim., **14**, 1112–1128.

Dai, A. 2023. The diurnal cycle from observations and ERA5 in surface pressure, temperature, humidity, and winds. Clim. Dyn., **61**, 2965–2990.

Dai, A., & Wang, J. 1999. Diurnal and Semidiurnal Tides in Global Surface Pressure Fields. J. Atm. Sci., **56**, 3874–3891.

Dayem, K.E., Noone, D.C., & Molnar, P. 2007. Tropical western Pacific warm pool and maritime continent precipitation rates and their contrasting relationships with the Walker Circulation. J. Geophys. Res.: Atm., **112**.

DeMott, C.A., Klingaman, N.P., & Woolnough, S.J. 2015. Atmosphere-ocean coupled processes in the Madden-Julian oscillation. Rev. Geophys., **53**, 1099–1154.

DeMott, C.A., Wolding, B.O., Maloney, E.D., & Randall, D.A. 2018. Atmospheric Mechanisms for MJO Decay Over the Maritime Continent. J. Geophys. Res.: Atm., **123**, 5188–5204.

Densmore, C.R., Sanabia, E.R., & Barrett, B.S. 2019. QBO influence on MJO amplitude over the maritime continent: Physical mechanisms and seasonality. Mon. Wea. Rev., **147**, 389–406.

Dexter, R.V. 1944. The diurnal variation of warm-frontal precipitation and thunderstorms. Q. J. Roy. Met. Soc., **70**, 129–137.

Dipankar, A., Webster, S., Huang, X.Y., & Doan, V.Q. 2019. Understanding biases in simulating the diurnal cycle of convection over the western coast of Sumatra: Comparison with pre-YMC observation campaign. Mon. Wea. Rev., **147**, 1615–1631.

Dirmeyer, P.A., Cash, B.A., Kinter, J.L., Jung, T., Marx, L., Satoh, M., Stan, C., Tomita, H., Towers, P., Wedi, N., Achuthavarier, D., Adams, J.M., Altshuler, E.L., Huang, B., Jin, E.K., & Manganello, J. 2012. Simulating the diurnal cycle of rainfall in global climate models: Resolution versus parameterization. Clim. Dyn., **39**, 399–418.

Duan, S.B., Li, Z.L., Tang, B.H., Wu, H., Tang, R., Bi, Y., & Zhou, G. 2014. Estimation of diurnal cycle of land surface temperature at high temporal and spatial resolution from clear-sky MODIS data. Rem. Sens., **6**, 3247–3262.

Eastman, R., & Warren, S.G. 2014. Diurnal cycles of cumulus, cumulonimbus, stratus, stratocumulus, and fog from surface observations over land and ocean. J. Clim., **27**, 2386–2404.

Evans, J.L., & Webster, C.C. 2014. A variable sea surface temperature threshold for tropical convection. Aus. Met. Ocean. J., **64**, S1–S8.

Fasullo, J., & Webster, P.J. 1999. Warm Pool SST Variability in Relation to the Surface Energy Balance. J. Clim., **12**, 1292–1305.

Feng, J., Li, T., & Zhu, W. 2015. Propagating and nonpropagating MJO events over maritime continent. J. Clim., **28**, 8430–8449.

Fujita, M., Yoneyama, K., Mori, S., Nasuno, T., & Satoh, M. 2011. Diurnal convection peaks over the eastern Indian Ocean off sumatra during different MJO phases. J. Met. Soc. Japan, **89**, 317–330.

Gage, K.S., & Reid, G.C. 1987. Longitudinal variations in tropical tropopause properties in relation to tropical convection and El Niño-Southern Oscillation events. J. Geophys. Res.: Oceans, **92**, 14197–14203.

Garcia-Carreras, L., Parker, D.J., Taylor, C.M., Reeves, C.E., & Murphy, J.G. 2010. Impact of mesoscale vegetation heterogeneities on the dynamical and thermodynamic properties of the planetary boundary layer. J. Geophys. Res.: Atm., **115**, D3.

Gelaro, R., McCarty, W., Suárez, M.J., Todling, R., Molod, A., Takacs, L., Randles, C.A., Darmenov, A., Bosilovich, M.G., Reichle, R., Wargan, K., Coy, L., Cullather, R., Draper, C., Akella, S., Buchard, V., Conaty, A., da Silva, A.M., Gu, W., Kim, G.-K., Koster, R., Lucchesi, R., Merkova, D., Nielsen, J.E., Partyka, G., Pawson, S., Putman, W., Rienecker, M., Schubert, S.D., Sienkiewicz, M., & Zhao, B. 2017. The modern-era retrospective analysis for research and applications, version 2 (MERRA-2). J. Clim., **30**, 5419–5454.

Gill, A.E. 1980. Some simple solutions for heat-induced tropical circulation. Q. J. Roy. Met. Soc., **106**, 447–462.

Goergen, K., & Kollet, S. 2021. Boundary condition and oceanic impacts on the atmospheric water balance in limited area climate model ensembles. Sci. Rep., **11**.

Gonzalez, A.O., & Jiang, X. 2017. Winter mean lower tropospheric moisture over the Maritime Continent as a climate model diagnostic metric for the propagation of the Madden-Julian oscillation. Geophys. Res. Lett., **44**, 2588–2596.

Good, S., Fiedler, E., Mao, C., Martin, M., Maycock, A., Reid, R., Roberts-Jones, J., Searle, T., Waters, J., While, J., & Worsfold, M. 2020. The Current Configuration of the OSTIA System for Operational Production of Foundation Sea Surface Temperature and Ice Concentration Analyses. Rem. Sens., **12**, 720.

Gottschalck, J., Wheeler, M., Weickmann, K., Vitart, F., Savage, N., Lin, H., Hendon, H., Waliser, D., Sperber, K., Nakagawa, M., Prestrelo, C., Flatau, M., & Higgins, W. 2010. A framework for assessing operational Madden-Julian oscillation forecasts: A clivar MJO working group project. Bull. Amer. Met. Soc., **91**, 1247–1258.

Graham, N.E., & Barnett, T.P. 1987. Sea Surface Temperature, Surface Wind Divergence, and Convection over Tropical Oceans. Science, **238**, 657–659.

Grandpeix, J.Y., & Lafore, J.P. 2010. A density current parameterization coupled with Emanuel's convection scheme. Part I: The models. J. Atm. Sci., **67**, 881–897.

Gregory, D., & Rowntree, P.R. 1990. A Mass Flux Convection Scheme with Representation of Cloud Ensemble Characteristics and Stability-Dependent Closure. Mon. Wea. Rev., **118**, 1483–1506.

Hagos, S., Zhang, C., Feng, Z., Burleyson, C., De Mott, C., Kerns, B., Benedict, J.J., & Martini, M. 2016. The impact of the diurnal cycle on the propagation of Madden-Julian Oscillation convection across the Maritime Continent. J. Adv. Model. Earth Sys., **8**, 1552–1564.

Hassim, M.E.E., Lane, T.P., & Grabowski, W.W. 2016. The diurnal cycle of rainfall over New Guinea in convection-permitting WRF simulations. Atm. Chem. Phys., **16**, 161–175.

He, Y., Monahan, A.H., & McFarlane, N.A. 2013. Diurnal variations of land surface wind speed probability distributions under clear-sky and low-cloud conditions. Geophys. Res. Lett., **40**, 3308–3314.

Helfrich, K.R., & Melville, W.K. 2006. Long nonlinear internal waves. Ann. Rev. Fluid Mech., **38**, 395–425.

Hendon, H.H., & Salby, M.L. 1994. The Life Cycle of the Madden–Julian Oscillation. J. Atm. Sci., **51**, 2225–2237.

Hirons, L.C., Klingaman, N.P., & Woolnough, S.J. 2015. MetUM-GOML1: a near-globally coupled atmosphere ocean-mixed-layer model. Geosci. Model Dev., **8**, 363–379.

Holle, R.L., & Murphy, M.J. 2017. Lightning over three large tropical lakes and the strait of Malacca: Exploratory analyses. Mon. Wea. Rev., **145**, 4559–4573.

Howard, E., Woolnough, S., Klingaman, N., Shipley, D., Sanchez, C., Peatman, S., Birch, C., & Matthews, A.J. in review, 2023. Evaluation of multi-season convection permitting atmosphere - mixed layer ocean simulations of the Maritime Continent [preprint]. Geosci. Model Dev.

Hoyos, C.D., & Webster, P.J. 2012. Evolution and modulation of tropical heating from the last glacial maximum through the twenty-first century. Clim. Dyn., **38**, 1501–1519.

Hsu, H.-H., & Lee, M.-Y. 2005. Topographic Effects on the Eastward Propagation and Initiation of the Madden-Julian Oscillation. J. Clim., **18**, 795–809.

Hu, S., Hu, D., Guan, C., Xing, N., & Li, J. Feng, J. 2017. Variability of the western Pacific warm pool structure associated with El Niño. Clim. Dyn., **49**, 2431–2449.

Huffman, G.J., Bolvin, D.T., Braithwaite, D., Hsu, K., Joyce, R., Xie, P., & Yoo, S.-H. 2015. NASA global precipitation measurement (GPM) integrated multi-satellite retrievals for GPM (IMERG). Algorithm Theoretical Basis Document (ATBD) Version, **4**, 26.

Hung, M.-P., Lin, J.-L., Wang, W., Kim, D., Shinoda, T., & Weaver, S.J. 2013. Mjo and convectively coupled equatorial waves simulated by CMIP5 climate models. J. Clim., **26**, 6185–6214.

Ichikawa, H., & Yasunari, T. 2006. Time-Space Characteristics of Diurnal Rainfall over Borneo and Surrounding Oceans as Observed by TRMM-PR. J. Clim., **19**, 1238–1260.

Ignatov, A., & Gutman, G. 1999. Monthly Mean Diurnal Cycles in Surface Temperatures over Land for Global Climate Studies. J. Clim., **12**, 1900–1910.

Inness, P.M., & Slingo, J.M. 2003. Simulation of the Madden-Julian Oscillation in a Coupled General Circulation Model. Part I: Comparison with Observations and an Atmosphere-Only GCM. J. Clim., **16**, 345–364.

Janowiak, J.E., Kousky, V.E., & Joyce, R.J. 2005. Diurnal cycle of precipitation determined from the CMORPH high spatial and temporal resolution global precipitation analyses. J. Geophys. Res.: Atm., **110**, 1–18.

Jiang, X., Waliser, D.E., Xavier, P.K., Petch, J., Klingaman, N.P., Woolnough, S.J., Guan, B., Bellon, G., Crueger, T., DeMott, C., Hannay, C., Lin, H., Hu, W., Kim, D., Lappen, C.L., Lu, M.-M., Ma, H.-Y., Miyakawa, T., Ridout, J.A., Schubert, S.D., Scinocca, J., Seo, K.-H., Shindo, E., Song, X., Stan, C., Tseng, W.-L., Wang, W., Wu, T., Wu, X., Wyser, K., Zhang, G.J., & Zhu, H. 2015. Vertical structure and physical processes of the madden-julian oscillation: Exploring key model physics in climate simulations. J. Geophys. Res.: Atm., **120**, 4718–4748.

Jiang, X., Adames, Á.F., Kim, D., Maloney, E.D., Lin, H., Kim, H., Zhang, C., DeMott, C.A., & Klingaman, N.P. 2020. Fifty Years of Research on the Madden-Julian Oscillation: Recent Progress, Challenges, and Perspectives. J. Geophys. Res.: Atm., **125**.

Jin, F., & Hoskins, B.J. 1995. The Direct Response to Tropical Heating in a Baroclinic Atmosphere. J. Atm. Sci., **52**, 307–319.

Junquas, C., Takahashi, K., Condom, T., Espinoza, J.C., Chavez, S., Sicart, J.E., & Lebel, T. 2018. Understanding the influence of orography on the precipitation diurnal cycle and the associated atmospheric processes in the central Andes. Clim. Dyn., **50**, 3995–4017.

Kang, D., Kim, D., Ahn, M.-S., & An, S.-I. 2021. The Role of the Background Meridional Moisture Gradient on the Propagation of the MJO over the Maritime Continent. J. Clim., **34**, 6565–6581.

Kerns, B.W., & Chen, S.S. 2016. Large-scale precipitation tracking and the MJO over the Maritime Continent and Indo-Pacific warm pool. J. Geophys. Res.: Atm., **121**, 8755–8776.

Kikuchi, K., & Wang, B. 2008. Diurnal precipitation regimes in the global tropics. J. Clim., **21**, 2680–2696.

Kikuchi, K., Wang, B., & Kajikawa, Y. 2012. Bimodal representation of the tropical intraseasonal oscillation. Clim. Dyn., **38**, 1989–2000.

Kikuchi, K., Kiladis, G.N., Dias, J., & Nasuno, T. 2018. Convectively coupled equatorial waves within the MJO during CINDY/DYNAMO: slow Kelvin waves as building blocks. Clim. Dyn., **50**, 4211–4230.

Kiladis, G.N., Wheeler, M.C., Haertel, P., Straub, K.H., & Roundy, P. 2009. Convectively coupled equatorial waves. Rev. Geophys., **47**.

Kiladis, G.N., Dias, J., Straub, K.H., Wheeler, M.C., Tulich, S.N., Kikuchi, K., Weickmann, K.M., & Ventrice, M.J. 2014. A comparison of OLR and circulation-based indices for tracking the MJO. Mon. Wea. Rev., **142**, 1697–1715.

Kim, D., Kug, J.S., & Sobel, A.H. 2014. Propagating versus nonpropagating Madden-Julian oscillation events. J. Clim., **27**, 111–125.

Kim, D., Kim, H., & Lee, M.-I. 2017. Why does the MJO detour the Maritime Continent during austral summer? Geophys. Res. Lett., **44**, 2579–2587.

Kim, H., & Benedict, J.J. 2023. The idealized aqua-planet Maritime Continent barrier effect on the MJO predictability. J. Clim., **36**, 5757–5773.

Kim, H., Kim, D., Vitart, F., Toma, V., Kug, J., & Webster, P. 2016. MJO propagation across the maritime continent in the ECMWF ensemble prediction system. J. Clim., **29**, 3973–3988.

Kim, H.R., Ha, K.J., Moon, S., Oh, H., & Sharma, S. 2020. Impact of the indo-pacific warm pool on the hadley, walker, and monsoon circulations. Atmosphere, **11**, 1030.

Kirschbaum, D., Adler, R., Adler, D., Peters-Lidard, C., & Huffman, G. 2012. Global distribution of extreme precipitation and high-impact landslides in 2010 relative to previous years. J. Hydromet., **13**, 1536–1551.

Koutsoyiannis, D. 2012. Clausius-Clapeyron equation and saturation vapour pressure: Simple theory reconciled with practice. Eur. J. Phys., **33**, 295–305.

Krishnamurti, T.N., & Subrahmanyam, D. 1982. The 30–50 Day Mode at 850 mb During MONEX. J. Atm. Sci., **39**, 2088–2095.

Kummerow, C.D., Hong, Y., Olson, W.S., Yang, S., Adler, R.F., McCollum, J., Ferraro, R., Petty, G., Shin, D.-B., & Wilheit, T.T. 2001. The Evolution of the Goddard Profiling Algorithm (GPROF) for Rainfall Estimation from Passive Microwave Sensors. J. App. Met. Clim., **40**, 1801–1820.

Kummerow, C.D., Randel, D.L., Kulie, M., Wang, N.-Y., Ferraro, R., Joseph Munchak, S., & Petkovic, V. 2015. The evolution of the Goddard profiling algorithm to a fully parametric scheme. J. Atm. Ocean. Tech., **32**, 2265–2280.

Lang, F., Huang, Y., Siems, S.T., & Manton, M.J. 2020. Evidence of a diurnal cycle in precipitation over the southern ocean as observed at Macquarie Island. Atmosphere, **11**, 181.

Large, W.G., McWilliams, J.C., & Doney, S.C. 1994. Oceanic vertical mixing: A review and a model with a nonlocal boundary layer parameterization. Rev. Geophys., **32**, 363–403.

Latos, B., Lefort, T., Flatau, M.K., Flatau, P.J., Permana, D.S., Baranowski, D.B., Paski, J.A.I., Makmur, E., Sulystyo, E., Peyrillé, P., Feng, Z., Matthews, A.J., & Schmidt, J.M. 2021. Equatorial waves triggering extreme rainfall and floods in southwest sulawesi, Indonesia. Mon. Wea. Rev., **149**, 1381–1401.

Latos, B., Peyrillé, P., Lefort, T., Baranowski, D.B., Flatau, M.K., Flatau, P.J., Riama, N.F., Permana, D.S., Rydbeck, A.V., & Matthews, A.J. 2023. The role of tropical waves in the genesis of Tropical Cyclone Seroja in the Maritime Continent. Nature Comms., **14**, 856.

Lau, K.-M., Chang, C.-P., & Chan, P.H. 1983. Short-Term Planetary-Scale Interactions over the Tropics and Midlatitudes. Part II: Winter-MONEX Period. Mon. Wea. Rev., **111**, 1372–1388.

Lee, R., Woolnough, S., Charlton-Perez, A., & Vitart, F. 2019. ENSO Modulation of MJO Teleconnections to the North Atlantic and Europe. Geophys. Res. Lett., **46**, 13535–13545.

Li, C., Hu, R., & Hui, Y. 2005. Intraseasonal Oscillation in the Tropical Indian Ocean. Adv. Atm. Sci., **22**, 617–624.

Li, Y., Huang, S., & Wen, Z. 2022. The Influence of the Stratospheric Quasi-Biennial Oscillation on the Tropical Easterly Jet Over the Maritime Continent. Geoophys. Res. Lett., **49**.

Ling, J., Zhao, Y., & Chen, G. 2019a. Barrier effect on MJO propagation by the maritime continent in the MJO Task Force/GeWEX atmospheric system study models. J. Clim., **32**, 5529–5547.

Ling, J., Zhang, C., Joyce, R., Xie, P., & Chen, G. 2019b. Possible Role of the Diurnal Cycle in Land Convection in the Barrier Effect on the MJO by the Maritime Continent. Geophys. Res. Lett., **46**, 3001–3011.

Liu, B., Goree, J., Flanagan, T.M., Sen, A., Tiwari, S.K., Ganguli, G., & Crabtree, C. 2018. Experimental observation of cnoidal waveform of nonlinear dust acoustic waves. Phys. Plasmas, **25**.

Love, B.S., Matthews, A.J., & Lister, G.M.S. 2011. The diurnal cycle of precipitation over the Maritime Continent in a high-resolution atmospheric model. Q. J. Roy. Met. Soc., **137**, 934–947.

Lu, J., Li, T., & Wang, L. 2019. Precipitation diurnal cycle over the Maritime Continent modulated by the MJO. Clim. Dyn., **53**, 6489–6501.

Lu, J., Li, T., & Wang, L. 2021. Precipitation diurnal cycle over the maritime continent modulated by the climatological annual cycle. J. Clim., **34**, 1387–1402.

Madden, R.A., & Julian, P.R. 1971. Detection of a 40–50 Day Oscillation in the Zonal Wind in the Tropical Pacific. J. Atm. Sci., **28**, 702–708.

Madden, R.A., & Julian, P.R. 1972. Description of Global-Scale Circulation Cells in the Tropics with a 40–50 Day Period. J. Atm. Sci., **29**, 1109–1123.

Madden, R.A., & Julian, P.R. 1994. Observations of the 40–50-Day Tropical Oscillation — A Review. Mon. Wea. Rev., **122**, 814–837.

Majda, A.J., & Stechmann, S.N. 2009. The skeleton of tropical intraseasonal oscillations. Pr. Nat. Ac. Sci. USA, **106**, 8417–8422.

Mapes, B.E., & Houze, R.A. 1993. Cloud Clusters and Superclusters over the Oceanic Warm Pool. Mon. Wea. Rev., **121**, 1398–1416.

Mapes, B.E., Warner, T.T., & Xu, M. 2003. Diurnal Patterns of Rainfall in Northwestern South America. Part III: Diurnal Gravity Waves and Nocturnal Convection Offshore. Mon. Wea. Rev., **131**, 830–844.

Martin, Z., Son, S.-W., Butler, A., Hendon, H., Kim, H., Sobel, A., Yoden, S., & Zhang, C. 2021. The influence of the quasi-biennial oscillation on the Madden–Julian oscillation. Nature Rev. Earth Env., **2**, 477–489.

Matsuno, T. 1966. Quasi-Geostrophic Motions in the Equatorial Area. J. Met. Soc. Japan, **44**, 25–43.

Matthews, A.J. 2008. Primary and successive events in the Madden-Julian Oscillation. Q. J. Roy. Met. Soc., **134**, 439–453.

Matthews, A.J., Baranowski, D.B., Heywood, K.J., Flatau, P.J., & Schmidtko, S. 2014. The surface diurnal warm layer in the Indian ocean during CINDY/DYNAMO. J. Clim., **27**, 9101–9122.

Meehl, G.A., Lukas, R., Kiladis, G.N., Weickmann, K.M., Matthews, A.J., & Wheeler, M. 2001. A conceptual framework for time and space scale interactions in the climate system. Clim. Dyn., **17**, 753–775.

Minobe, S., Park, J.H., & Virts, K.S. 2020. Diurnal cycles of precipitation and lightning in the tropics observed by TRMM3G68, GSMaP, LIS, and WWLLN. J. Clim., **33**, 4293–4313.

Mori, S., Jun-Ichi, H., Yamanaka, M., Okamoto, N., Murata, F., Sakurai, N., & Hashiguchi, H. 2004. Diurnal Land-Sea Rainfall Peak Migration over Sumatera Island, Indonesian Maritime Continent, Observed by TRMM Satellite and Intensive Rawinsonde Soundings. Mon. Wea. Rev., **132**, 2021–2039.

Mustafa, J.M., Matthews, A.J., Hall, R.A., Heywood, K.J., & Azaneu, M.V.C. 2024. Characterisation of the observed diurnal cycle of precipitation over the Maritime Continent. Q. J. Roy. Met. Soc.

Nakazawa, T. 1988. Tropical Super Clusters within Intraseasonal Variations over the Western Pacific. J. Met. Soc. Japan, **66**, 823–839.

Neale, R., & Slingo, J. 2003. The Maritime Continent and Its Role in the Global Climate: A GCM Study. J. Clim., **16**, 834–848.

Nesbitt, S.W., & Zipser, E.J. 2003. The Diurnal Cycle of Rainfall and Convective Intensity according to Three Years of TRMM Measurements. J. Clim., **16**, 1456–1475.

Nicholson, S.E., Hartman, A.T., & Klotter, D.A. 2021. On the Diurnal Cycle of Rainfall and Convection over Lake Victoria and Its Catchment. Part II: Meteorological Factors in the Diurnal and Seasonal Cycles. J. Hydromet., **22**, 3049–3064.

Nitta, T., & Sekine, S. 1994. Diurnal variation of convective activity over the tropical western Pacific. J. Met. Soc. Japan, **72**, 627–640.

Oh, J.-H., Kim, K.Y., & Lim, G.H. 2012. Impact of MJO on the diurnal cycle of rainfall over the western Maritime Continent in the austral summer. Clim. Dyn., **38**, 1167–1180.

Oh, J.-H., Kim, B.-M., Kim, K.-Y., Song, H.-J., & Lim, G.-H. 2013. The impact of the diurnal cycle on the MJO over the Maritime Continent: A modeling study assimilating TRMM rain rate into global analysis. Clim. Dyn., **40**, 893–911.

Peatman, S.C., Matthews, A.J., & Stevens, D.P. 2014. Propagation of the Madden–Julian Oscillation through the Maritime Continent and scale interaction with the diurnal cycle of precipitation. Q. J. Roy. Met. Soc., **140**, 814–825.

Peatman, S.C., Matthews, A.J., & Stevens, D.P. 2015. Propagation of the Madden–Julian Oscillation and scale interaction with the diurnal cycle in a high-resolution GCM. Clim. Dyn., **45**, 2901–2918.

Peatman, S.C., Schwendike, J., Birch, C.E., Marsham, J.H., Matthews, A.J., & Yang, G.-Y. 2021. A Local-to-Large Scale View of Maritime Continent Rainfall: Control by ENSO, MJO, and Equatorial Waves. J. Clim., **34**, 8933–8953.

Peatman, S.C., Birch, C.E., Schwendike, J., Marsham, J.H., Dearden, C., Webster, S., Neely, R.R., & Matthews, A.J. 2023. The Role of Density Currents and Gravity Waves in the Offshore Propagation of Convection over Sumatra. Mon. Wea. Rev., **151**, 1757–1777.

Power, S., Lengaigne, M., Capotondi, A., Khodri, M., Vialard, J., Jebri, B., Guilyardi, E., McGregor, S., Kug, J.-S., Newman, M., McPhaden, M.J., Meehl, G., Smith, D., Cole, J., Emile-Geay, J., Vimont, D., Wittenberg, A.T., Collins, M.,

Kim, G.-I., Cai, W., Okumura, Y., Chung, C., Cobb, K.M., Delage, F., Planton, Y.Y., Levine, A., Zhu, F., Sprintall, J., Di Lorenzo, E., Zhang, X.B., Luo, J.J., Lin, X.P., Balmaseda, M., Wang, G.J., & Henley, B.J. 2021. Decadal climate variability in the tropical Pacific: Characteristics, causes, predictability, and prospects. Science, **374**, 6563.

Qian, T., Epifanio, C.C., & Zhang, F. 2012. Topographic effects on the tropical land and sea breeze. J. Atm. Sci., **69**, 130–149.

Rais, A.F., & Yunita, R. 2017. Main diurnal cycle pattern of rainfall in East Java. AIP Conference Proceedings, **1867**.

Ramage, C. 1968. Role of a tropical "Maritime Continent" in the atmospheric circulation. Mon. Wea. Rev., **96**, 365–370.

Rauniyar, S.P., & Walsh, K.J.E. 2011. Scale interaction of the diurnal cycle of rainfall over the Maritime Continent and Australia: Influence of the MJO. J. Clim., **24**, 325–348.

Renner, M., Kleidon, A., Clark, M., Nijssen, B., Heidkamp, M., Best, M., & Abramowitz, G. 2021. How well can land-surface models represent the diurnal cycle of turbulent heat fluxes? J. Hydromet., **22**, 77–94.

Repinaldo, H.F.B., Nicolini, M., & Skabar, Y.G. 2015. Characterizing the diurnal cycle of low-level circulation and convergence using CFSR data in southeastern South America. J. App. Met. Clim., **54**, 671–690.

Riehl, H. 1947. Diurnal Variation of Cloudiness Over the Subtropical Atlantic Ocean. Bull. Amer. Met. Soc., **28**, 37–40.

Rio, C., Hourdin, F., Grandpeix, J.Y., & Lafore, J.P. 2009. Shifting the diurnal cycle of parameterized deep convection over land. Geophys. Res. Lett., **36**.

Roberts, M.J., Baker, A., Blockley, E.W., Calvert, D., Coward, A., Hewitt, H.T., Jackson, L.C., Kuhlbrodt, T., Mathiot, P., Roberts, C.D., Schiemann, R., Seddon, J., Vannière, B., & Vidale, P.L. 2019. Description of the resolution hierarchy of the global coupled HadGEM3-GC3.1 model as used in CMIP6 HighResMIP experiments. Geosci. Model Dev., **12**, 4999–5028.

Roxy, M., Dasgupta, P., McPhaden, M., Suematsu, T., Zhang, C., & Kim, D. 2019. Twofold expansion of the Indo-Pacific warm pool warps the MJO life cycle. Nature, **575**, 647–651.

Rui, H., & Wang, B. 1990. Development Characteristics and Dynamic Structure of Tropical Intraseasonal Convection Anomalies. J. Atm. Sci., **47**, 357–379.

Sakaeda, N., Kiladis, G., & Dias, J. 2017. The diurnal cycle of tropical cloudiness and rainfall associated with the Madden-Julian oscillation. J. Clim., **30**, 3999–4020.

Sakaeda, N., Kiladis, G., & Dias, J. 2020. The diurnal cycle of rainfall and the convectively coupled equatorial waves over the maritime continent. J. Clim., **33**, 3307–3331.

Salby, M.L., & Hendon, H.H. 1994. Intraseasonal Behavior of Clouds, Temperature, and Motion in the Tropics. J. Atm. Sci., **51**, 2207–2224.

Sane, Y., Bonazzola, M., Rio, C., Chambon, P., Fiolleau, T., Musat, I., Hourdin, F., Roca, R., Grandpeix, J.Y., & Diedhiou, A. 2012. An analysis of the diurnal cycle of precipitation over Dakar using local rain-gauge data and a general circulation model. Q. J. Roy. Met. Soc., **138**, 2182–2195.

Santoso, A., McPhaden, M.J., & Cai, W. 2017. The Defining Characteristics of ENSO Extremes and the Strong 2015/2016 El Niño. Rev. Geophys., **55**, 1079–1129.

Savarin, A., & Chen, S.S. 2023. Land-locked convection as a barrier to MJO propagation across the Maritime Continent. J. Adv. Model. Earth Sys., **15**.

Schindelegger, M., & Ray, R.D. 2014. Surface Pressure Tide Climatologies Deduced from a Quality-Controlled Network of Barometric Observations. Mon. Wea. Rev., **142**, 4872–4889.

Schumacher, C., & Houze, R.A. 2003. The TRMM Precipitation Radar's View of Shallow, Isolated Rain. J. App. Met. Clim., **42**, 1519–1524.

Schwendike, J., Berry, G.J., Reeder, M.J., Jakob, C., Govekar, P., & Wardle, R. 2015. Trends in the local Hadley and local Walker circulations. J. Geophys. Res.: Atm., **120**, 7599–7618.

Seiki, A., Yokoi, S., & Katsumata, M. 2021. The impact of diurnal precipitation over sumatra island, indonesia, on synoptic disturbances and its relation to the madden-julian oscillation. J. Met. Soc. Japan, **99**, 113–137.

Sekaranom, A.B., Nurjani, E., Hadi, M.P., & Marfai, M.A. 2018. Comparsion of TRMM Precipitation Satellite Data over Central Java Region - Indonesia. Qua. Geo., **37**, 97–114.

Senior, N.V., Matthews, A.J., Webber, B.G.M., Webster, S., Jones, R.W., Permana, D.S., Paski, J.A.I., & Fadila, R. 2023. Extreme precipitation at Padang, Sumatra triggered by convectively coupled Kelvin waves. Q. J. Roy. Met. Soc., **149**, 2281–2300.

Seo, K.-H., & Kim, K.-Y. 2003. Propagation and initiation mechanism of the Madden-Julian oscillation. J. Geophys. Res.: Atm., **108**.

Seo, K.-H., Wang, W., Gottschalck, J., Zhang, Q., Schemm, J.K.E., Higgins, W.R., & Kumar, A. 2009. Evaluation of MJO forecast skill from several statistical and dynamical forecast models. J. Clim., **22**, 2372–2388.

Sharifnezhad, Z., Norouzi, H., Prakash, S., Blake, R., & Khanbilvardi, R. 2021. Diurnal cycle of passive microwave brightness temperatures over land at a global scale. Rem. Sens., **13**, 1–14.

Shepherd, J.M. 2005. A Review of Current Investigations of Urban-Induced Rainfall and Recommendations for the Future. Earth Int., **9**, 1–27.

Short, E., Vincent, C.L., & Lane, T.P. 2019. Diurnal cycle of surface winds in the maritime continent observed through satellite scatterometry. Mon. Wea. Rev., **147**, 2023–2044.

Skinner, D.T., Matthews, A.J., & Stevens, D.P. 2022. North Atlantic Oscillation response to the Madden–Julian Oscillation in a coupled climate model. Weather, **77**, 201–205.

Slingo, J., Inness, P., Neale, R., Woolnough, S., & Yang, G.-Y. 2003. Scale interactions on diurnal to seasonal timescales and their relevance to model systematic errors. Ann. Geophys., **46**, 139–155.

Smith, G.L., & Rutan, D.A. 2003. The Diurnal Cycle of Outgoing Longwave Radiation from Earth Radiation Budget Experiment Measurements. J. Atm. Sci., **60**, 1529–1542.

Sobel, A., & Maloney, E. 2012. An idealized semi-empirical framework for modeling the Madden-Julian oscillation. J. Atm. Sci., **69**, 1691–1705.

Sobel, A., & Maloney, E. 2013. Moisture modes and the eastward propagation of the MJO. J. Atm. Sci., **70**, 187–192.

Sobel, A.H., Maloney, E.D., Bellon, G., & Frierson, D.M. 2010. Surface Fluxes and Tropical Intraseasonal Variability: a Reassessment. J. Adv. Model. Earth Sys., **2**, 2.

Soden, B.J. 2000. The diurnal cycle of convection, clouds, and water vapor in the tropical upper troposphere. Geophys. Res. Lett., **27**, 2173–2176.

Soloviev, A., & Lukas, R. 1997. Observation of large diurnal warming events in the near-surface layer of the western equatorial Pacific warm pool. Deep Sea Res. P1: Ocean. Res. Pap., **44**, 1055–1076.

Son, S.-W., Lim, Y., Yoo, C., Hendon, H.H., & Kim, J. 2017. Stratospheric Control of the Madden-Julian Oscillation. J. Clim., **30**, 1909–1922.

Sui, C.-H., & Lau, K.-M. 1992. Multiscale Phenomena in the Tropical Atmosphere over the Western Pacific. Mon. Wea. Rev., **120**, 407–430.

Sui, C.-H., Li, X., Lau, K.-M., & Adamec, D. 1997. Multiscale Air-Sea Interactions during TOGA COARE. Mon. Wea. Rev., **125**, 448–462.

Sun, L., Wang, H., & Liu, F. 2019. Combined effect of the QBO and ENSO on the MJO. Atm. Ocean. Sci. Lett., **12**, 170–176.

Suzuki, T. 2009. Diurnal cycle of deep convection in super clusters embedded in the Madden-Julian Oscillation. J. Geophys. Res.: Atm., **114**.

Szkolka, W.R., Baranowski, D.B., Flatau, M.K., Marzuki, M., Shimomai, T., & Hashiguchi, H. 2023. Diurnal Cycle of Tropospheric Winds over West Sumatra and Its Variability Associated with Various Climate and Weather Modes. Atmosphere, **14**.

Tan, H., Ray, P., Barrett, B., Dudhia, J., Moncrieff, M., Zhang, L., & Zermeno-Diaz, D. 2022. Understanding the role of topography on the diurnal cycle of precipitation in the Maritime Continent during MJO propagation. Clim. Dyn., **58**, 3003–3019.

Tan, J., Huffman, G., Bolvin, D., & Nelkin, E. 2019a. Diurnal Cycle of IMERG V06 Precipitation. Geophys. Res. Lett., **46**, 13584–13592.

Tan, J., Huffman, G., Bolvin, D., & Nelkin, E. 2019b. IMERG V06: Changes to the Morphing Algorithm. J. Atm. Ocean. Tech., **36**, 2471–2482.

Tappeiner, H.W., Klatzky, R.L., Unger, B., & Hollis, R. 2009. Good Vibrations: Asymmetric vibrations for directional haptic cues. Proceedings - 3rd Joint EuroHaptics Conference and Symposium on Haptic Interfaces for Virtual Environment and Teleoperator Systems, **World Haptics 2009**, 285–289.

Tastula, E.M., Vihma, T., Andreas, E.L., & Galperin, B. 2013. Validation of the diurnal cycles in atmospheric reanalyses over Antarctic sea ice. J. Geophys. Res.:. Atm., **118**, 4194–4204.

Taylor, P.C. 2012. Tropical outgoing longwave radiation and longwave cloud forcing diurnal cycles from CERES. J. Atm. Sci., **69**, 3652–3669.

Tian, B., Soden, B.J., & Wu, X. 2004. Diurnal cycle of convection, clouds, and water vapor in the tropical upper troposphere: Satellites versus a general circulation model. J. Geophys. Res.: Atm., **109**.

Tian, B., Waliser, D.E., & Fetzer, E.J. 2006. Modulation of the diurnal cycle of tropical deep convective clouds by the MJO. Geophys. Res. Lett., **33**.

Toh, Y.Y., Turner, A.G., Johnson, S.J., & Holloway, C.E. 2018. Maritime Continent seasonal climate biases in AMIP experiments of the CMIP5 multimodel ensemble. Clim. Dyn., **50**, 777–800.

Tsuda, T., Ratnam, M.V., Kozu, T., & Mori, S. 2006. Characteristics of 10-day Kelvin Wave Observed with Radiosondes and CHAMP/GPS Occultation during the CPEA Campaign (April-May, 2004). J. Met. Soc. Japan, **84A**, 277–293.

Ungerovich, M., Barreiro, M., & Masoller, C. 2021. Influence of Madden–Julian Oscillation on extreme rainfall events in Spring in southern Uruguay. I. J. Clim., **41**, 3339–3351.

Valcke, S. 2013. The OASIS3 coupler: a European climate modelling community software. Geosci. Model Dev., **6**, 373–388.

Ventrice, M.J., Wheeler, M.C., Hendon, H.H., Schreck, C.J., Thorncroft, C.D., & Kiladis, G.N. 2013. A modified multivariate Madden-Julian oscillation index using velocity potential. Mon. Wea. Rev., **141**, 4197–4210.

Vincent, C.L., & Lane, T.P. 2016. Evolution of the diurnal precipitation cycle with the passage of a Madden-Julian oscillation event through the Maritime Continent. Mon. Wea. Rev., **144**, 1983–2005.

Vincent, C.L., & Lane, T.P. 2017. A 10-Year Austral Summer Climatology of Observed and Modeled Intraseasonal, Mesoscale, and Diurnal Variations over the Maritime Continent. J. Clim., **30**, 3807–3828.

Virts, K.S., Wallace, J.M., Hutchins, M.L., & Holzworth, R.H. 2013. Diurnal lightning variability over the maritime continent: Impact of low-level winds, cloudiness, and the MJO. J. Atm. Sci., **70**, 3128–3146.

Vitart, F., & Molteni, F. 2010. Simulation of the Madden–Julian Oscillation and its teleconnections in the ECMWF forecast system. Q. J. Roy. Met. Soc., **136**, 829–1102.

Waliser, D.E., Moncrieff, M.W., Burridge, D., Fink, A.H., Gochis, D., Goswami, B.N., Guan, B., Harr, P., Heming, J., Hsu, H.-H., Jakob, C., Janiga, M., Johnson, R., Jones, S., Knippertz, P., Marengo, J., Nguyen, H., Pope, M., Serra, Y., Thorncroft, C., Wheeler, M., Wood, R., & Yuter, S. 2012. The "year" of tropical convection (May 2008–April 2010): Climate variability and weather highlights. Bull. Amer. Met. Soc., **93**, 1189–1218.

Walters, D., Baran, A.J., Boutle, I., Brooks, M., Earnshaw, P., Edwards, J., Furtado, K., Hill, P., Lock, A., Manners, J., Morcrette, C., Mulcahy, J., Sanchez, C., Smith, C., Stratton, R., Tennant, W., Tomassini, L., Van Weverberg, K., Vosper, S., Willett, M., Browse, J., Bushell, A., Carslaw, K., Dalvi, M., Essery, R., Gedney, N., Hardiman, S., Johnson, B., Johnson, C., Jones, A., Jones, C., Mann, G., Milton, S., Rumbold, H., Sellar, A., Ujiie, M., Whitall, M., Williams, K., & Zerroukat, M. 2019. The Met Office Unified Model Global Atmosphere 7.0/7.1 and JULES Global Land 7.0 configurations. Geosci. Model Dev., **12**, 1909–1963.

Wang, B. 1988. Dynamics of Tropical Low-Frequency Waves: An Analysis of the Moist Kelvin Wave. J. Atm. Sci., **45**, 2051–2065.

Wang, B., Liu, F., & Chen, G. 2016. A trio-interaction theory for Madden–Julian oscillation. Geosci. Lett., **3**.

Wang, X., & Zender, C.S. 2011. Arctic and Antarctic diurnal and seasonal variations of snow albedo from multiyear Baseline Surface Radiation Network measurements. J. Geophys. Res.: Earth Surf., **116**, F03008.

Wang, Y., Heywood, K.J., Stevens, D.P., & Damerell, G.M. 2022. Seasonal extrema of sea surface temperature in CMIP6 models. Ocean Sci., **18**, 839–855.

Webster, P.J., & Lukas, R. 1992. TOGA COARE: The Coupled Ocean–Atmosphere Response Experiment. Bull. Amer. Met. Soc., **73**, 1377–1416.

Webster, P.J., Clayson, C.A., & Curry, J.A. 1996. Clouds, Radiation, and the Diurnal Cycle of Sea Surface Temperature in the Tropical Western Pacific. J. Clim., **9**, 1712–1730.

Wei, Y., Pu, Z., & Zhang, C. 2020. Diurnal Cycle of Precipitation Over the Maritime Continent Under Modulation of MJO: Perspectives From Cloud-Permitting Scale Simulations. J. Geophys. Res.: Atm., **125**.

Weickmann, K.M., Lussky, G.R., & Kutzbach, J.E. 1985. Intraseasonal (30–60 Day) Fluctuations of Outgoing Longwave Radiation and 250 mb Streamfunction during Northern Winter. Mon. Wea. Rev., **113**, 941–961.

Wheeler, M.C., & Hendon, H.H. 2004. An All-Season Real-Time Multivariate MJO Index: Development of an Index for Monitoring and Prediction. Mon. Wea. Rev., **132**, 1917–1932.

Worku, L.Y., Mekonnen, A., & Schreck, C.J. 2019. Diurnal cycle of rainfall and convection over the Maritime Continent using TRMM and ISCCP. I. J. Clim., **39**, 5191–5200.

Worku, L.Y., Mekonnen, A., & Schreck, C.J. 2020. The impact of MJO, Kelvin, and equatorial rossby waves on the diurnal cycle over the maritime continent. Atmosphere, **11**.

Wu, C.-H., & Hsu, H.-H. 2009. Topographic influence on the MJO in the maritime continent. J. Clim., **22**, 5433–5448.

Wu, P., Hara, M., Hamada, J.I., Yamanaka, M.D., & Kimura, F. 2009. Why a large amount of rain falls over the sea in the vicinity of western Sumatra Island during nighttime. J. App. Met. Clim., **48**, 1345–1361.

Xu, W., & Rutledge, S.A. 2014. Convective characteristics of the madden-julian oscillation over the central indian ocean observed by shipborne radar during DYNAMO. J. Atm. Sci., **71**, 2859–2877.

Xue, P., Malanotte-Rizzoli, P., Wei, J., & Eltahir, E.A.B. 2020. Coupled Ocean-Atmosphere Modeling Over the Maritime Continent: A Review. J. Geophys. Res.: Oceans, **125**.

Yang, D., & Ingersoll, A.P. 2013. Triggered convection, gravity waves, and the MJO: A shallow-water model. J. Atm. Sci., **70**, 2476–2486.

Yang, G.-Y., & Slingo, J. 2001. The Diurnal Cycle in the Tropics. Mon. Wea. Rev., **129**, 784–801.

Yang, S., & Smith, E.A. 2006. Mechanisms for Diurnal Variability of Global Tropical Rainfall Observed from TRMM. J. Clim., **19**, 5190–5226.

Yin, Z., Dong, Q., Xiang, K., & Bian, M. 2022. Spatio-Temporal Characteristics of the Indo-Pacific Warm Pool and the Corresponding Rain Pool. Sustainability, **14**, 10841.

Yokoi, S., Mori, S., Syamsudin, F., Haryoko, U., & Geng, B. 2019. Environmental conditions for nighttime offshore migration of precipitation area as revealed by in situ observation off Sumatra Island. Mon. Wea. Rev., **147**, 3391–3407.

Yoneyama, K., & Zhang, C. 2020. Years of the Maritime Continent. Geophys. Res. Lett., **47**.

Yoneyama, K., Zhang, C., & Long, C.N. 2013. Tracking pulses of the Madden-Julian oscillation. Bull. Amer. Met. Soc., **94**, 1871–1891.

Zhang, C. 2005. Madden-Julian Oscillation. Rev. Geophys., **43**.

Zhang, C., & Chen, G. 2008. The atmospheric wet pool: Definition and comparison with the oceanic warm pool. Chin. J. Ocean. Limn., **26**, 440–449.

Zhang, C., & Ling, J. 2017. Barrier effect of the Indo-Pacific Maritime Continent on the MJO: Perspectives from tracking MJO precipitation. J. Clim., **30**, 3439–3459.

Zhang, C., Adames, Á.F., Khouider, B., Wang, B., & Yang, D. 2020. Four Theories of the Madden-Julian Oscillation. Rev. Geophys., **58**.

Zhang, H., Beggs, H., Wang, X., Kiss, A., & Griffin, C. 2016. Seasonal patterns of SST diurnal variation over the Tropical Warm Pool region. J. Geophys. Res.: Oceans, **121**, 8077–8094.

Zhang, W., Cao, Y., Zhu, Y., Zheng, J., Ji, X., Xu, Y., Wu, Y., & Hoitink, A.J.F. 2018. Unravelling the causes of tidal asymmetry in deltas. J. Hydrol., **564**, 588–604.

Zhou, J., Chen, Y., Zhang, X., & Zhan, W. 2013. Modelling the diurnal variations of urban heat islands with multi-source satellite data. I. J. Rem. Sens., **34**, 7568–7588.

Zhou, Y., Fang, J., & Wang, S. 2021. Impact of islands on the MJO propagation across the maritime continent: a numerical modeling study of an MJO event. Clim. Dyn., **57**, 2921–2935.